Mathematical Modeling of Bladder Mechanobiology

by

Fangzhou Cheng

B.S., University of Pittsburgh, 2013

Submitted to the Graduate Faculty of

the Swanson School of Engineering in partial fulfillment

of the requirements for the degree of

Doctor of Philosophy

University of Pittsburgh

2021

UNIVERSITY OF PITTSBURGH

SWANSON SCHOOL OF ENGINEERING

This dissertation was presented

by

Fangzhou Cheng

It was defended on

November 19 2021

and approved by

William S. Slaughter, PhD, Professor, Department of Mechanical Engineering and Materials Science

Patrick Smolinski, PhD, Professor, Department of Mechanical Engineering and Materials Science

Lori A. Birder, PhD, Professor, Department of Medicine

Paul N. Watton, PhD, Professor, Department of Computer Science

Dissertation Director: Anne M. Robertson, PhD, Professor, Department of Mechanical Engineering and Materials Science

Mathematical Modeling of Bladder Mechanobiology

Fangzhou Cheng, PhD

University of Pittsburgh, 2021

Lower urinary tract symptoms (LUTS), including an increase of urination urgency, frequency, incontinence, residual volume, are relevant to the deterioration of bladder mechanical function and can significantly lower the quality of life. Urodynamics, the gold standard of bladder diagnosis, has often been used to assess bladder functionality. Urodynamic data, which include pressure and volume change during filling, are affected by the mechanical properties of the bladder. However, the underlying mechanisms of bladder pathologies are not fully understood and therefore the interpretation of urodynamic data is highly subjective and may be inconclusive; often requiring further testing or leading to inappropriate treatment. Although morphological changes such as smooth muscle hypertrophy and collagen fibrosis have been commonly observed in the dysfunctional bladder, the effect of these changes on the bladder mechanical function has not been fully explained. In this work, we integrated in situ mechanical testing and multiphoton microscopy to assess bladder mechanical properties and reorganization, growth and remodeling. As a first step, a constitutive model, motivated by the collagen fiber structure, was developed and used to investigate the mechanical function under aging, disease, and pharmacological treatments. This model was then further sophisticated to model the bladder filling and voiding process by integrating the results from in-vivo and ex-vivo experiments. Lastly, a growth and remodeling framework, which has demonstrated its success in many other soft tissues (artery, heart, etc.), was modified and used to simulate the adaptive remodeling within the bladder wall driven by bladder outlet obstruction. Our long-range objective is to improve patient care and develop novel treatments. This present work provides insights on mechanisms of bladder function and remodeling that lay the necessary foundation for the next steps toward this goal.

Table of Contents

List of Tables

List of Figures

Preface

It is a genuine pleasure to express my deep sense of thanks and gratitude to my advisor Dr. Anne M. Robertson for her continued support and guidance throughout my Ph.D study and research. She is a great scientist and her patience, enthusiasm, and immense knowledge have encouraged me in all the time of my academic research. I would like to thank all my committee members, Dr. Paul Watton, Dr. Lori Birder, Dr. William Slaughter and Dr. Patrick Smolinski for their guidance and insightful comments.

My sincere thanks also go to our collaborators. Dr. Watton has always provided insightful computational ideas and huge support on the writing of papers. Also, I'm very grateful for the opportunity to visit Dr. Watton's group at University of Sheffield to learn about a novel growth and remodeling theory. Dr. Watton's student, Giulia, has offered a lot of help during my visit in Sheffield. Dr. Birder provided aged and treated samples for the mechanical testing and Dr. Yoshimura provided outlet obstructed bladder tissues as well as in-vivo data from cystometry study. Dr. Watkins provided technical support for microscopic imaging.

I would like to thank my lab mates, Xinjie, Chao, Piyusha, Mike, Sara, Ricardo, and Yas. It's a great pleasure to work with you and thank you all for letting me have a wonderful time in my Ph.D. journey. I am sure that the memory will last forever and shine forever. I miss you all!

Last but not least, many thanks to my parents for giving me my life and guiding me to understand the beauty of life. I would also like to thank my wife for always being supportive. I'm grateful to have her with me and growing up with me.

1.0 Introduction

The human bladder is a highly compliant organ that allows it to store a high volume of urine under low pressure. Structurally, it is a layered composite with passive components (elastin, collagen fibers, and smooth muscle cells) as well as active components (smooth muscle cells). The components are distributed in laminated structures within the bladder wall that are typically grouped into three layers, Fig. 1. Moving from the lumen, these are the mucosa, the muscularis propria (herein referred to as the detrusor smooth muscle (DSM) layer and the adventitia. The mucosa is composed of a urothelium, a basement membrane, and a lamina propria (LP). The LP contains a densely packed, interwoven network of collagen I and III fibers ([27] and [17]). The DSM is a composite of smooth muscle bundles intermixed with type III collagen fibers and elastin fibers. Collagen fibers are believed to interconnect the smooth muscle cells (SMC) within the bundles ([27]) and are less densely packed than in the lamina propria layer. The outer surface of the bladder is formed of loose connective tissue commonly termed the adventitia.

The main function of the bladder, a hollow organ, is to store and empty urine. During filling, the unfolding of the tissue layers allows the bladder to expand at low pressure. After the full capacity is reached, the contraction of the muscle cells is triggered to generate active stress and initiate flow by overcoming the urethra resistance.

The lower urinary tract symptoms (LUTs), indicative of the increase of urination frequency, urgency, and incontinence, can cause significant morbidity and dramatically lower quality of life for those affected [34] [24]. It is a common disease in later life; 50 - 75% of men over age 50 and 80% of men over age 70 experience LUTS [26] and is usually triggered by one or more bladder disorders such as bladder outlet obstruction, detrusor disorders, urinary incontinence, non-compliant bladder. Although morphological changes such as smooth muscle hypertrophy and collagen fibrosis have been commonly observed in dysfunctional bladders, the effect of these changes on the bladder mechanical function have not been fully explained.

Urodynamics or urodynamic testing is the gold standard to assess how the bladder and urethra are performing their job of storing and releasing urine. It replicates the filling

and voiding functions and allows the quantification of vesical and abdominal pressures, and measures the flow of both to and from the bladder through the use of urethral and rectal catheters. While the urodynamic studies provide a method of quantifying the mechanical functionality of the bladder, these invasive tests are very subjective and do not always reveal underlying disorders responsible for patient symptoms which could result in costly follow-up procedures or inefficient treatment. It is envisaged that *in silico* models of the bladder will offer new clinical tools to assist diagnosis, management, and treatment of bladder disease.

In this work, we integrated in situ mechanical testing and multiphoton microscopy to assess bladder mechanical properties while observing the microstructure transformation and using our experiment to inform the development of a novel mathematical model. Using this model, we aim to understand the mechanical function from a microstructural perspective and the growth and remodeling of bladder with and without pathology. In order to achieve the overall goal, we plan to work on three main objectives.

1. **Identify the effect of morphological changes on bladder compliance** The bladder compliance decreases with age and disease. The loss of compliance not only diminishes the bladder capacity but also raises the filling pressure which can be transmitted to the kidney and cause renal insufficiency. The loss of compliance was found to have a strong correlation with morphological changes such as smooth muscle hypertrophy and collagen fibrosis [16, 17]. However, the impact of these morphological changes on the wall properties remains unknown. The structural changes that are primarily responsible for decreased compliance will be investigated by combing mechanical testing and multiphoton imaging.
2. **Understand the bladder mechanical function from urodynamics** While the urodynamic studies provide a method of quantifying the mechanical functionality of the bladder, these invasive tests do not always reveal underlying disorders responsible for patient symptoms resulting in costly follow-up procedures, or inefficient treatment. To increase diagnostic success or replace invasive procedures with non-invasive alternatives, mathematical models have been developed and employed as a predictive tool to understand the underlying mechanism of bladder function.

3. **Understand the bladder growth with and without pathology** Among the non-compliant bladders, the change of mechanical properties is highly relevant to the physiological changes such as bladder outlet obstruction (BOO). These symptoms indicate the changes of intramural pressure could drive the remodeling that leads to bladder wall stiffening. To understand this process, the effect of intramural pressure on bladder wall changes (e.g. size and wall thickness) have been simulated with a novel growth model.

2.0 Layer Dependent Role of Collagen Recruitment during Loading of the Rat Bladder Wall

The work in this chapter was largely reproduced from the following manuscript [20] with permission granted by Biomechanics and Modeling in Mechanobiology (BMMB):

Cheng, F., Birder, L.A., Kullmann, F.A., Hornsby, J., Watton, P.N., Watkins, S., Thompson, M. and Robertson, A.M., 2018. Layer-dependent role of collagen recruitment during loading of the rat bladder wall. Biomechanics and modeling in mechanobiology, 17(2), pp.403-417.

2.1 Introduction

The human bladder is a highly compliant organ that can expand from an empty state to store 450 $\pm$ 64.4 ml of urine at relatively low pressures of 43.5 $\pm$ 7.3 cm of H_2O in young adults (18 yrs) [49]. This is quite remarkable given the low extensibility of the collagen fibers that make up the bulk of the extracellular matrix in the bladder wall. However, the compliance of the bladder wall can decrease with age and disease [48, 52]. This increased stiffness not only diminishes the bladder capacity but also results in increased filling pressures that are transmitted to the kidney and can cause recurrent infection, abdominal pain and, in severe cases, reflux nephropathy or chronic kidney failure [7, 91]. Hence, it is of great importance to understand the mechanical source of the bladder extensibilty and how this functional property is changed during aging and disease.

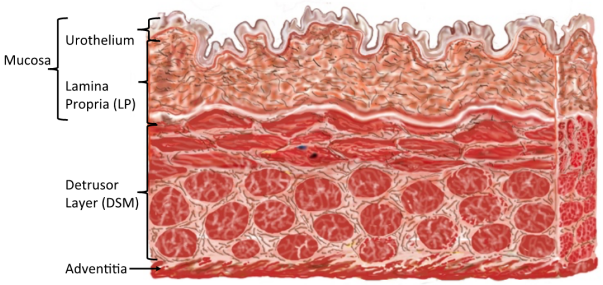

Figure 1: Schematic of a cross section of the bladder wall showing the three major layers (mucosa, detrusor smooth muscle layer and adventitia). The folds (rugae) of the mucosa layer involve both the urothelium and LP layers. Smooth muscle bundles are shown aligned in two layers within the DSM.

Structurally, the bladder wall is a layered composite with passive components (elastin, collagen fibers and smooth muscle cells) as well as active components (smooth muscle cells). The components are distributed in laminated structures within the bladder wall that are typically grouped into three layers, Figure 1. Moving from the lumen, these are the mucosa, the muscularis propria (herein referred to as the detrusor smooth muscle (DSM) layer and the adventitia. The mucosa is composed of an urothelium, a basement membrane and a lamina propria (LP). The LP contains a densely packed, interwoven network of collagen I and III fibers [27, 17]. The DSM is a composite of smooth muscle bundles intermixed with type III collagen fibers and elastin fibers. The collagen fibers are believed to interconnect the smooth muscle cells (SMC) within the bundles [27] and are less densely packed than in the lamina propria layer. The outer surface of the bladder is formed of loose connective tissue commonly termed the adventitia.

Even though it is generally accepted that bladder compliance is of tremendous clinical importance, a small number of studies performed nearly two decades ago are the main source of information on the physical source of bladder wall extensibility.

In 1992, Ewalt et al. published what appears to be the first conjecture as to the source of bladder compliance, attributing bladder extensibility to folds in the LP collagen fibers,

[27]. They conjectured the wavy LP fibers have little resistance to straightening, enabling the bladder to undergo large changes in volume with small increases in pressure. They attributed the bladder filling capacity entirely to the LP layer, and in particular to the volume at which the LP collagen fibers are engaged.

[17] explored the conjecture of Ewalt et al. by analyzing the collagen fibers in bladders filled to 0%, 25%, 50%, 75% and 100% of their total capacity. They similarly attributed bladder capacity entirely to the lamina propria and made a second conjecture that the mechanical role of the detrusor layer is to simply serve as "the limiting or girding layer to prevent over-distension of the bladder wall". This emphasis on the LP layer as the limiting factor for wall compliance was primarily supported by a comparison of estimates of the maximum tension of the lamina propria and detrusor layer [75] and their change in thickness during filling [17]. These conjectures, while often referenced, have not been reevaluated, (e.g. [3, 6]) with the exception of recent uniaxial work on mouse bladder [46]. Hence, there is a need for further direct evidence to prove or disprove these conjectures.

While there is a lack of direct measurements of the varied mechanical roles of the LP and DSM layers during bladder filling, changes to the extracellular matrix have been associated with altered mechanical function. For example, [27] found that, in the non-compliant bladders of children (≤ 14), the interfascicular space (between SMC bundles) accumulates type III collagen fibers and elastin. They postulated these changes prevent normal expansion of the detrusor layer and thereby affect bladder compliance. Non-compliant bladders have also been studied in the context of spinal cord injured and partial bladder obstruction [19]. In these settings, non-compliant bladders were found to have increased density and volume of smooth muscle cells [42], increased quantities of elastin, and decreased collagen fibers in the detrusor layer [57, 51]. The ratio of collagen types I and III as well as collagen fiber orientation were also found to be significantly different in the detrusor layer of the non-compliant bladder relative to the compliant [51, 17, 27]. These changes were speculated to directly or indirectly cause the loss of bladder compliance.

In this work, we make use of advances in bioimaging coupled with mechanical testing to revisit these two conjectures. In particular, the purpose of the current study is to investigate the relationship between bladder wall structure and compliance during loading using recently

developed imaging tools that enable concurrent imaging of collagen fibers and mechanical testing in intact, unfixed bladder samples [43]. We developed a planar biaxial system compatible with multiphoton imaging (MPM) that enables imaging of collagen fiber recruitment during simulated bladder filling - approximated as a planar biaxial deformation. The structural and mechanical data were quantified and used to evaluate the mechanisms responsible for compliance and loss of compliance in rat bladders. Attention was given to changing roles of the wall layers during loading from zero strain through supraphysiological levels.

An enhanced understanding of the structural mechanisms responsible for bladder compliance will guide the development of novel medical treatments of bladder dysfunction, and provide design objectives for tissue engineered bladders aimed at mimicking the remarkable compliance of the bladder [68]. Furthermore, this study will identify the structural milieu of the intramural cells, knowledge that is essential for understanding the growth and remodeling process in health and disease [3].

2.2 Methods

2.2.1 Tissue Preparation

Nine male Fischer rats (Species F344, adult and aged rats from National Institute on Aging of the NIH) were used in this study, separated by age with 4 adult rats (12 months) and 5 aged rats (21-24 month). The unloaded meridional length (h_o) and diameter (w_o) were measured in the explanted bladder. The bladders were then cut open longitudinally and trimmed into square pieces with widths of 6mm $\pm$ 1mm such that the sides of the samples were aligned with the in situ longitudinal and circumferential directions, Figure 2a.

To inhibit smooth muscle cell contraction, samples were immersed in Hanks Buffer Salt Solution (HBSS) containing, (in mM) NaCl 138, KCl 5, KH2PO4 0.3, NaHCO3 4, MgCl2 1, HEPES 10, glucose 5.6, with pH 7.4, 310 mOsm/l) without calcium and with added EDTA (0.5mM). The voltage calcium channel blocker nifedipine (5uM; Sigma) and the SERCA pump inhibitor, thapsigargin (1uM; Tocris Biosciences), which prevents the reloading of intracellular calcium stores, were also added.

2.2.2 Mechanical Testing and Constitutive Modeling

Mechanical testing was performed using a custom biaxial system specifically designed for testing bladder tissue concurrent with imaging under a multiphoton microscope, Figure 2. This design enabled imaging of collagen fibers in intact specimens without staining or fixation. In the biaxial system, displacement can be independently controlled by four actuators (Aerotech, Inc., linear actuator ANT-25LA) and force measurements are performed using load cells on two of the actuators (Transducer techniques, nonrepeatibility 0.05% of R.O., capacity 5 lbs), Figure 2b. Tissue is mounted on the device using biorakes (World Precision Instruments, Inc.). The biaxial system includes a CCD camera and a 45 degree offset mirror to enable imaging of strain markers from beneath the mounted tissue, Figure 2d,e. This imaging system enables MPM imaging at prescribed biaxial strains.

Prior to testing, the unloaded thickness t_o of each sample was measured in 5 positions using a 0-150mm digital caliper (Marathon watch company Ltd) and averaged. Fiducial strain markers (Basalt microspheres, 425-500 μm, Whitehouse Scientific) were attached to the abluminal side of each sample for strain calculation. During testing, the square sample was first loaded lumen side up on the biorakes, Figure 2b. Following [90], a tare-load was applied to the sample after which it was preconditioned, then unloaded, then loaded to the tare-load, then mechanically tested. Five consecutive equibiaxial loading cycles to a stretch of 1.8 were used for preconditioning with a tare-load of 0.02N. The post-precondition tare-loaded state is used as reference configuration. The lumen surface was imaged under MPM at stepwise increases in strains, Figure 2c, (Section 3.2.1.5). To avoid tissue damage while obtaining a large range of strain, loading was stopped after collagen fibers were visibly

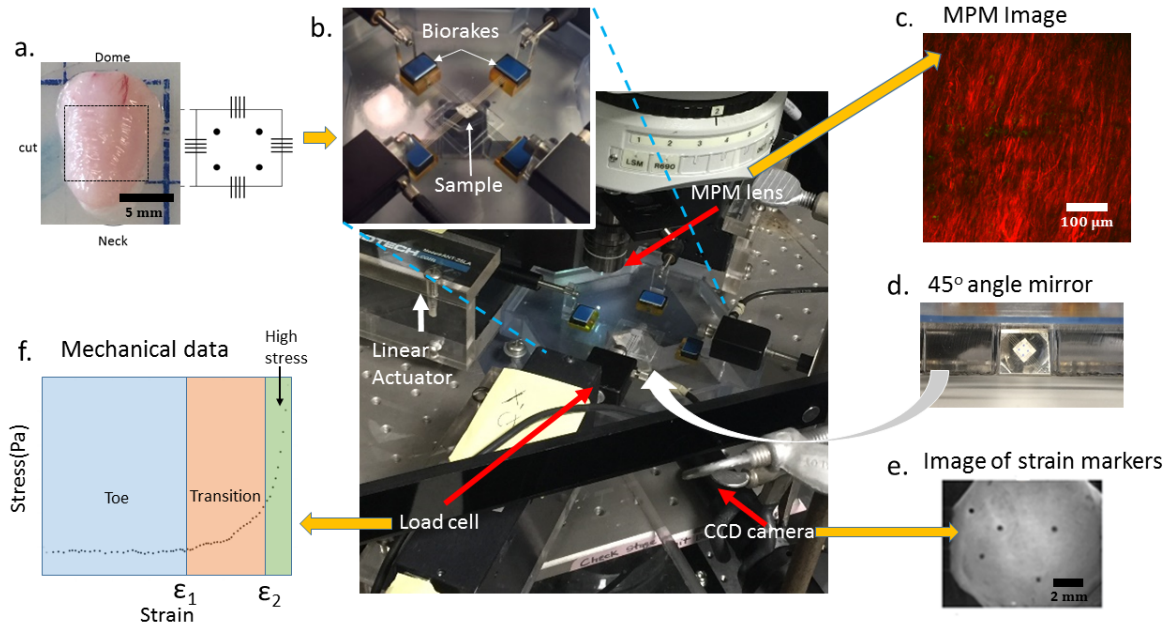

Figure 2: Schematic of experimental system developed for mechanical testing and bioimaging of bladder samples. Yellow arrows indicate input (one) and output (three) for the system. (a) Bladder and schematic of of square tissue sample (input), (b) Biaxial testing system under MPM lens with insert showing magnification of tissue loaded on biorakes, (c) Representative projected stack of images showing second harmonic generation signal from MPM imaging (output), (d) Image from 45^o mirror showing underside of loaded sample, (e) Image from CCD camera showing strain markers imaged using mirror system (output), (f) Representative loading stress strain curve showing toe, transition and high stress regimes of curve obtained using mechanical testing system (output).

straightened (recruited) where it is defined as the maximum stretch. Hence, an individual maximum stretch was identified for each sample. After lumen side imaging, 5 equibiaxial loading cycles at a strain rate of 1% s^{-1} to the maximum stretch were performed with the strain marker locations recorded by a CCD camera using the 45 degree mirror block beneath the sample (Figure 2d,e) and used to obtain the loading curves. The sample was then flipped and the imaging was repeated from the abluminal, once again until collagen recruitment was observed. The components of the Green-Lagrange strains were calculated from the fiducial marker locations using a finite element interpolation method [70]. Components of the Cauchy stress tensor were calculated using load measurements with estimates of current cross sectional area obtained from the strain measurements under the approximation of isochoric motion.

The rat bladder was modeled as an incompressible, hyperelastic, isotropic material with Cauchy stress tensor

$$\underline{\sigma} = -p\underline{I} + \mu\, e^{\gamma(I_1-3)}\underline{B} \tag{2.1}$$

where p is the Lagrange multiplier associated with incompressibility, I_1 is the first invariant of the left Cauchy-Green deformation tensor $\underline{B}$, μ is the shear modulus and material constant γ controls the exponential dependence on I_1. An exponential dependence on stretch was proposed by [30] and the form in (2.1) is commonly used for soft biological tissues. Data sets for the planar biaxial loading studies were combined for the longitudinal and circumferential directions and used to obtain the material constants in (2.1).

2.2.3 Calculation of Bladder Compliance and Capcity

The International Continence Society (ICS) defines bladder compliance C as

$$C = \frac{\Delta V}{\Delta P} \tag{2.2}$$

(given in units of ml per cm of H_20) where ΔP is the change in intraluminal pressure between two different loading states and ΔV is the corresponding change in volume [2].

The initial loading state is chosen as the start of filling while the second and higher loading state is either the cystometric capacity or the state immediately before any muscular bladder contractions have started (that would lead to substantial bladder leakage). Cystometric capacity is defined as the bladder volume when the patient has a normal desire to void, [2].

In this work, consistent with the ICS definition for compliance, we consider the two states to be the zero pressure state (P_o) and the cystometric pressure (P_1) set equal to 45 mmHg for rats, [4]. The corresponding volumes are denoted V_o and V_1, respectively. The bladder capacity is simply V_1, namely, the amount of urine the bladder can hold at the cystometric pressure. Since the compliance is calculated for a fixed cystometric pressure for a given population, the compliance for this population is simply the bladder capacity multiplied by a constant.

We used animal specific values for the unloaded volume (V_o) that were based on measurements of the bladder geometry. An effective unloaded radius r_o of a idealized spherical membrane was then calculated from width (w_0) and height (h_0)

$$r_o = \frac{1}{8}(w_o h_o)^{1/3}. \tag{2.3}$$

The corresponding loaded volume was estimated from the analytic solution for pressure inflation of a spherical membrane [11] with bladder specific material constants obtained from the planar biaxial studies. In particular, the intraluminal pressure for the exponential model as a function of stretch λ

$$P(\lambda) = \frac{2t_o}{\lambda r_o}\,[1 - \frac{1}{\lambda^6}]\mu e^{\gamma(I_1-3)} \tag{2.4}$$

where λ is the ratio of the current radius to r_o.

2.2.4 Assessment of Regimes of the Loading Curve

Following the approach of [70], the intramural stress in the bladder wall corresponding to the maximum filling pressure is 100KPa, which is estimated from an equilibrium balance for a sphere (Laplace's law). Using the exponential fit, loading curves were extrapolated to this maximum load with corresponding maximum strain, (ϵ_{max}) and strain, $\epsilon = (\lambda^2 - 1)/2$. The average curve for each of the principal directions was calculated and divided into 3 regimes: toe regime, transition regime, and high stress regime as follows. To determine the strain defining the end of the toe regime, first a linear fit of the data starting from the origin was performed with an R^2 of 0.99. The toe regime, or low stress regime was then defined by strains in the range [0,ϵ_1), where ϵ_1 is the strain at which the loading data deviates from the linear fit by 450 Pa. The high stress regime was defined as $\epsilon \in (\epsilon_2, \epsilon_{max}]$, Figure 2f. Here ϵ_2 was similarly defined relative to a linear fit to the data with an R^2 of 0.98, in this case, beginning with the maximum of the high stress data rather than the origin. The transition regime was defined as the intermediate regime, $\epsilon \in [\epsilon_1, \epsilon_2\ ]$, Figure 2f.

2.2.5 Multiphoton imaging

Tissues were scanned with multiphoton imaging using a Z step size of 2 μm, following methods in [43]. Briefly, a multiphoton microscope (Olympus FV1000 MPE) equipped with a Coherent Chameleon TiSapphire pulsed Laser was used to image collagen fibers. An excitation wavelength of 800 nm and 1.12 NA 25 x MPE water immersion objective were used for all samples. Signals from second harmonic generation (SHG) were collected using a 400 nm emission filter with a $\pm$50 nm spectral bin.

2.2.6 Evaluation of Fiber Recruitment from Multiphoton Images

Multiphoton image stacks were used to obtain 3D reconstructions of the collagen fiber architecture that were mapped to the corresponding point on the loading curve by matching the loading level. Collagen fibers could be clearly imaged up to depths of approximately 200 μm in unloaded samples. Collagen fibers were traced in 2D slices through the depth of the

3D reconstructed model (Filament function in Imaris, Bitplane, Switzerland), Figure 3, [43]. Fiber arc length (s) was determined for each fiber tracing. Cord length (L) was defined as the length of a best linear fit line to the same segment. Fiber straightness was defined as the ratio of chord length to arc length L/s [43]. A fiber was designated as recruited to load bearing when its straightness reached 0.98 [43, 44]. Careful attention was given to assuring the fiber straightness results for each sample at each load were independent of the number of fiber tracings. In particular, a mean value of straightness of the first j tracings was defined as,

$$m(j) = \frac{1}{j}\sum_{i=1}^{j}\frac{L(i)}{s(i)} \quad j = 1, 2, 3, \cdots n \tag{2.5}$$

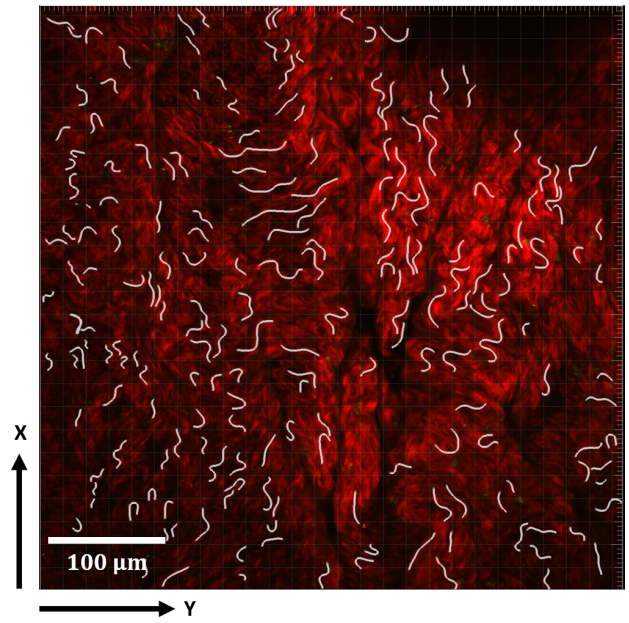

Figure 3: Collagen fiber tracings shown in white in a 2D projection of a representative 3D reconstructed model formed from 2D multiphoton stacks. MPM signal from collagen fibers seen in red.

The difference between the calculated straightness for $j+1$ tracings and j tracings was defined as a residual of $m(j)$:

$$e(j) = \frac{m(j+1) - m(j)}{m(j+1)}, \quad j = 1, 2, 3, \cdots n-1 \tag{2.6}$$

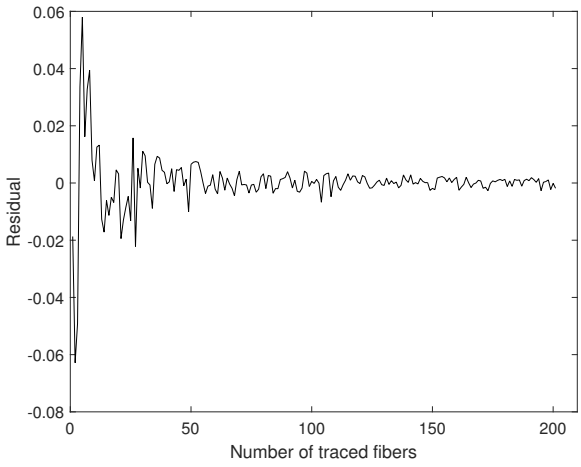

Figure 4: Residual $e(j)$ as a function of number of fibers considered in calculating fiber straightness. Definition of residual is given in Eq. 2.6

When the residual satisfied abs$[e(j)] < 0.005$, the number of fiber tracings was deemed sufficient to evaluate fiber straightness. A representative plot for $e(j)$ is shown in Figure 4 and illustrates how the bounds on the residual diminish with increasing number of fiber tracings, tending toward zero.

We developed a method to evaluate measured mean straightness and recruited fiber percentage as a function of different bins of fiber length, Table **??**. We tested this for one of the sample adult02 and found the variance (sample standard deviation) is less 1.7 %. Namely, the results were almost insensitive to the range of fiber tracing.

2.2.7 Quantification of the Flattening of the Lamina Propria

The mucosa of the unloaded bladder wall is wavy, Figure 1, and gradually flattens under load. The flatness/waviness of the LP was assessed in 3D reconstructions of the MPM images by calculating the vertical position of the surface. The lamina propria was defined to be flat when the standard deviation of the vertical position was less than 20 microns.

Table 1: Mean fiber straightness and recruited fiber percentage at different fiber tracing length range.

Fiber length	20∼100 microns	30∼100 microns	40∼100 microns	50∼100 microns	Average over all bins
Mean fiber straightness	0.76	0.82	0.81	0.80	0.80 ± 0.023
Recruited fiber percentage	7.1%	8.1%	7.6%	7.6%	7.6 ± 0.41

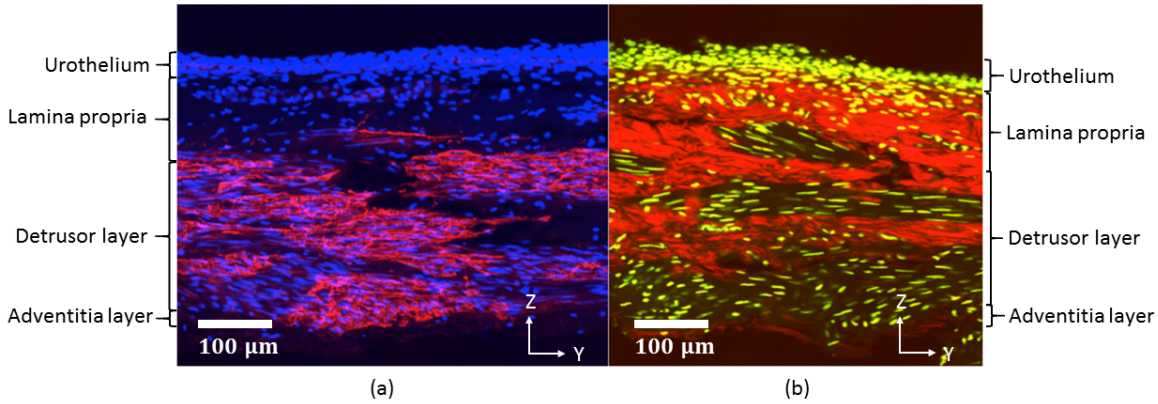

Figure 5: Bladder cross section imagined using (a) Confocal microscopy and (b) Multiphoton Microscopy. In (a), cell nuclei are shown in blue (DAPI), while red shows regions positive for αSMA. Cell nuclei are yellow in (b) with collagen fiber signal in red. The y-z plane corresponds to the longitudinal and transmural directions, respectively. Lumen side is on the top of the image.

2.2.8 Immunohistochemistry

Immunofluorescent (IH) staining was performed to identify regions of smooth muscle cell bundles and location of cell nuclei, following established protocols from the Center for Biologic Imaging (CBI), (details can be found at www.cbi.pitt.edu/Protocols.htm). Briefly,

after preparing the square sample for mechanical testing, a portion of the remaining tissue was fixed in 4% PFA (paraformaldehyde). Cross sections were obtained by freezing the specimen in OCT and 2 μm thick slices were cut using a cryostat (HM 50SE, Microm). The sample was incubated (diluted by 1% NGS) with primary antibody for αSMA (Sigma C6198). To stain cell nuclei, the slices were then washed with 1X PBS 3 times and incubated without illumination in DAPI (4′,6-diamidino-2-phenylindole, 1:1000, Life Technologies). All sections were then imaged using Olympus Fluoview 1000 confocal microscopy (Olympus Imaging America, Melville, NY). A neighboring section similarly stained with DAPI but without antibody for αSMA was imaged using multiphoton microscopy.

2.3 Results

2.3.1 Overview of Collagen Fiber and Cellular Distribution across the Wall Layers

To provide context for discussions of the enface images of collagen fibers, a cross section of the rat bladder is provided in Figure 5, with IH staining imagined under confocal microscope and a neighboring section imaged using MPM. Figure 5(a) shows cell nuclei (blue) and αSMA positive regions in red whereas Figure 5(b) shows the cell nuclei (yellow) and collagen fibers (red). In Figure 5(a), moving from the lumen downwards, the cell density diminishes as one moves through the mucosa from the urothelium to the lamina propria. The adjacent detrusor layer has large regions of αSMA positive staining indicating areas of smooth muscle bundles. Sparse cell nuclei can be seen in the adventitial layer. In Figure 5(b), consistent with Figure5(a), the urothelium layer has a dense display of cell nuclei. Under MPM, the collagen within the lamina propria can be seen. Moving into the detrusor layer, regions of dense collagen fibers are interspersed with regions populated with cells corresponding to regions of smooth cell bundles in Figure 5(a). Further outwards, the collagen within a thin adventitial layer can be seen. This sample has been gently flattened before fixation, so waviness is not seen in the mucosa layer.

2.3.2 Mechanical Response of the Bladder Wall

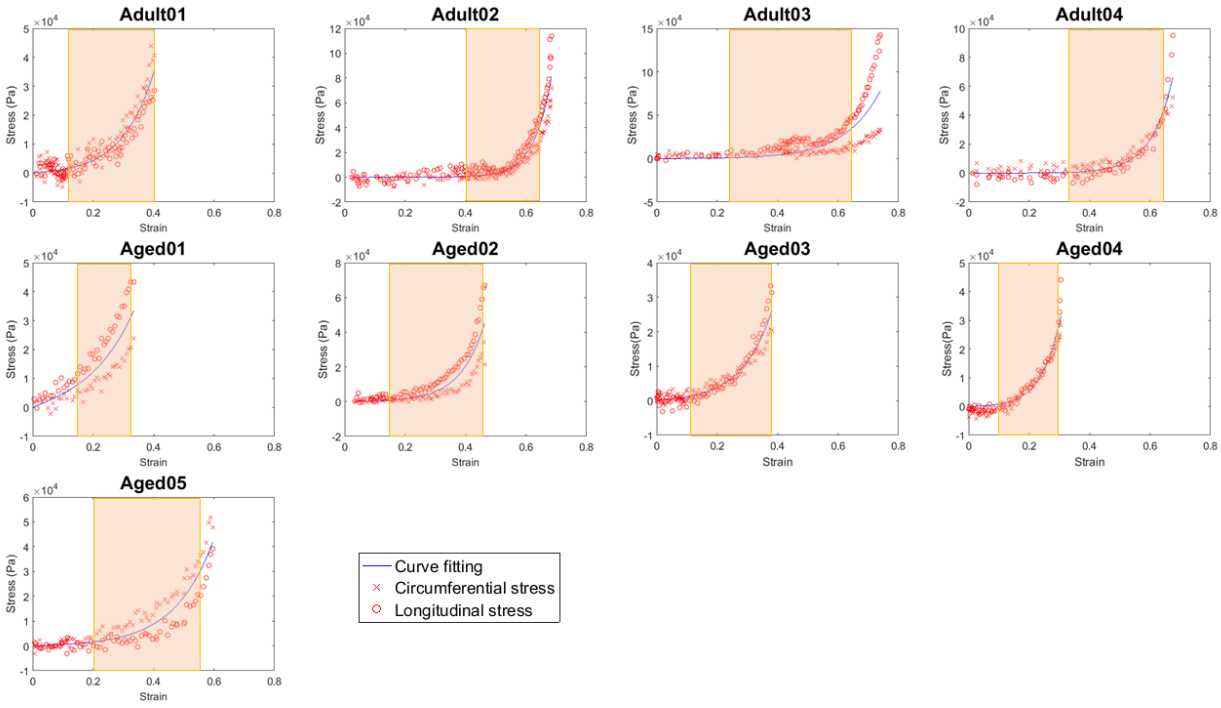

Figure 6: Mechanical loading curves for bladder tissue showing Cauchy stress as a function of strain (ϵ) with biaxial raw data (red) and exponential model of the averaged data of two directions from Eq. 2.1 (blue). Material parameters in Table **??**. The transition regime for each curve is delineated by a colored rectangle. High stiffness regime following the transition regime inhibits further extension.

The raw data for the biaxial testing for each sample are shown in Figure 6, averaged for the longitudinal and circumferential directions. This data was well fit by the exponential model (2.1) with an $R^2 > 0.94$ for all samples, Table **??**.

2.3.3 Two Bladder Wall types Identified based on Wall Extensibility.

The strains ϵ_1 and ϵ_2 at the interface between the three loading regimes (toe, transition, and high-stress regimes) are given in Table **??**. Two different categories of bladder were defined based on these strains. In particular, the method of k means clustering was used to

Table 2: Mechanical properties for each bladder sample. Material constants μ, γ and corresponding R^2 for fit of constitutive model in Eq. 2.1 to data shown in Figure 6. Strains ϵ_1 and ϵ_2 separate the low strain, transition and high strain regimes of the loading curve.

Sample	μ (Pa)	γ	R^2	ϵ_1	ϵ_2	Type
Adult01	4635	2.2	0.95	0.13	0.40	II
Adult02	22	4.2	0.98	0.40	0.63	I
Adult03	625	2.0	0.94	0.24	0.64	I
Adult04	90	3.3	0.98	0.34	0.64	I
Aged01	11,015	1.4	0.99	0.15	0.34	II
Aged02	1814	2.9	0.98	0.16	0.44	II
Aged03	4050	2.2	0.98	0.13	0.38	II
Aged04	7720	3.7	0.96	0.11	0.28	II
Aged05	1500	1.8	0.98	0.20	0.57	I

partition the $n = 9$ observations into $k = 2$ clusters, where each observation belongs to the cluster with the nearest mean. Type I has mean values $(\epsilon_1 = 0.29, \epsilon_2 = 0.62)$, while Type II has means $(\epsilon_1 = 0.14, \epsilon_2 = 0.37)$, Table **??**. A student T-test showed these groups were statistically distinct, (p=0.039 for ϵ_1, and p=0.00016 for ϵ_2). Type I wall is more extensible due to longer toe regimes (larger ϵ_1) and larger strains before the onset of the high stress regime (ϵ_2). These differences can be seen visually for each bladder in Figure 6 and for the combined data set in Figure 7. The blinded separation of the samples into two wall types is clearly seen in Figure 7, where data for Type I are shown in green and for Type II in red.

2.3.4 Bladder Compliance can be Maintained Despite Increased Wall Stiffness

The bladder capacity, defined here as the bladder volume at cystometric pressure, is an important variable for the health of the animal since it determines how much urine can be stored comfortably before voiding. As noted earlier, bladder compliance and capacity are proportional for a fixed cystometric pressure. It follows from a simple equilibrium balance that reduced capacity can arise due to increased stiffness (μ, γ), decreased volume (V_o) and/or increased wall thickness t_o. The average compliance (and hence capacity) of the more extensible Type I bladders is nearly twice that of Type II bladders and these groups are statistically distinct (p=0.0038), Table 2.3.4 and Figure 8.

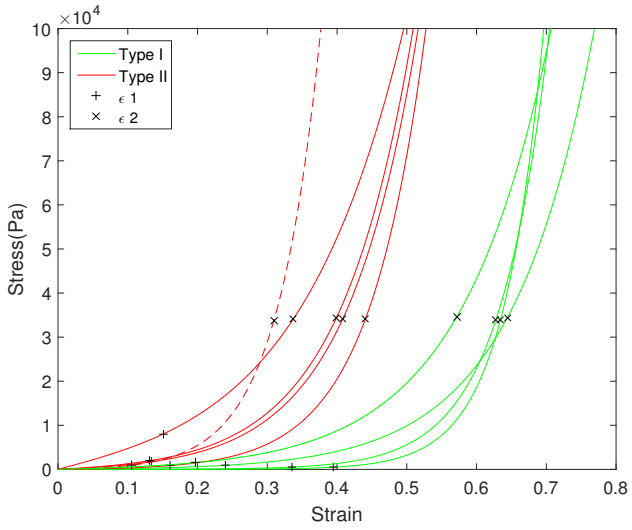

Figure 7: Cauchy stress as a function of strain for wall types I (green) and II (red) corresponding to composite of curves from Figure 6. The strain at the end of toe regime (ϵ_1) and end of transition regime (ϵ_2) are designated by "+" and "x', respectively.

Two of the (Type II) bladders (Aged02 and Aged03) maintained a relatively large capacity (compliance) despite lower extensibility through increased V_o, Figure 8 and Table 2.3.4. The wall thickness was within one standard deviation of the average for Type II walls and therefore did not play a large role in maintaining a high bladder capacity. These two bladders had the largest unloaded volumes of the entire cohort and V_o was more than 30% greater than the average volume of the Type I bladders, Table 2.3.4. As a result, the capacities of these Type II bladder were within 70% of the average for Type I bladders. In contrast, the other three Type II walls were not enlarged relative to the Type I bladders and their capacities were reduced to less than 34% of the average capacity for the type I walls.

2.3.5 Relationship between Flattening of Rugae and Bladder Loading Curves

A representative projected stack of MPM images as viewed from the lumen side of the bladder wall in the unloaded state is seen Figure 9(a), The waviness of the unloaded luminal surface (rugae) can be seen with the undulated collagen fibers in red. Since the depth of

Table 3: Comparison of the unloaded wall thickness t_o, unloaded volume V_o, volume expansion V-V_o, and compliance C between the two wall types

Sample	Wall Type	t_o (mm)	V_o (mm^3)	$V - V_o$ (mm^3)	C (ml/cmH_2O)
Adult02	I	0.52±0.02	170	414	0.0069
Adult03	I	0.61±0.04	166	446	0.0074
Adult04	I	0.46±0.05	182	460	0.0077
Aged05	I	0.66±0.03	143	317	0.0053
Average	I	0.56	165	409	0.0068
Std	I	0.09	17	65	0.0011
Adult01	II	0.66±0.03	115	138	0.0023
Aged01	II	0.72±0.03	129	116	0.0019
Aged02	II	0.85±0.02	214	291	0.0048
Aged03	II	0.92±0.04	245	293	0.0049
Aged04	II	1.12±0.04	151	80	0.0013
Average	II	0.85	171	184	0.0031
Std	II	0.18	56	101	0.0017

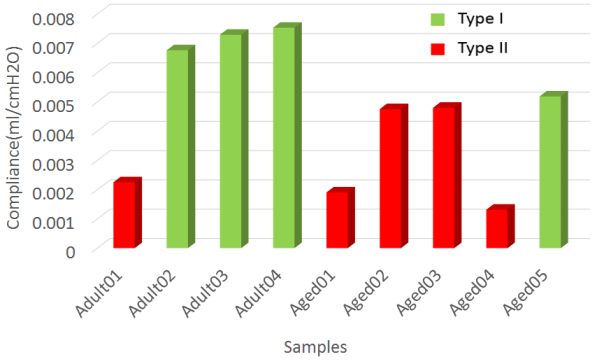

Figure 8: Compliance of Type I (green) and Type II (red) bladder walls.

the stack is less than the depth of the unloaded LP layer, these undulations are truncated, leading to areas absent of the red signal in this projected view. In Figure 9(b), the surface elevation of the luminal surface is shown as a contour plot for the 3D reconstructed stacks in Figure9(a). The surface folds are clearly multi-dimensional, not, for example, ridges running in the longitudinal direction.

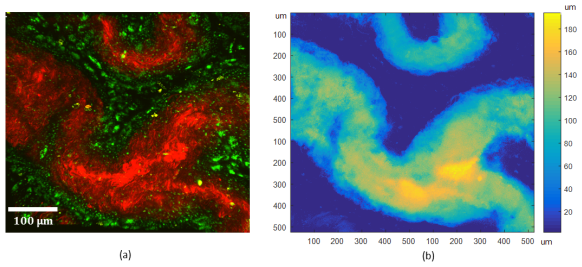

Figure 9: Rugae of the unloaded bladder wall as seen in (a) Projected stack of multiphoton images with collagen fibers in red and (b) Corresponding contour plot of surface elevation with peaks of undulated surface (large z-value) shown in yellow.

2.3.5.1 Rugae are not Flattened until Transition Regime

The regime in the loading curve where rugae were lost for each sample is seen in Figure 10. The two "x" marks denote the strain (y-axis) at which the transition regime begins and ends. The "o" denotes the strain at which the luminal surface was flattened. Since the imaging was done at discrete strain values, for each sample, there is a bar, signifying the largest strain at which the tissue was wavy and the smallest strain at which it was imaged as flat. In all cases, the flattening occurred beyond the toe region, within the transition regime, Figure 10. We found that LPs of Type II walls were flattened at lower strains in general than Type I walls.

2.3.6 Collagen Fiber Recruitment across the Bladder Wall

Figure 11 shows the fiber recruitment with increasing strain as seen in projected stacks of MPM images from both the luminal side (row 1) and abluminal side (row 2). From the luminal side, both the flattening of the undulations as well as the straightening of the collagen fibers in the LP and onset of recruitment can be seen. From the abluminal side, highly coiled fibers can be seen in the DSM layer for the toe regime with gradual straightening of the collagen fibers with increasing strain.

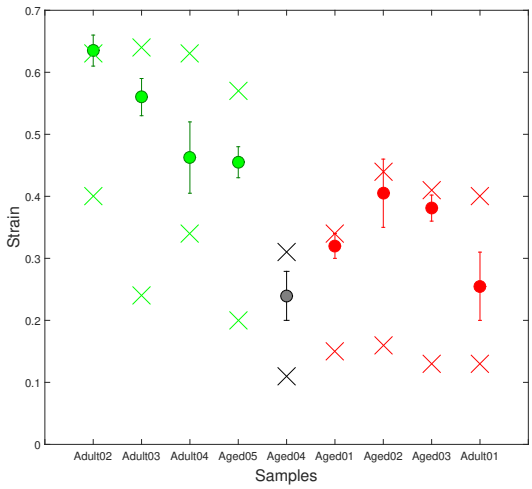

Figure 10: Strain at which the undulations in the luminal surface (rugae) were lost for each of the nine cases. The two "x" marks for each case denote the strain (y-axis) at which the transition regime begins and ends. The "o" denotes the strain at which the luminal surface was flattened. Green, red and black correspond to wall types I, II, and II′, respectively.

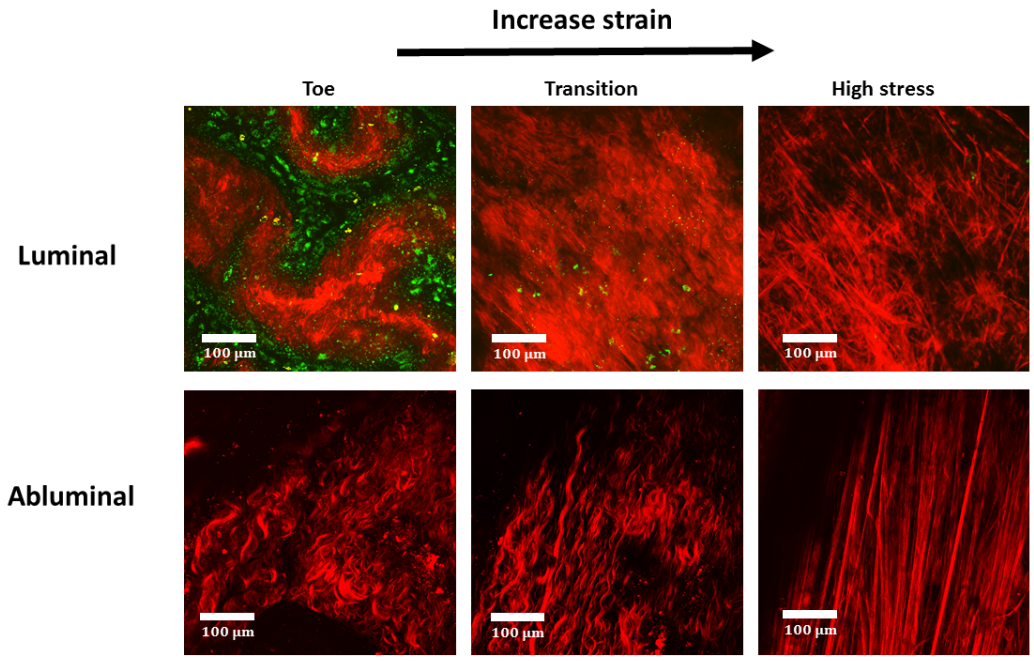

Figure 11: Projected stacks of MPM images showing Adult04 as viewed from the luminal (row 1) and abluminal (row 2) sides. Panels one to three correspond to the toe, transition and high stress regimes, respectively. With increasing strain, undulations (rugae) of the mucosa on the luminal side are flattened (row 1), followed by straightening (recruitment) of the collagen fibers (column 3).

2.3.6.1 LP and DSM Collagen Recruitment is Coordinated in Extensible Bladder Walls

In order to understand the relative role of collagen recruitment in the DSM and LP layers during loading, we quantified the percentage of recruited collagen fibers from both the luminal (lamina propria) and abluminal sides (detrusor layer) and considered these with respect to the toe, transition and high stress regimes, Figure 12.

A representative fiber tracing for the abluminal side was shown in Figure 3. The fraction of recruited fibers at 4 different strain points in each of the LP and DSM layers is shown in Figure 12. Since the MPM images were performed independently on luminal and abluminal sides, the data for the LP and DSM layers are obtained at slightly shifted strains within each regime, and this is reflected in the horizontal location of the recruitment data within a regime.

No fibers were recruited in the toe regime for any of the samples (n=9), Figure 12. In Type I bladders, recruitment of collagen fibers was coordinated in the LP and DSM layers. In particular, collagen fibers from both the lamina propria and detrusor layer began to be recruited in the transition regime and most of the fibers were straightened in both layers in the high stress regime. For all Type II samples except one (Aged04), the recruitment of collagen in the LP and DSM layers was uncoordinated. Namely, few LP collagen fibers were recruited in the transition regime and the recruitment of DSM fibers dominated this regime. The premature recruitment of the DSM collagen continued through the high stress regime for these walls In contrast, the Type II bladder (Aged04) showed a coordinated fiber recruitment to Type I bladders and is referred to as Type II′ wall in further discussions and shown as dashed red lines in Figure 7. The Type II′ wall (Aged04) had the earliest flattening of the LP layer, Figure 10, and the shortest toe regime with $\epsilon_1(\text{II}') = 0.11$, Table **??**.

2.3.7 Aged versus Adult Bladder

The bladders from the adult rats were more likely to be Type I (3 out of 4), whereas the aged bladders were generally Type II (4 out of 5). The aged bladders were thicker than the adult bladders (p=0.019) with averages of 0.89 ± 0.18 mm and 0.56 ± 0.09 mm. The Type I and Type II walls had average thicknesses of 0.56 ± 0.09 mm and 0.79± 0.12 mm, respectively. The Type II′ wall, an aged bladder, was substantially thicker than the other walls, with a thickness of 1.12 mm. In addition, we found the wall thickness of adult samples are negatively correlated (R^2= -0.85) to their initial volume while the aged samples, except for the unusual case Aged04 (Type II′), showed the opposite trend ($R^2 = 0.95$).

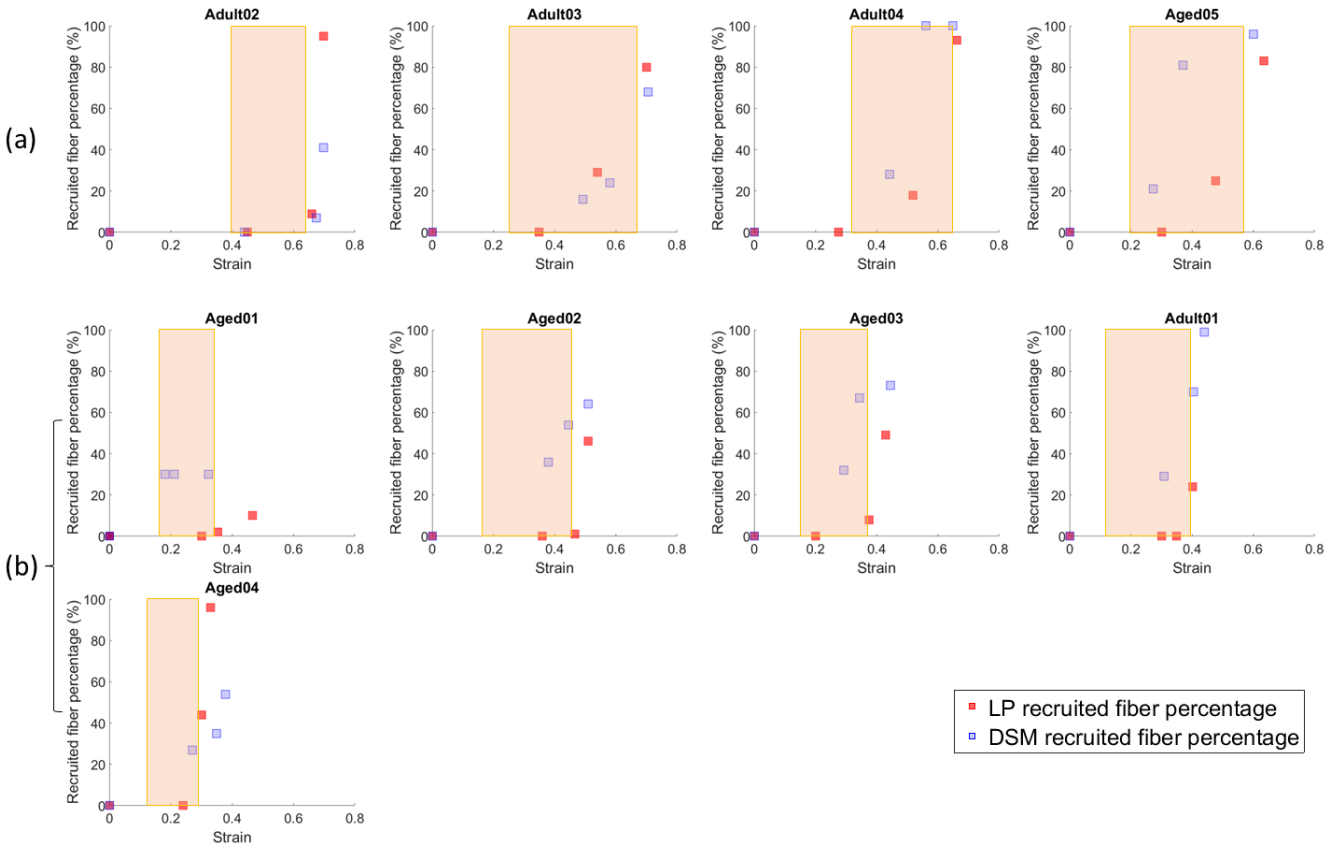

Figure 12: Collagen fiber recruited percentage of the LP layer (red) and DSM layer (blue) plotted with the exponential model fitting curve. The transition regime is delineated by a colored rectangle. High stiffness regime following the transition regime inhibits further extension. (a) demonstrate type I samples. (b) demonstrate type II samples.

2.4 Discussion

The bladder is one of the most compliant organs in the body. For example, a normal rat bladder can expand to about three times its initial volume. The same passive components of the bladder wall, such as elastin and collagen fibers, are also found in the walls of other biological tissues. It is the wall architecture, or the way these components are combined, that must be responsible for its extensibility. In this work, we mainly focus on the passive properties of the rat bladder wall while SMC activity is removed. A custom designed planar

biaxial system compatible with multiphoton microscopy was made to directly investigate the relationship between bladder wall structure and wall extensibility during loading in fresh bladder samples from adult and aged rats.

To understand the changing roles of the wall layers during loading, we defined three regimes for the bladder mechanical loading curves: the toe regime, transition regime, and high stress regime. Since the bladder material stiffness increases so rapidly in the high stress regime the bladder extensibility is largely determined by the length of the toe and transition regimes, Figure 7. Namely, the steep increase in wall stiffness in the high stress regime inhibits further substantial bladder expansion, essentially "locking in" the maximum bladder volume.

2.4.1 Two Wall Types Classified by Extensibility

Within 5 aged samples and 4 adult samples, we found two types of bladders, defined by measures of their extensibility, ϵ_1 and ϵ_2. Type I walls have longer toe regions and later onset of the high stress regime compared with Type II and these differences reached statistical significance. The increased extensibility of Type I walls is mainly due to significantly longer toe regimes than Type II bladders. The average length of the transition regime is also longer, but it does not reach statistical significance.

2.4.2 Mechanisms for Long Toe Regimes

The high extensibility associated with longer toe regimes is only possible if both the inner (mucosa) and outer (DSM and adventitial) layers of the wall are both extensible. In this work, we showed the extensibility of the LP layer is due to folds (rugae) in the bladder wall. With increasing strain the LP gradually flattens with little resistance to load. In parallel, the LP collagen fibers become more planar and eventually begin to straighten. Importantly, the rugae do not fully flatten, nor does collagen recruitment commence until after the end of the toe regime (in the transition regime). Therefore, the bladder wall has two levels of undulations to provide extensibility: wall undulations (rugae) on the order of 100 microns, Figure 9, as well as undulations in the collagen fibers themselves, on the order

of tens of microns. This second level does not engage until the after the first (rugae) are flattened. Previous work has suggested the high extensibility of the outer wall is provided by the architecture of the SMC bundles and collagen fibers. In particular, that in the unloaded bladder the SMC bundles are connected by wavy collagen fibers, [17]. Hence, the reorientation and stretching of the SMC bundles as well as straightening of the wavy collagen fibers are mechanisms that provide high extensibility in the DSM layer. Our results are consistent with this conjecture. In particular, while we did not investigate the connection between the SMC bundles and collagen fibers in this work, we have shown the DSM collagen fibers were not recruited until the transition regime was reached. This is consistent with the proposed mechanism for large extensibility of this layer. A schematic of mechanisms for extensibility of the LP and DSM layers is shown in Figure 14.

2.4.3 Mechanisms Responsible for Stiffening in the Transition Regime of Type I Bladders

In the transition regime of Type I walls, the stress increase is due to the gradual fiber recruitment of fibers in both layers. The fiber recruitment in the LP and DSM layers are co-ordinated in that both layers demonstrate collagen recruitment that continues to substantial levels in the high stress regime, Figure 12 (a).

2.4.4 Physical Mechanisms Responsible for Loss of Bladder Bxtensibility (Type II and Type II′ Walls)

The central difference in the Type II and Type II′ walls compared with the Type I walls was the shortened toe regime. Since the toe regime is a region of high extensibility under low loads, even a small amount of loading of stiff collagen fibers will end this regime and force it to enter the transition regime. We found that Type II bladders have a shorter toe regime because the DSM fibers were straightened prematurely (lower strains than Type I walls), ending the toe regime and preventing extensive recruitment of LP collagen, Figs. 12. In contrast, in the Type II′ wall, fibers from both the LP and DSM layers were recruited prematurely, resulting in the earliest flattening of the LP among all the samples, Figure 10.

As aresult, this case had the shortest toe regime. In Type II walls the early recruitment of DSM collagen fibers prevented the LP fibers from engaging and straightening. In fact, large fractions of LP fibers remained unrecruited even in the high stress regime, Figure 12 (b). In Type II walls, the DSM collagen fibers will take a more dominant role than LP fibers in physiological and supraphysiological load bearing. In one sample (Aged01), we also saw a lack of coordination of fiber recruitment even within the DSM layer itself with some highly recruited fibers preventing continuing recruitment of other still highly tortuous fibers, Figure 13. This is consistent with the unchanging fraction of recruited DSM fibers over the transition regime in that sample, Figure 12 (b).

These findings suggest the DSM layer of Type II walls somehow lost one or more of the mechanisms for structural transformation to accommodate extension before fibers are recruited. Mure and Galdo found an increased ratio of type III to type I collagen in non-compliant bladders [56]. Chang found that in normal bladder, type III collagen localization is largely confined to the interfascicular regions (between SMC bundles) of the detrusor while in non-compliant bladder, type III collagen is found not only in the intrafasciular region, but also within the smooth muscle bundles [17]. The abnormal type III collagen fibers in the SMC bundles may be the cause of the earlier fiber recruitment because they could stiffen the SMC bundles, forcing earlier recruitment of the interfascicular fibers.

2.4.5 Overview of Structure/Function Relationship

The relative roles of the collagen fibers in the LP and DSM layers, including conjectures regarding the role of the connection between SMC bundles and collagen fibers are shown in a schematic in Figure 14. In the toe regime of all wall types, the LP is wavy and no fibers are recruited to load bearing. The DSM layers collagen fibers are drawn to shown an interconnection with smooth muscle bundles (following the conjecture of [16] and further supported by recent work on murine bladder using MPM [46]).

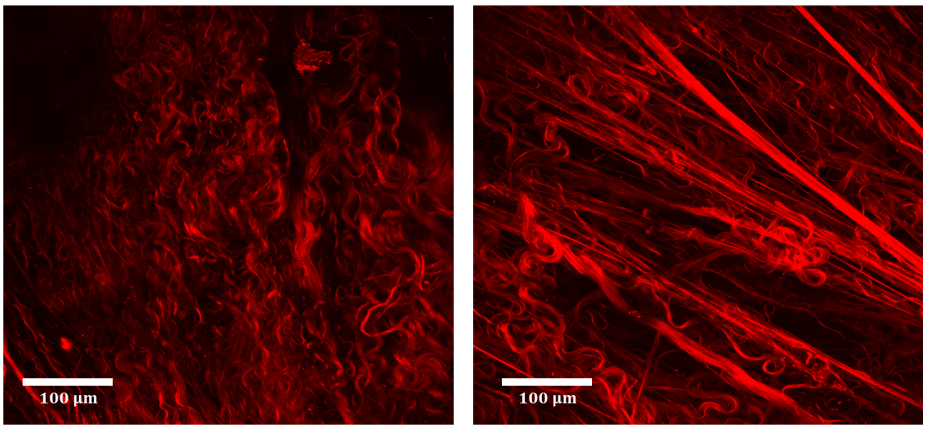

Figure 13: Collagen fibers in Type II wall (Aged01) as seen in projected stacks of abluminal MPM images (a) toe regime and (b) transition regime. Unbalanced fiber recruitment is seen in the DSM where some fibers are fully straightened and others are highly tortuous.

As shown in the present work, during further loading of the Type I wall, the LP layer becomes flattened and collagen fibers in both layers are gradually recruited to load bearing. For Type II walls, the toe regime ends earlier than for Type I walls and the fiber loading is unsynchronized. For Type II walls, some of the DSM collagen fibers become load bearing prematurely inhibiting the strains needed for the collagen in the LP layer to become load bearing.

2.4.6 Elastin in Bladder Wall

Unlike arterial walls, there are no elastic layers (lamellae) in the bladder wall. Rather elastin in the bladder wall has only been reported as small quantities of fibers throughout the lamina propria, and in a loose network around the muscle fascicles (Murakumo 1995). This is consistent with our own findings.

2.4.7 Effects of Aging

The heterogeneous aging process seen across species (with some animals aging more rapidly than others, for example, or in different ways), can confound analysis. For this reason, we looked for wall types based on mechanical response, rather than trends with aging. Despite the small numbers of samples in this study, a high statistical significance was found, demonstrating a propensity for aged walls to be Type II and of increased thickness.

2.4.8 Extensibility, Bladder Capacity and Bladder Compliance

In this work, we have emphasized the need to consider bladder extensibility separately from bladder capacity and bladder compliance. Like other soft tissues such as arteries, the relationship between local stress and strain is highly nonlinear and cannot be captured with a single measure of stiffness. This is particularly important for the bladder, since the the bladder empties and fills during normal filling/voiding cycles. This is in contrast to, for example, an artery wall where the cyclic loading takes place about a largely inflated state.

Bladder compliance, which is often used in the literature on the biology of the bladder wall, is a linear approximation to the bladder pressure/volume relationship. In particular, it is defined as the slope of in vivo bladder volume versus pressure curves, from the unloaded bladder to the bladder capacity (near the leak point). This is a very rough approximation to the mechanical response of the entire bladder. It does not separate out the three regimes of loading, nor consider the wall properties independent of the response of the bladder as a whole. While compliance may be the most amenable measurement in vivo, there are some concerns when it is used ex vivo for assessment of the bladder wall. First, we have shown that the bladder capacity is dominated by the *length* the toe regime, (not even the stiffness in this regime). Secondly, we have found a bladder with a shorter toe region can compensate for low extensibility through an increase in bladder size. Namely, two bladders can have roughly the same compliance, yet one can have a shortened toe region due to uncoordinated recruitment of collagen in the LP and DSM layers.

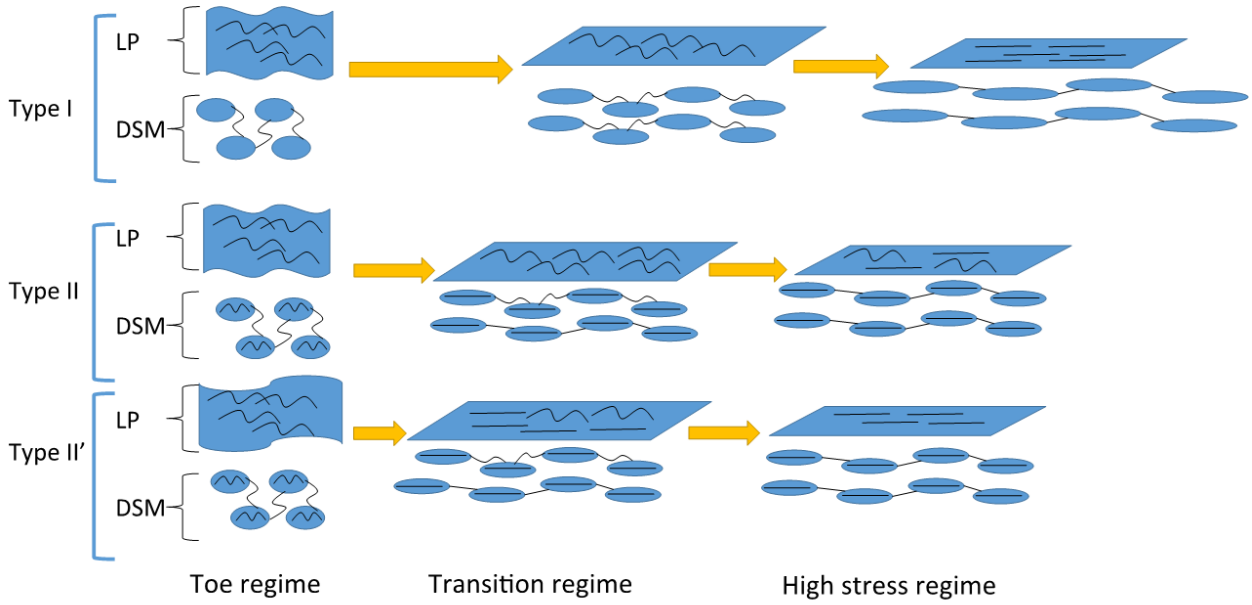

Figure 14: Schematic of the findings for the relative roles of the collagen fibers in the LP and DSM layers by wall type. This figure is a conjectured scheme based on [16] 's assumption on muscle cells mechanism and the findings of infiltration collagen fiber in SMC [17] (conjectured to be a possible reason for the premature DSM collagen recruitment found in our study). In all wall types, extensibility in the toe regime is achieved by flattening of the rugae without fiber recruitment. In the toe regime, the extensibility of the DSM (conjectured by [16]) to arise from the wavy nature of the collagen fibers connecting extensible SMC bundles. For the transition regime of Type I walls, the fiber recruitment in the LP and DSM layers were shown to be coordinated. In Type II walls, the toe region is cut short by early recruitment of the DSM collagen which is conjectured to arise from infiltration of fibers in the SMC bundles as well as other stiffening mechanisms. As a result, complete recruitment of LP collagen is inhibited, even in the high stress regime. In Type II′ walls, although the LP and DSM fiber recruitment is coordinated, the rugae are flattened prematurely, resulting in the earliest recruitment.

2.4.9 Limitations and Future Directions

In this study, we focused attention on a population of male Fischer rats. In future studies, it will be important to extend this study to female rats as well as to human bladders. While, we would have liked to have increased the population size for this study even further, we were limited by the challenges associated with obtaining older rats as well as the time consuming aspects of the MPM analysis. Nonetheless, statistical significance was achieved relating wall type to structure of the extracellular matrix during loading.

The interconnection between layers is an interesting topic in the bladder wall as well as in other soft tissues, where it is also relatively unexplored. Recent work has, for example, explored these interconnections in the aortic wall in the context of delamination of wall layers (e.g. Tsamis et al. 2014). We believe this interconnection will have only a secondary effect on loading mechanisms during inflation, though this is certainly of interest for future studies. The current work does not assume any level of importance on the role of these fibers during bladder filling.

Necessarily, this study was carried out ex-vivo. There is currently no method for measuring collagen recruitment across the wall layers in vivo. In the future, studies could be performed to evaluate recruitment in fixed, inflated bladders to provide further evidence to support the current findings. However, such studies would be limited by the need to consider different bladders for each loading level, rather than a single sample across all loading levels, such as was done in the present work. Future work could also explore the structural mechanisms behind bladder viscoelasticity and anisotropy [57, 63].

2.5 Conclusions

This work has taken advantage of advances in bioimaging to directly assess collagen fibers and wall architecture during biaxial loading. It was directly shown for the first time, that the large extensibility of the bladder is determined largely by the length of the toe region of the loading curve. which arises from gradual flattening of the folds in the bladder

wall. These rugae provide a mechanism for low resistance flattening without any discernible recruitment of collagen fibers throughout the toe regime. We have shown that, in contrast to prior conjectures on the bladder wall, that a coordinated recruitment of collagen across the LP and DSM layers is essential for the large extensibility of the bladder wall. In extensible bladder walls, the collagen fibers in both the lamina propria and detrusor layers contribute to limiting distension at higher filling pressures. Furthermore, wall extensibility can be lost by premature recruitment of collagen in the DSM that cuts short the toe region and prevents extensive recruitment of collagen fibers in the LP. Loss of bladder extensibility (Type II walls) was more common in the aged population. Knowledge of the mechanisms responsible for bladder compliance is essential for providing targets for improved diagnostics, developing novel medical treatments of bladder dysfunction, and for understanding the biomechanical environment of the intramural cells that drive changes in the bladder wall in health and disease.

2.6 Acknowledgement

The authors gratefully acknowledge the NIH National Institute on Aging for funding through 1R56 AG050408-01(PI Birder) as well as the aged rats used in this study. The bladders used in this work were provided by the group of Dr. L. Birder. The authors also gratefully acknowledge Mr. Chih Yuan Chuang for performing the immunohistochemistry work to obtain histology images presented in Figure 5 of this chapter. The custom biaxial system and some preliminary data for the present work were previously described in the Proceedings of the 5th International Conference on Computational and Mathematical Biomedical Engineering - CMBE2017, [21].

2.7 Appendix to Chapter 2: Quantification of Collagen Recruitment Stretch Distribution in Young, Adult, Aged and Treated Bladders

2.7.1 Introduction

As noted in this chapter, bladders were found to gradually lose compliance during aging and there is no effective treatment to reverse this change. In this study, we proposed two treatments for the dysfunctional bladder. One is a mitochondrially targeted antioxidant, MitoTEMPO. The other is a purine nucleoside phosphorylase (PNPase inhibitor) 8-aminoguanine (8-AG). The effect of the two types of treatment was investigated by measuring the change the bladder wall mechanical properties and collagen recruitment distribution.

2.7.2 Method

2.7.2.1 Tissue Preparation

Twenty four Fischer rats were used in this study with three young, five aged, six adult, six aged treated by MitoTEMPO for 6 weeks, and five aged treated by 8-AG for 6 weeks. The unloaded meridional length (h_o) and diameter (w_o) were measured in the explanted bladder. The bladders were then cut open longitudinally and trimmed into square pieces with widths of 6mm $\pm$ 1mm such that the sides of the samples were aligned with the in situ longitudinal and circumferential directions, Figure 2a. To inhibit smooth muscle cell contraction, samples were immersed in Hanks Buffer Salt Solution (HBSS) containing, (in mM) NaCl 138, KCl 5, KH2PO4 0.3, NaHCO3 4, MgCl2 1, HEPES 10, glucose 5.6, with pH 7.4, 310 mOsm/l) without calcium and with added EDTA (0.5mM). The voltage calcium channel blocker nifedipine (5uM; Sigma) and the SERCA pump inhibitor, thapsigargin (1uM; Tocris Biosciences), which prevents the reloading of intracellular calcium stores, were also added.

2.7.2.2 Planar Biaxial Testing

Mechanical testing was performed using a custom biaxial system specifically designed for testing bladder tissue concurrent with imaging under a multiphoton microscope, Figure 2. This design enabled imaging of collagen fibers in intact specimens without staining or fixation. In the biaxial system, displacement can be independently controlled by four actuators (Aerotech, Inc., linear actuator ANT-25LA) and force measurements are performed using load cells on two of the actuators (Transducer techniques, nonrepeatibility 0.05% of R.O., capacity 5 lbs), Figure 2b. Tissue is mounted on the device using biorakes (World Precision Instruments, Inc.). The biaxial system includes a CCD camera and a 45 degree offset mirror to enable imaging of strain markers from beneath the mounted tissue, Figure 2d,e. This imaging system enables MPM imaging at prescribed biaxial strains.

Prior to testing, the unloaded thickness t_o of each sample was measured in 5 positions using a 0-150 mm digital caliper (Marathon watch company Ltd) and averaged. Fiducial strain markers (Basalt microspheres, 425-500 μm, Whitehouse Scientific) were attached to the abluminal side of each sample for strain calculation. During testing, the square sample was first loaded lumen side up on the biorakes, Figure 2b. Following [90], a tare-load was applied to the sample after which it was preconditioned, then unloaded, then loaded to the tare-load, then mechanically tested. Five consecutive equibiaxial loading cycles to a stretch of 1.8 were used for preconditioning with a tare-load of 0.02N. The post-precondition tare-loaded state is used as reference configuration. The lumen surface was imaged under MPM at stepwise increases in strains, Figure 2c. To avoid tissue damage while obtaining a large range of strain, loading was stopped after collagen fibers were visibly straightened (recruited) where it is defined as the maximum stretch. Hence, an individual maximum stretch was identified for each sample. After lumen side imaging, 5 equibiaxial loading cycles at a strain rate of $1\%s^{-1}$ to the maximum stretch were performed with the strain marker locations recorded by a CCD camera using the 45 degree mirror block beneath the sample (Figure 2d,e) and used to obtain the loading curves. The sample was then flipped and the imaging was repeated from the abluminal, once again until collagen recruitment was observed. The components of the Green-Lagrange strains were calculated from the fiducial marker locations using a finite

element interpolation method [70]. Components of the Cauchy stress tensor were calculated using load measurements with estimates of current cross sectional area obtained from the strain measurements under the approximation of isochoric motion.

2.7.2.3 Evaluation of fiber recruitment from multiphoton images

The collagen fiber recruitment fraction was quantified at multiple loading levels following a previously established method [20]. Briefly, collagen fibers are traced in the stack of 2D slices corresponding to the depth of the 3D reconstruction (Filament function in Imaris, Bitplane, Switzerland)[43]. The fiber arc length (c) was determined for each fiber tracing and the cord length (L) was defined as the length of the best linear fit line to the same segment. Fiber straightness was defined as the ratio of chord length to arc length L/c [43], Figure 4. A fiber was designated as recruited to load-bearing when its straightness reached 0.98 [43]. The robustness of the fiber straightness measurement in one stack of images is validated by checking the residual of average fiber straightness [20].

2.7.2.4 Models of Collagen Fiber Recruitment Distribution

The fiber recruitment distribution is represented with a triangular probability density function $\rho^i_{Rc}(\lambda^i_{Rc})$ [18, 8, 13, 78]; $\lambda^{i,q}_{Rc}$ relates to the the minimum ($q = min$), modal ($q = mode$) and maximum ($q = max$) recruitment stretches of the distribution, Figure**??**. More specifically:

$$\rho^i_R\left(\lambda^i_{Rc}\right) = \begin{cases} 0, & \lambda^i_{Rc} \leq \lambda^{i,min}_{Rc} \\ g_1(\lambda^i_{Rc}), & \lambda^{i,min}_{Rc} < \lambda^i_{Rc} \leq \lambda^{i,mode}_{Rc} \\ g_2(\lambda^i_{Rc}), & \lambda^{i,mode}_{Rc} < \lambda^i_{Rc} \leq \lambda^{i,max}_{Rc} \\ 0, & \lambda^{i,max}_{Rc} < \lambda^i_{Rc}, \end{cases} \tag{2.7}$$

We determined the three main parameters of the distribution ($\lambda_{Rc}^{i,min}$, $\lambda_{Rc}^{i,mode}$, $\lambda_{Rc}^{i,max}$) by fitting the cumulative triangular probability function using the tissue stretch and collagen fiber recruitment fraction data obtained using method described in 3.2.1.5, as shown in Figure 27. The estimation of collagen fiber recruitment stretch helped us to understand the loading mechanism of bladder and formulate hypothesis of collagen fiber layer dependent role in the model.

2.7.3 Results

2.7.3.1 Mechanical Response of Bladder Wall

Mechanical loading curves from biaxial testings are shown in Figure 15 and 16, with Cauchy stress as a function of stretch for averaged stress from the two loading directions. The aged bladder is less compliant than both the young and adult bladders. The MitoTEMPO treatment increased bladder compliance (shifting the loading curve to the right) though the compliance is still lower than young and adult. The bladder treated by 8-AG has a similar mechanical response compared with young and adult.

2.7.3.2 Collagen Fiber Recruitment Distribution

The collagen fiber recruitment distribution parameters ($\lambda_{Rc}^{i,min}$, $\lambda_{Rc}^{i,mode}$, $\lambda_{Rc}^{i,max}$) were compared across different types of bladder to evaluate the change in fiber structure and loading mechanism. Minimum Fiber Recruitment Stretch Compared with young and adult bladder, the minimum collagen fiber recruitment stretch in both layers is lower in the aged bladder. Compared with the aged bladder, the bladder treated by MitoTEMPO has higher minimum collagen fiber recruitment stretch in both layers. The 8-AG treatment also increased the minimum fiber recruitment stretch but only in DSM layer.

For young and adult bladders, the ratio ($\lambda_{Rc}^{dsm,min}/\lambda_{Rc}^{lp,min}$) is close to 1 and higher than the aged bladder. Both treatments shift this ratio toward 1 in the aged bladders, with 8-AG showing larger improvement than MitoTEMPO.

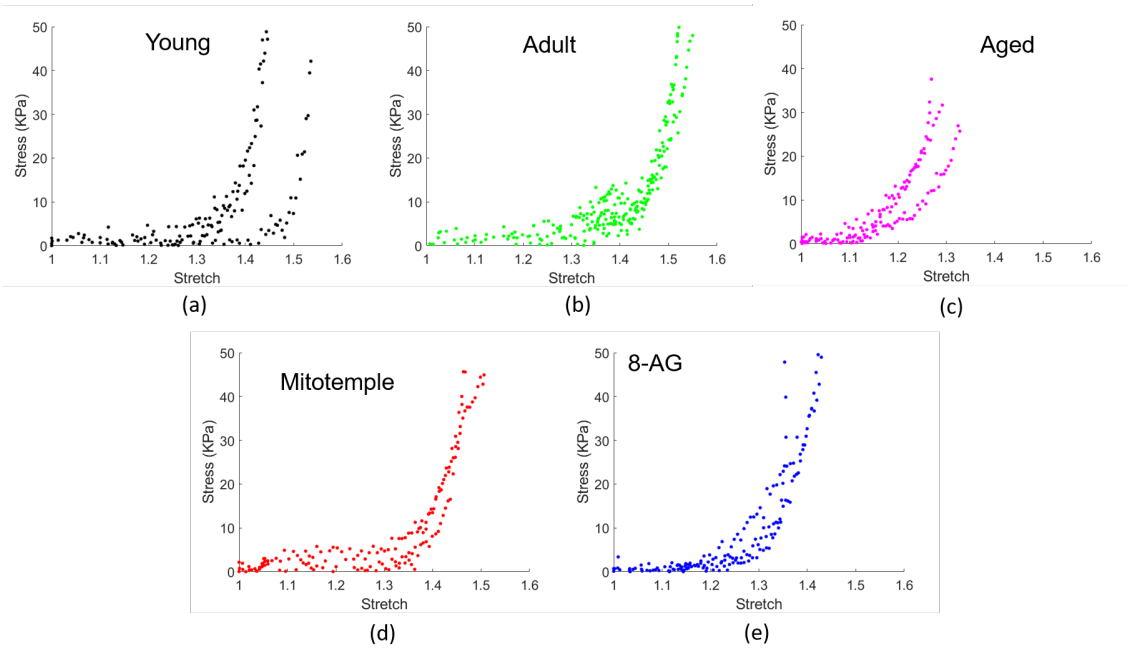

Figure 15: Individual mechanical loading curves (Stretch vs. Cauchy stress) obtained from planar biaxial testing for (a) young (b) adult (c) aged (d) aged treated by MitoTEMPO for 6 weeks and (e) aged treated by 8-AG for 6 weeks

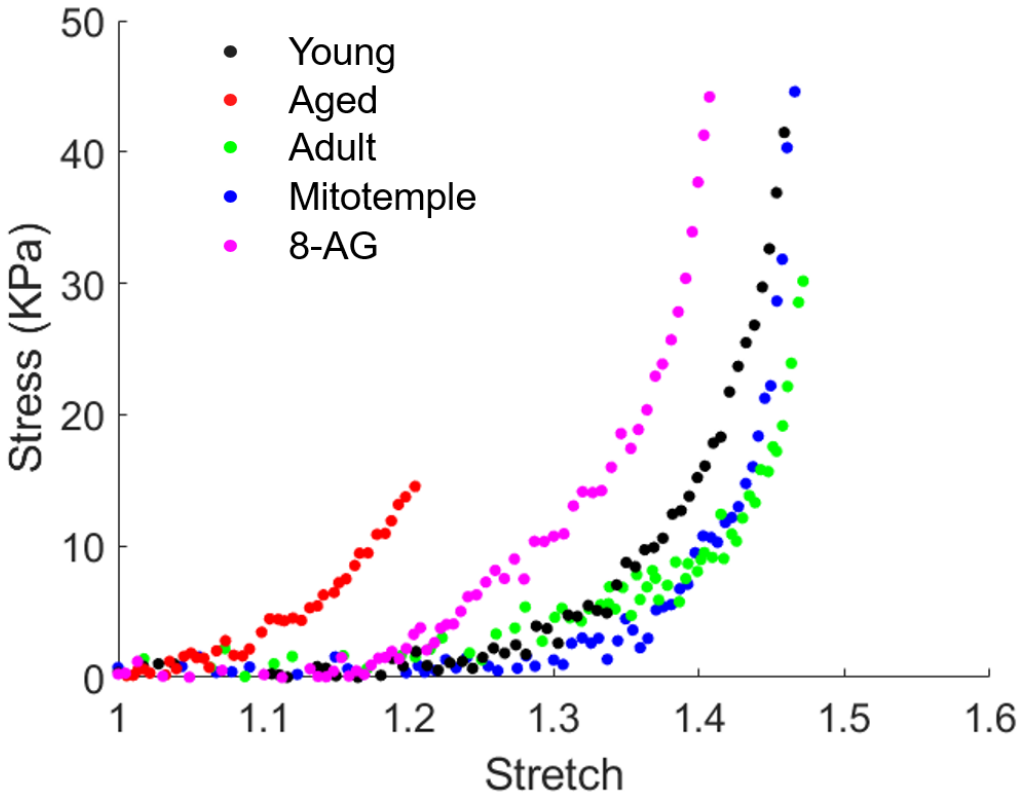

Figure 16: Averaged mechanical loading curves (Cauchy stress vs stretch) obtained from planar biaxial testing for young (black), adult (green), aged (red), aged treated by MitoTEMPO for 6 weeks (purple), and aged treated by 8-AG for 6 weeks (red)

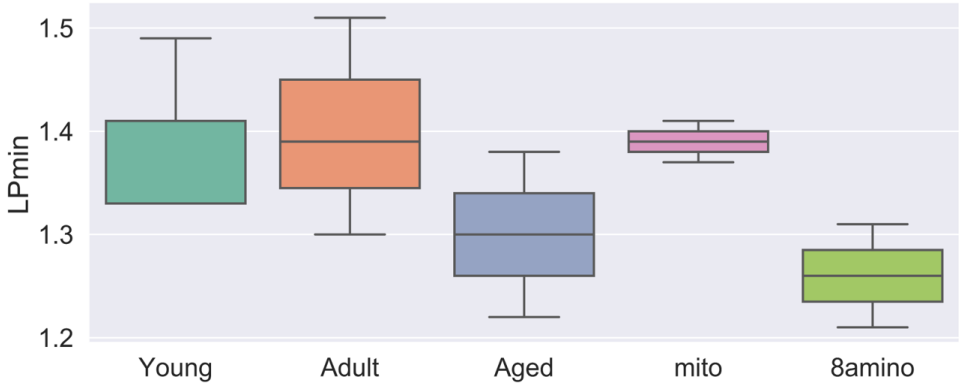

Figure 17: The minimum fiber recruitment stretch ($\lambda_{Rc}^{lp,min}$) in LP layer for different types of bladder.

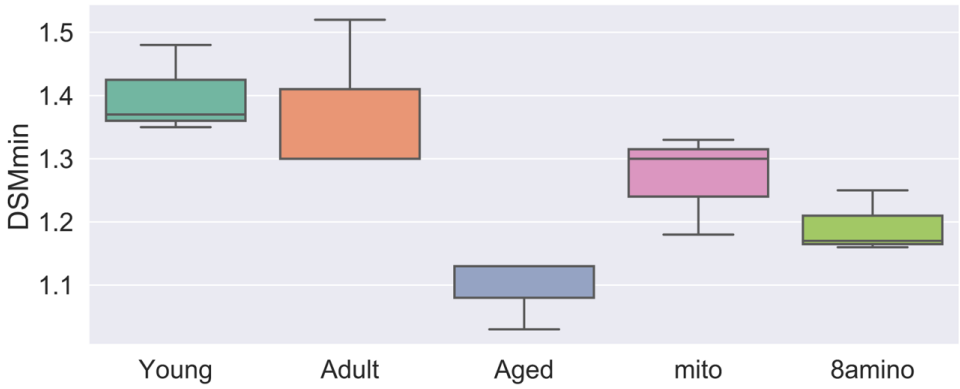

Figure 18: The minimum fiber recruitment stretch ($\lambda_{Rc}^{dsm,min}$) in DSM layer for different types of bladder.

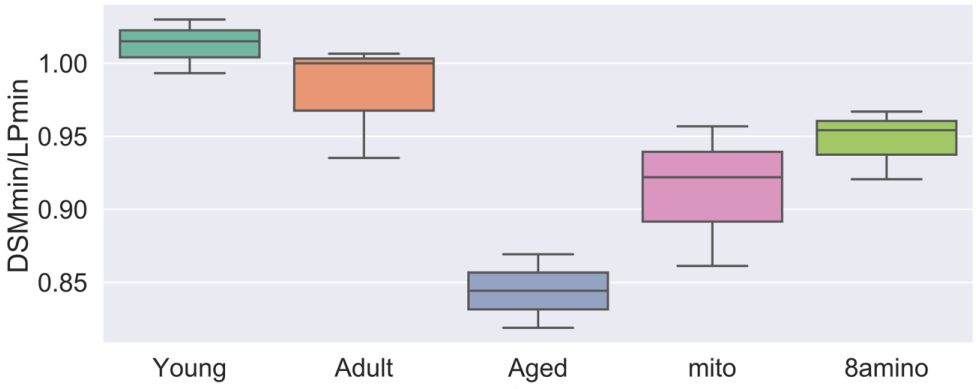

Figure 19: The ratio between the minimum fiber stretch recruitment in DSM and the minimum fiber recruitment stretch in LP ($\lambda_{Rc}^{dsm,min}/\lambda_{Rc}^{lp,min}$) for different types of bladder.

Width of Fiber Recruitment Distribution In the LP layer, the width of collagen recruitment distribution is not significantly different among the young, adult and aged bladder. However, we observed that both treatments widen the width of collagen recruitment distribution in the LP layer.

The width of DSM collagen recruitment distribution in the aged bladder is much higher than the young and adult bladders, Figure 20 and remains elevated in both treated bladders (MitoTEMPO and 8-AG).

2.7.4 Discussion

2.7.4.1 Initiation of Fiber Recruitment

As noted in the prior chapters, the bladder consists of elastin and collagen fibers. The highly undulated LP and folded muscle bundles in the DSM allow the bladder to extend without bearing much load at the early stage of filling. This unique mechanism gives the long toe regime in the loading curve. However, any fiber recruitment will steepen the loading curve and immediately end this toe regime. In this study, we use the minimum recruitment stretch parameter $\lambda_{Rc}^{i,min}$ to estimate the begin of collagen fiber recruitment. We found that the aged

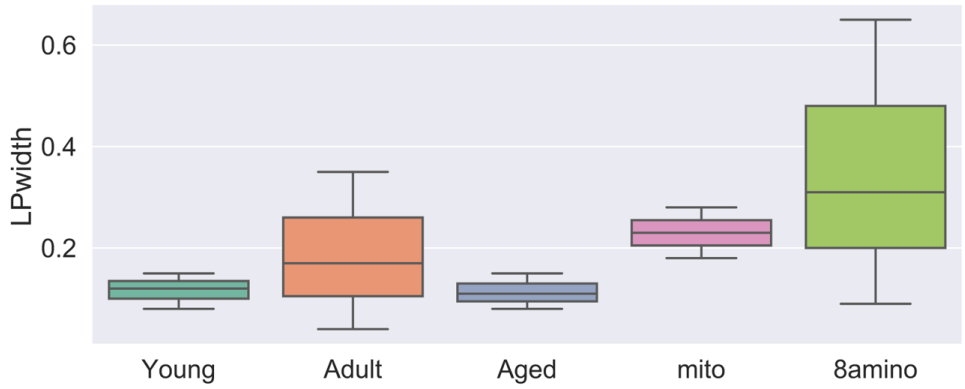

Figure 20: The width of collagen fiber recruitment stretch distribution ($\lambda_{Rc}^{lp,max} - \lambda_{Rc}^{lp,min}$) in LP layer for different types of bladder

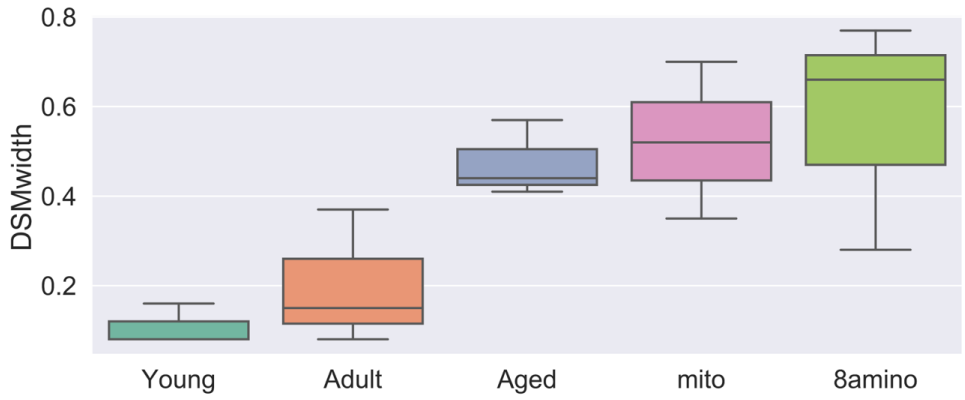

Figure 21: The width of collagen fiber recruitment stretch distribution ($\lambda_{Rc}^{dsm,max} - \lambda_{Rc}^{dsm,min}$) in DSM layer for different types of bladder

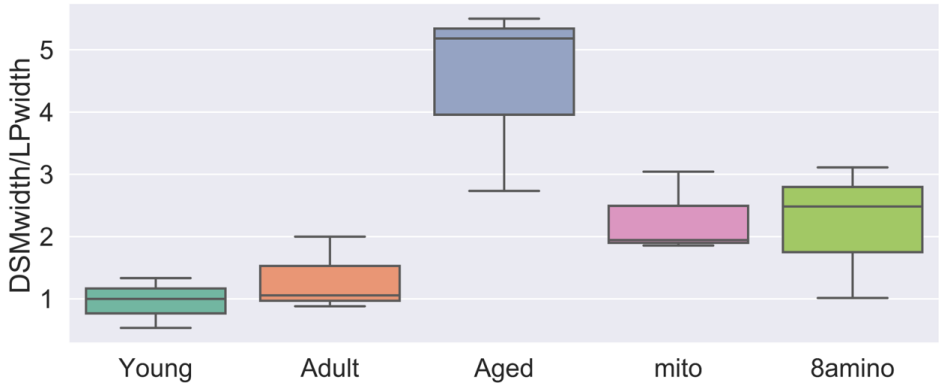

Figure 22: The ratio between DSM fiber recruitment stretch distribution width and LP fiber recruitment stretch distribution width, $(\lambda_{Rc}^{dsm,max} - \lambda_{Rc}^{dsm,min})/(\lambda_{Rc}^{lp,max} - \lambda_{Rc}^{lp,min})$, for different types of bladder

bladder has a premature collagen fiber recruitment in both DSM and LP layer and this is why it has a much shorter toe regime compared with young and adult. The MitoTEMPO treatment seems to be able to increase the minimum recruitment stretch of both layers in the aged bladder. The 8-AG treatment can also delay the premature recruitment of fibers, though mainly happens in the DSM layer.

2.7.4.2 Coordination of Fiber Recruitment

The coordination of fiber recruitment between the two layers was assessed in two ways. The first was to assess the coordination of the onset of fiber recruitment. The other was to assess the consistency of the width of collagen fiber distribution, namely if it takes the same stretch to recruit the majority of fibers in both layers. As shown in Figure 19, for both the young and adult bladder the ratio between the minimum fiber stretch recruitment in DSM versus LP is close to 1. Moreover, for both young and adults bladders, the fiber recruitment distribution width between DSM and LP in young and adult bladders is also close 1. This indicates that their collagen fibers from both layers are almost well coordinated. However,

Table 4: The collagen recruitment stretch distribution parameters for all samples

	$\lambda_{Rc}^{dsm,min}$	$\lambda_{Rc}^{dsm,mod}$	$\lambda_{Rc}^{dsm,max}$	$\lambda_{Rc}^{lp,min}$	$\lambda_{Rc}^{lp,mod}$	$\lambda_{Rc}^{lp,max}$
mito01	1.21	1.44	2.07	1.28	1.58	1.67
mito02	1.18	1.33	1.88	1.37	1.59	1.60
mito03	1.33	1.37	1.68	1.39	1.44	1.57
mito04	1.06	1.65	2.01	1.17	1.34	1.53
mito05	1.31	1.43	1.82	1.41	1.42	1.69
mito06	0.98	1.33	1.37	1.25	1.21	1.93
8amino01	1.16	1.42	1.93	1.26	1.44	1.57
8amino02	1.17	1.63	1.83	1.05	1.55	1.64
8amino03	1.25	1.26	2.05	1.34	1.37	1.77
8amino04	1.25	1.35	1.53	1.31	1.32	1.40
8amino05	1.04	1.13	1.25	1.03	1.04	1.28
Young01	1.35	1.39	1.51	1.33	1.38	1.45
Young02	1.37	1.43	1.45	1.33	1.39	1.48
Young03	1.48	1.52	1.56	1.49	1.52	1.57
Aged02	1.13	1.31	1.72	1.38	1.42	1.49
Aged03	1.13	1.22	1.54	1.30	1.35	1.45
Aged04	1.03	1.43	1.47	1.22	1.28	1.33
Aged05	1.17	1.29	1.38	1.28	1.45	1.59
Aged06	1.12	1.25	1.96	1.36	1.43	1.61
Aged07	1.15	1.53	1.68	1.10	1.46	1.56
Adult01	1.16	1.37	1.38	1.31	1.33	1.51
Adult02	1.52	1.54	1.65	1.51	1.54	1.55
Adult03	1.32	1.56	1.67	1.32	1.49	1.65
Adult04	1.31	1.42	1.45	1.39	1.43	1.56

the aged bladder has less coordination between the two layers displaying both premature fiber recruitment and a wider recruitment distribution developed in the DSM layer versus the LP layer. Both treatments, MitoTEMPO and 8-AG, tended to recover the coordinated initiation of recruitment between the layers.

3.0 A Novel Hybrid Constrained Mixture Model for the Bladder

3.1 Introduction

Lower urinary tract symptoms (LUTs) are a collection of symptoms that include increase of urination frequency, urgency, and incontinence, and can be categorized as being related to urine storage or voiding. LUTS can cause significant morbidity and dramatically lower quality of life for those affected [34] [24]. They are usually triggered by one or more bladder disorders such as bladder outlet obstruction, detrusor disorders, and non-compliant bladder. Diagnosis of patients presenting with LUTs heavily rely on an invasive, time consuming and costly procedure called urodynamics. Urodynamic studies replicate the filling and voiding functions and allow the quantification of vesical and abdominal pressures, and measures the flow both to and from the bladder through the use of urethral and rectal catheters. While the urodynamic studies provide a method of quantifying the mechanical functionality of the bladder, these invasive tests do not always reveal underlying disorders responsible for patient symptoms, resulting in costly follow-up procedures, or inefficient treatment. To increase diagnostic success or replace invasive procedures with non-invasive alternatives, a better understanding of the relationship between underlying disorders, the mechanics of bladder function and LUTS is needed. In this work, mathematical models have been developed and employed in order to understand the underlying mechanism of bladder function.

The mechanical function of the bladder is usually assumed to be attributed to the following properties: elasticity, contractility, nervous control, and urethra resistance relation (URR). Griffiths [39] created the first bladder micturition model including the contractility, nervous control, and URR. However, elasticity was neglected in this model as the elastic passive stress was assumed to be much smaller than the active stress. After that, multiple micturition models were developed with the focus mainly on the interaction between muscle and urethra [28, 66]. Even though the micturition models improved the understanding of the bladder voiding function, they neglected or oversimplified the elastic contributors and did not provide information into the specific structural mechanism driving bladder function. To

bridge this gap, constitutive models [23] [12] [85] of the bladder with the focus on the passive bladder elasticity were developed based on Fung's exponential model [31]. While these models provide high-quality fitting to mechanical testing data, they are mainly phenomenological and therefore can not explain the correspondence between individual model components and bladder function. In 2010, Wognum et al. introduced the first ensemble fiber bladder model including the fiber orientation and recruitment [89]. Following this idea, [59] created a constrained mixture model using separate strain energy functions for the ground matrix and collagen fibers. Even though these recent efforts captured the properties of some bladder components, they were not used to understand the bladder micturition function.

In the current study, we developed a novel hybrid model that couples a constrained mixture model with a micturition framework. The model includes the bladder elasticity, contractility, nervous control, and urethra resistance relation (URR) and is informed by both in-vivo (planar biaxial testing) and ex-vivo (cystometry) experiments. Collagen fiber distribution of individual layers were directly measured from multiphoton images. The collagen fiber stiffness was calibrated by planar biaxial testing data and muscle stiffness was calibrated by bladder cystometry. This model was then applied to a an idealized case of spherical inflation of the bladder using an isotropic representation for the wall components. Using this structurally motivated model, we were able to explain for the first time the role of bladder wall components in bladder mechanical function during filling and.

3.2 Methods

We utilise an integrative *in vivo in-vitro in-silico* modelling approach (see Figure 23). An *in silico* model is developed that simulates the mechanics of the micturition cycle in healthy bladder. Where possible, model parameters are informed from *in vivo* pressure-flow experiments and *in vitro* planar biaxial testing coupled with multi-photon microscopy of the collagen fibers.

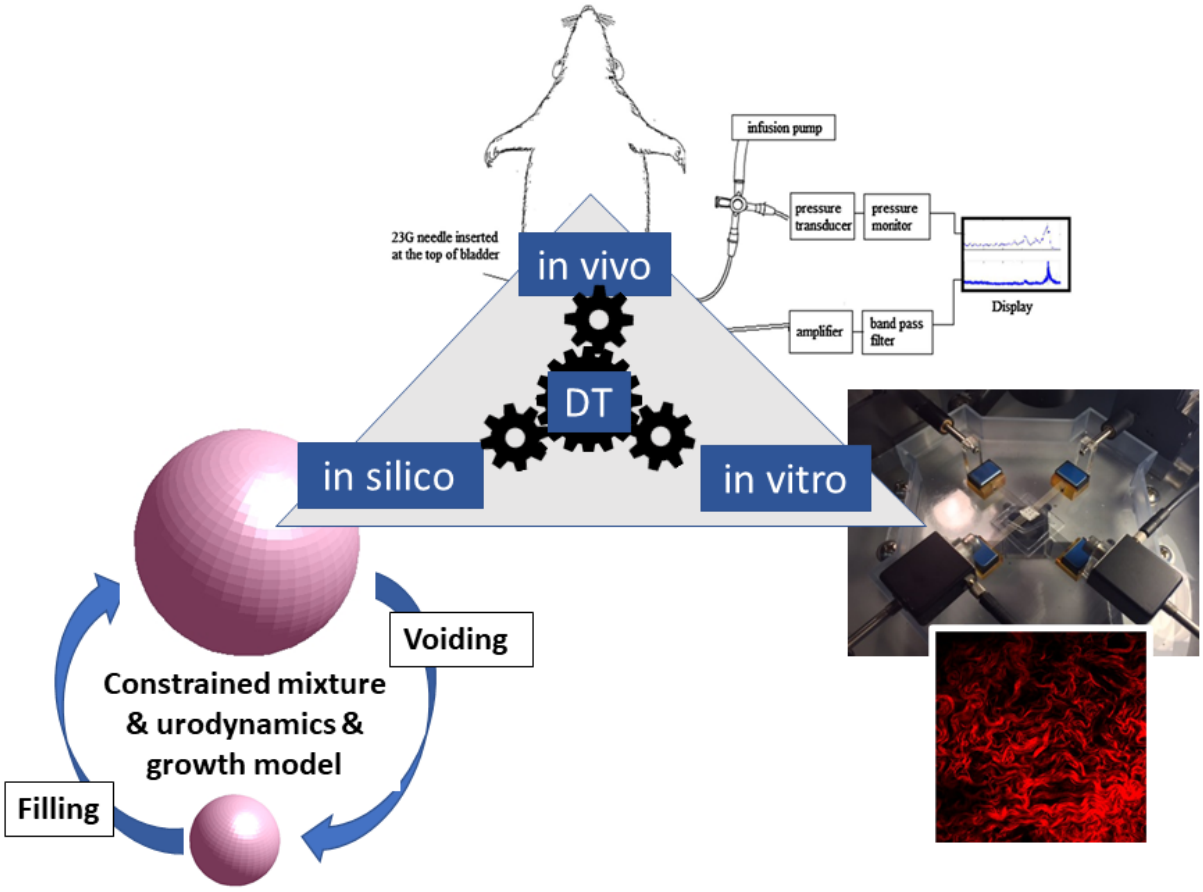

Figure 23: An integrative *in vivo in-vitro in-silico* modelling approach. Figure provided by P. Watton, with permission.

3.2.1 Experimental Studies

3.2.1.1 In vivo Measurements: Pressure-flow Study

Twelve young (6-month old, male) Sprague Dawley rats, weighing 370±8.9g, were used in the cystometry (pressure-flow) studies[76] with Institutional Animal Care and Use Committee guidelines being observed. Under isoflurane anaesthesia, a PE-50 polyethylene catheter (Clay-Adams, Parsippany, NJ) was inserted through the bladder dome and a purse-string suture was placed tightly around the catheter. The implanted catheter was exteriorized through the abdominal wall, and the wound was closed with 4-0 silk sutures. After the surgery, the rats were placed in restraining cages (W 80 mm × L 300 mm × H 150 mm, Yamanaka Chemical Ind., Ltd, Osaka, Japan) and allowed to recover from isoflurane anaesthesia for 1–2 h before starting cystometry. After recovery, a three-way stopcock was used to connect the intravesical catheter to a pressure transducer (Transbridge 4M, World Precision Instruments, Sarasota, FL, USA) for recording intravesical bladder pressure and to a syringe pump (*company*) for infusing saline at a fixed flowrate. Saline was initially infused at 0.1 ml/min; subsequently, the infusion rate was adjusted to 0.04–0.3 ml/min to obtain an intercontraction interval around 10-15 min [60]. The recorded data were used to construct the pressure/flow curves (Figure 24), from which the following parameters were evaluated: (i) maximum voiding pressure $P_{max}^{voiding}$ (the peak pressure minus the basal pressure during each voiding cycle); (ii) maximum passive filling pressure $P_{max}^{passive}$ (the pressure immediately after the reflex contraction minus the basal pressure; the basal pressure is the the passive pressure in the empty bladder and measured from the lowest pressure during cystometry). The maximum active voiding pressure (P_{max}^{active}) is defined as the difference between maximum voiding pressure and maximum passive filling pressure, i.e. $P_{max}^{active} = P_{max}^{voiding} - P_{max}^{passive}$. The voiding duration ($\Delta t_{void}$) was also recorded and voided urine was collected using a plastic cup placed underneath the restraining cage and measured to determine the voided volume (ΔV_{void}), and post-void residual volume (V_{PV}) was collected and measured by draining the post-void bladder using the bladder catheter with gravity [76]. Bladder capacity (V_F) was calculated as the sum of voided and residual volumes.

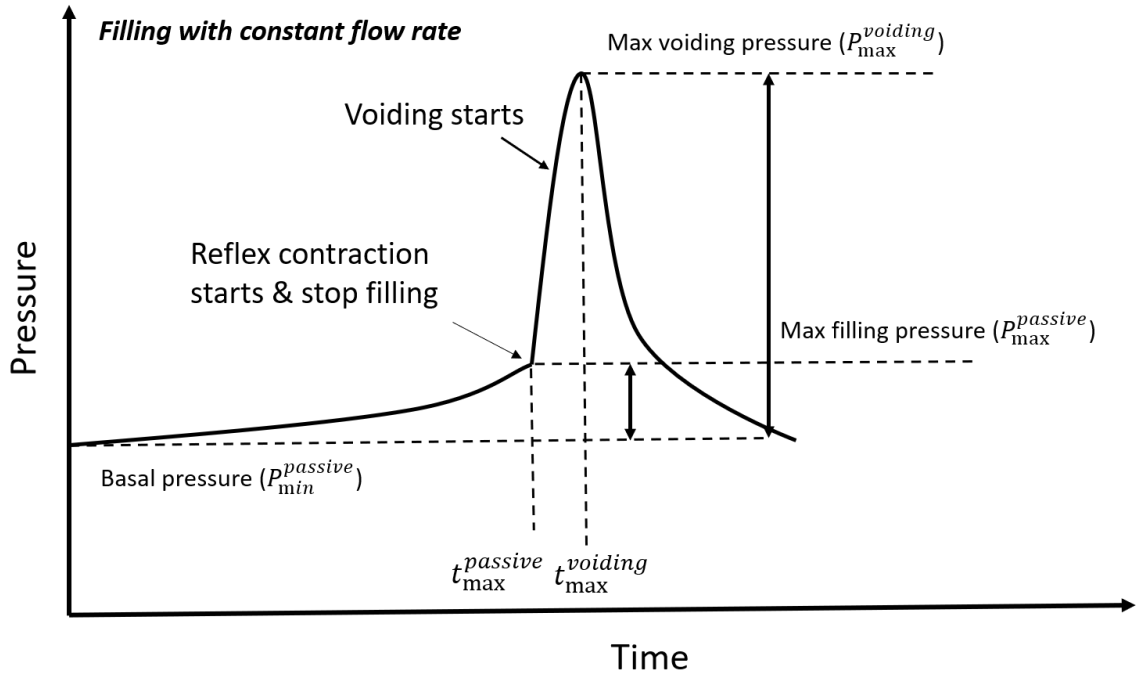

Figure 24: Schematic representation of the pressure flow curve during the cystometry study.

3.2.1.2 In vitro Measurements: Planar Biaxial Testing

As described below, mechanical testing was performed on square samples from four young rat bladders using a custom biaxial system specifically designed for testing bladder tissue concurrent with imaging under a multiphoton microscope (MPM) [20]. This approach enables imaging of the reorganization and recruitment of collagen fibers during loading within fresh, intact specimens without staining or fixation. In particular, after the bladder was harvested, the ex-vivo unloaded width (W_0), height (Y_0) and thickness (H_o) of the bladder were measured and the bladder volume was approximated as an ellipsoid ($V_0 = \pi {W_0}^2 Y_0/6$), Table 8.

To inhibit smooth muscle cell contraction [20], the dissected intact bladders were immersed in Hank's buffer salt solution (HBSS) containing, (in mM) NaCl 138, KCl 5, KH_2PO_4 0.3, $NaHCO_3$ 4, $MgCl_2$ 1, HEPES 10, glucose 5.6, with pH 7.4, 310 $mOsm/l$) without calcium and with added EDTA (0.5 mM). The voltage calcium channel blocker nifedipine ($5\mu M$; Sigma) and the SERCA pump inhibitor, thapsigargin ($1\mu M$; Tocris Biosciences), which prevents the reloading of intracellular calcium stores, were also added. The bladders were then cut open longitudinally and trimmed into square pieces with widths of 6 ± 1 mm such that the sides of the samples were aligned with the in situ longitudinal and circumferential directions. Prior to testing, the unloaded thickness H_0 of the samples were measured at 5 locations using a digital caliper (0–150 mm range, Marathon Watch Company Ltd) and averaged.

Fiducial strain markers (Basalt microspheres, 425–500 μm, Whitehouse Scientific) were attached to the abluminal side of each sample for strain calculations. The square samples were then mounted lumen side up in the biaxial device using biorakes (World Precision Instruments, Inc.). During testing, displacement was controlled by four actuators (Aerotech, Inc., linear actuator ANT-25LA) and force measurements were taken using load cells on two of the actuators (Transducer Techniques, nonrepeatability 0.05% of rate output, capacity 5 lbs). A CCD camera and a 45^o offset mirror enabled imaging displacement of fiducial markers from beneath the mounted tissue, [20].

The testing protocol follows [90]. Briefly, five consecutive equibiaxial loading cycles

to a prescribed sample stretch of 1.8 were performed for preconditioning, followed by five consecutive main loading cycles. As the penetration depth for MPM imaging for bladder tissue is less than the bladder thickness, the sample was imaged from both lumen and abluminal sides to assess collagen recruitment as a function of applied stretch. To avoid tissue damage at large strains, loading was stopped when collagen fibers were visibly straightened under MPM.

Load taring was applied before the preconditioning and main loading cycles following the methods described [90]. The purpose of load taring is to avoid the immeasurable low force due to the extreme softness of bladder at small stretch and create a common reference configuration during mechanical testing for all samples. Briefly, a force value of $F_1 = 0.02N$ was subtracted from the load cell values when calculating the Cauchy stress. The post-precondition tare-loaded state κ_1 is used as the reference configuration. The stretch relative to κ_1, denoted as $\bar{\lambda}^{(1)}(t)$, was calculated from the displacements of the fiducial markers using a finite element interpolation method [70]. Namely, we denote the specimen width and thickness in κ_1 as L_1 and $\bar{H}_1$, respectively. Then, the width of L_1 is used as a reference length when calculating specimen stretch $\bar{\lambda}^{(1)} = L/L_1$. Here, the overbar is used as needed to distinguish quantities in the planar biaxial testing from those in spherical inflation. We denote the tared force value (with F_1 subtracted) as F',

$$F' = F - F_1 \tag{3.1}$$

The corresponding stress $\bar{\sigma}'$ is

$$\bar{\sigma}' = F'/(L\bar{H}) = (F - F_1)/(L\bar{H}). \tag{3.2}$$

The experimental data can then be presented as a function of $\bar{\lambda}^{(1)}$. Namely, $\bar{\sigma}' = \bar{\sigma}'(\bar{\lambda}^{(1)})$.

3.2.1.3 Kinematics for the Cystometry Data

The modeling studies in this chapter idealize the bladder as a spherical membrane. In this context, we define an equivalent bladder radius for each of the configurations of interest which have measured volumes, Figure 25. Namely, R is calculated as the radius of a sphere with the equivalent volume. In particular, the bladder radius for the unloaded configuration, κ_0 is obtained from the explanted bladder volume V_0, the post void radius R_{PV} is calculated from measured voided volume V_{PV}, and R_F is calculated from the measured filled volume $V_F = V_{PF} + \Delta V_{void}$, Table 5. The stretch associated with inflation of a spherical membrane at an arbitrary intermediate state can then be calculated relative to κ_0,

$$\lambda^{(0)}(s) = \frac{R(s)}{R_0}. \tag{3.3}$$

The corresponding thicknesses follow directly for this isochoric motion, given the measured thickness in κ_0. Definitions of various quantities relevant to the spherical models are summarized in Table 5

3.2.1.4 Extending the Bi-axial Data to the Unloaded State

In order to make use of the biaxial testing data in the studies of bladder filling/voiding, it is necessary to extend the data from the bi-axial testing to the unloaded state, κ_0. As noted above, the mechanical loading curves were obtained using κ_1 as the reference state and data was obtained for stretches of $\bar{\lambda}^{(1)} \geq 1$. However, the ex-vivo tared load would correspond to a loaded (deformed) bladder in vivo. In order to model the entire filling voiding cycle, we need to obtain the complete loading curve

$$\bar{\sigma}' = \bar{\sigma}'(\bar{\lambda}^{(1)}) \qquad \bar{\lambda}^{(1)}(s) \geq 1 \quad \longrightarrow \quad \bar{\sigma} = \bar{\sigma}(\bar{\lambda}^{(0)}) \qquad \bar{\lambda}^{(0)}(s) \geq 1. \tag{3.4}$$

We first note that it follows from Eq. 3.5,

$$\bar{\sigma} = \bar{\sigma}' + \bar{\lambda}^{(1)}\sigma_1 \quad \text{where} \quad \bar{\sigma}_1 = F_1/(L_1\bar{H}_1) \tag{3.5}$$

Furthermore,

$$\bar{\lambda}^{(0)}(s) = \frac{L(s)}{L_0} = \frac{L(s)}{L_1}\frac{L_1}{L_0} = \bar{\lambda}^{(1)}(s)\bar{\lambda}_1^{(0)} \tag{3.6}$$

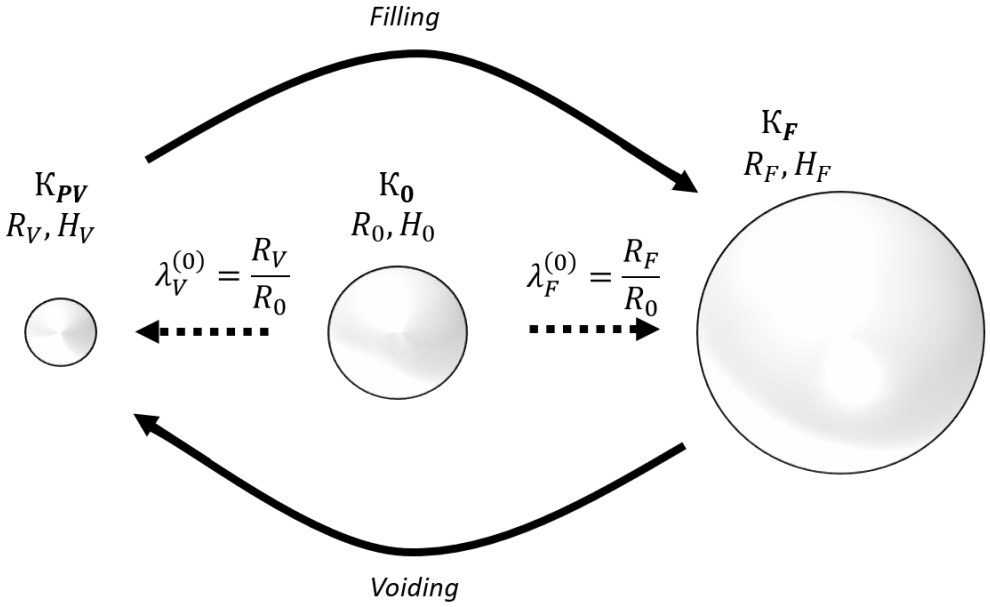

Figure 25: Schematic of different reference configurations relevant to modeling cystometry. Here, κ_0 represents the unloaded state of the bladder, κ_F the filled state right before the voiding and κ_{PV} the state where voiding is just completed (post voiding). The symbols R and H represent the radius and thickness at the corresponding state labeled by the subscript. Here, the radii are calculated for a sphere with the equivalent volume measured in cystometry. Further, λ represents the bladder stretch at the configuration labeled by the subscript with stretch relative to the reference configuration labeled by the superscript, Table 5. Namely, λ represents the bladder stretch at the state labeled by the subscription with reference to the state labeled by the superscript.

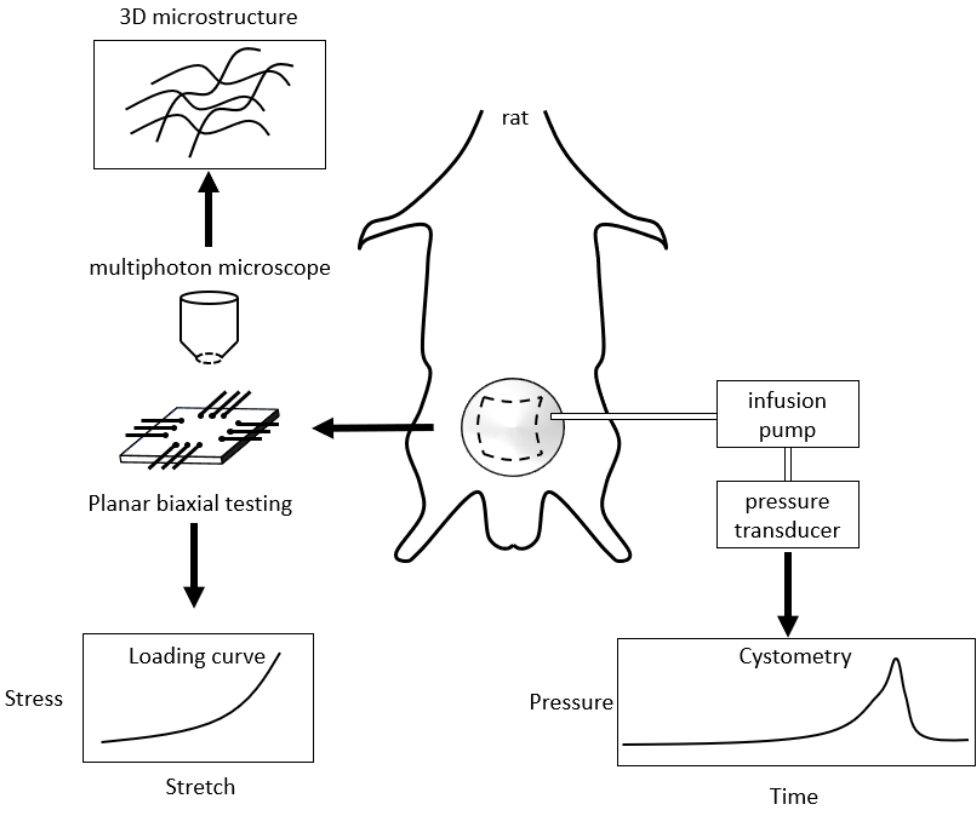

Figure 26: Schematic of overview experimental setup

Table 5: Summary of definitions of variables for studies of spherical bladder models.

	Pressures
$\mathrm{P}_{min}^{passive}$	(Basal pressure) Passive pressure in the empty bladder, measured from lowest pressure in cystometry
$\mathrm{P}_{max}^{passive}$	Pressure immediately after reflex contraction minus $P_{min}^{passive}$
$P_{max}^{voiding}$	Peak pressure minus $P_{min}^{passive}$
	Bladder Volumes
V_0	Volume of explanted empty bladder, (estimated from W_0, Y_0)
V_{PV}	Bladder post void volume, measured in cystometry
ΔV_{void}	Bladder voided volume, measured in cystometry
V_F	Bladder filled volume ($V_F = V_{PV} + \Delta V_{void}$)
	Equivalent Radii from $4/3\ \pi R^3 =$ volume
R_0	From explanted bladder volume in κ_0
R_{PV}	From bladder post void volume, V_{PV}
R_F	From bladder filled volume, V_F
	Stretch values
$\lambda_{PV}^{(0)}$	$\lambda_{PV}^{(0)} = R_{PV}/R_0$
$\lambda_F^{(0)}$	$\lambda_F^{(0)} = R_F/R_0$
$\lambda_1^{(0)}$	$\lambda_1^{(0)} = \lambda_F^{(0)}/\lambda_F^{(1)}$
	Wall Thickness
H_0	Measured in ex-vivo unloaded bladder κ_0
H_{PV}	Calculated assuming isochoric motion: $H_{PV} = H_0/{\lambda_{PV}^{(0)}}^2$
H_F	Calculated assuming isochoric motion: $H_F = H_0/{\lambda_F^{(0)}}^2$

where $\bar{\lambda}^{(0)}(s)$ denotes the stretch at an arbitrary intermediate state $\kappa(s)$ relative to the unloaded bladder. However, we do not know the value of $\bar{\lambda}_1^{(0)}$, which is needed to extend the biaxial data to the unloaded state of the bladder.

To determine $\bar{\lambda}_1^{(0)}$, we consider Eq. 3.6 at the filled state through $\bar{\lambda}_F^{(0)} = \bar{\lambda}_F^{(1)}\bar{\lambda}_1^{(0)}$, or

$$\bar{\lambda}_1^{(0)} = \bar{\lambda}_F^{(0)}/\bar{\lambda}_F^{(1)}. \tag{3.7}$$

If we determine $\bar{\lambda}_F^{(0)}$ and $\bar{\lambda}_F^{(1)}$, we will have determined $\overset{(0)}{1}$. We first recall that the analytical stress solution of equi-biaixal stretch and spherical inflation have the same functional form for the exponential model (see Appendix 3.8). We define the $\bar{\sigma}_F$ equal to the stress in the filled bladder σ_F. As the functional forms are the same, the stretch corresponding to the filled stress state in the specimen, $\bar{\lambda}_F^{(0)}$, will be the same at that in the filled spherical bladder,

$$\bar{\lambda}_F^{(0)} = \lambda_F^{(0)} = R_F/R_0. \tag{3.8}$$

Hence, we have a means to calculate $\bar{\lambda}_F^{(0)}$ in Eq. 3.7. We now note that the stretch $\bar{\lambda}_F^{(1)}$ in Eq. 3.7 can be obtained from the experimental data for $\bar{\sigma}'(\bar{\lambda}^{(1)})$ as the stretch corresponding to the $\bar{\sigma}'_F$. From Eq. 3.5

$$\bar{\sigma}'_F(\bar{\lambda}_F^{(1)}) = \bar{\sigma}_F - \sigma_1\bar{\lambda}_F^{(1)} \tag{3.9}$$

where

$$\bar{\sigma}_F = \sigma_F \qquad \sigma_1 = F_1/(L_1\bar{H}_1). \tag{3.10}$$

Hence, we can solve for $\bar{\lambda}_F^{(1)}$ using Eq. 3.9 and therefore, can determine $\bar{\lambda}_1^{(0)}$.

The experimental data is in the form $\bar{\sigma}' = \bar{\sigma}'(\bar{\lambda^{(1)}})$ where $\bar{\lambda}^{(1)} \geq 1$. It can now be mapped to $\bar{\sigma} = \bar{\sigma}(\bar{\lambda^{(0)}})$ with $\bar{\lambda}^{(0)} \geq \bar{\lambda}_1$ using Eqs. 3.5 and 3.6. We furthermore extend the definition of $\bar{\sigma}(\bar{\lambda}^{(0)})$ down to $\bar{\lambda}^{(0)} = 1$ using a linear fit between $(\bar{\lambda}^{(0)}, \bar{\sigma}) = (1, 0)$ and $(\bar{\lambda}_1, \bar{\sigma}_1)$.

3.2.1.5 Evaluation of Fiber Recruitment from Multiphoton Images

The collagen fiber recruitment fraction was quantified at multiple loading levels following a previously established method [20]. Briefly, collagen fibers are traced in the stack of 2D slices corresponding to the depth of the 3D reconstruction (Filament function in Imaris, Bitplane, Switzerland)[43]. The fiber arc length (c) was determined for each fiber tracing

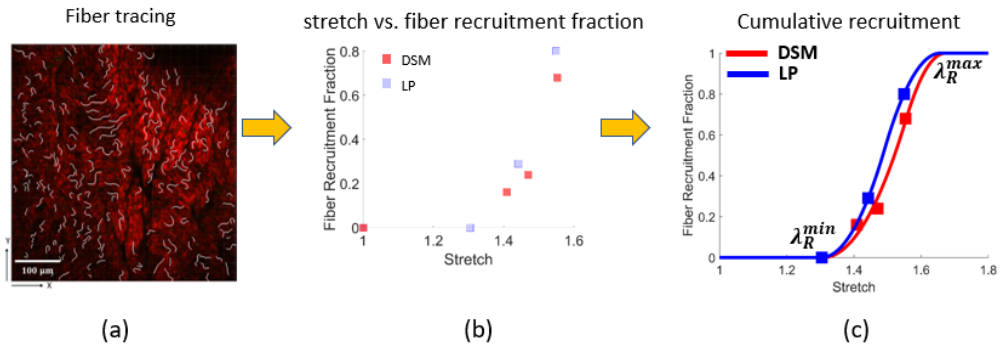

Figure 27: Procedure for fitting the fiber recruitment distribution function shown for representative data set: (a) fiber tracing overlaid on multiphoton image (red is collagen fiber) (b) Fiber recruitment fraction versus stretch (c) Cumulative density function as fit to the fiber recruitment fraction. This curve is used to obtain the three layer specific (i) parameters of the collagen recruitment (Rc) stretch distribution: $\lambda_{Rc}^{i,min}$, $\lambda_{Rc}^{i,mode}$ and $\lambda_{Rc}^{i,max}$

and the cord length (L) was defined as the length of the best linear fit line to the same segment. Fiber straightness was defined as the ratio of chord length to arc length L/c [43], Figure4. A fiber was designated as recruited to load-bearing when its straightness reached 0.98 [43]. The robustness of the fiber straightness measurement in one stack of images is validated by checking the residual of average fiber straightness [20].

3.2.2 Constitutive Modeling for the Bladder Wall Mechanics

The bladder wall was modeled as an incompressible, nonlinear elastic material. We assume an additive decomposition of the stresses due to the passive component (elastin and collagen) and and active components (smooth muscle cells)

$$\underline{\sigma} = \underline{\sigma}_{L,e} + \underline{\sigma}_{L,c} + \underline{\sigma}_a. \tag{3.11}$$

where $\underline{\sigma}_{L,e}$ and $\underline{\sigma}_{L,c}$ are the Cauchy stress for elastin and collagen fibers, respectively, and $\underline{\sigma}_a$ is the active stress from smooth muscle contraction.

3.2.2.1 Kinematics

The deformation gradient tensor is denoted as $\underline{F}$ and the right Cauchy-Green tensor as $\underline{C} = \underline{F}^T\underline{F}$. The tensor invariants for $\underline{C}$ are $I_1 = tr(\underline{C})$, $I_2 = (tr(\underline{C})^2 - tr(\underline{C}^2))/2$ and $I_3 = \det(\underline{C}) = 1$. The direction of the collagen fibers is denoted by the unit vector $\underline{a}_c^i$ where i ranges over the number of fiber orientations at each point within the tissue. The stretch in the collagen fibre direction, denoted by λ_{4c}^i, can then be written with respect to I_{4c}^i through,

$$\left(\lambda_{4c}^i\right)^2 = I_{4c}^i = \underline{C} : \underline{a}_c^i \otimes \underline{a}_c^i, \tag{3.12}$$

where I_{4c}^i is a pseudo-invariant of $\underline{C}$ and $\underline{a}_c^i \otimes \underline{a}_c^i$.

Similarly, denoting the SMC direction by the unit vector $\underline{a}_m$, the stretch λ_{4m} in the SMC direction is

$$\left(\lambda_{4m}^i\right)^2 = I_{4m} = \underline{C} : \underline{a}_m \otimes \underline{a}_m \tag{3.13}$$

3.2.2.2 Strain-energy Functions

The passive response of each layer L receives contributions from elastin and collagen fibers (anisotropic components). Hence

$$\Psi_L = \Psi_{L,e}(I_1) + \sum_i \Psi_{L,c}^i(I_{4c}^i) \tag{3.14}$$

Here, we consider three layers, $L = LP$ denotes lamina propria and $L = DSM$ denotes the destrusor muscle layer, and $L = ADV$ denotes the adventitia layer.

3.2.2.3 Elastinous Constitutents

The elastin components in each layer are modeled as isotropic, and in particular as a neo-Hookean material [88]:

$$\Psi_{L,e} = K_e \left(I_1 - 3\right), \tag{3.15}$$

with K_e being material constants. The corresponding Cauchy stress tensor $\sigma_{L,e}$ can be calculated as :

$$\underline{\sigma_{L,e}} = -p\underline{I} + 2K_e\underline{B} \tag{3.16}$$

where p is the Lagrange multiplier and $\underline{B}$ is the right Cauchy-Green deformation tensor.

3.2.2.4 Collagenous Constituents

The constitutive model for the collagen accounts for both the collagen fiber orientation distribution as well as the experimental observation that collagen fibers have a a distribution of waviness in the unloaded configuration and thus have a distribution of recruitment stretches ([43]). The strain energy function involves integrating the strain energy for a fiber ($\tilde{\Psi}^i_{L,c}$) over the distribution of recruitment stretches (ρ^i_R),

$$\Psi_{L,c}(I^i_4) = m_{L,c} \cdot \sum_i \int_1^{\sqrt{I^i_4}} \tilde{\Psi}^i_{L,c}\left(\lambda^i_c\right) \rho^i_{Rc}\left(\lambda^i_{Rc}\right) d\lambda^i_{Rc}. \tag{3.17}$$

where $\lambda^i_{Rc} = \sqrt{I^i_{Rc}}$ denotes the recruitment stretch of the collagen fiber and $m_{L,c}$ is the (dimensionless) normalized mass density of collagen fibers that can adapt to simulate collagen growth/atrophy[87]. We model each individual fiber to have a linear relationship between its 1st Piola-Kirchoff stress and its stretch (λ^i_c)([8, 78])

$$\tilde{\Psi}^i_{L,c}\left(\lambda^i_c\right) = \frac{k^i_{L,c}}{2} \cdot \left(\lambda^i_c - 1\right)^2 \tag{3.18}$$

where $K_{L,c}$ is a stiffness-like material constant,

$$\lambda^i_c = \begin{cases} \dfrac{\lambda^i_{4c}}{\lambda^i_{Rc}}, & \lambda^i_{4c} \geq \lambda^i_{Rc} \\ 1, & \text{otherwise} , \end{cases} \tag{3.19}$$

where $\lambda^i_{4c} = \sqrt{I^i_{4c}}$. Therefore, the Cauchy stress tensor $\sigma_{L,c}$ can be calculated as a function of λ^i_{4c}:

$$\underline{\sigma}_{L,c} = \lambda^i_{4c}\frac{\delta}{\delta\lambda^i_{4c}} \int_1^{\lambda^i_{4c}} \frac{k^i_{L,c}}{2}\left(\frac{\lambda^i_{4c}}{\lambda^i_{Rc}} - 1\right)^2 \rho(\lambda^i_{Rc})\underline{a}^i_c \otimes \underline{a}^i_c d\lambda^i_{Rc} \tag{3.20}$$

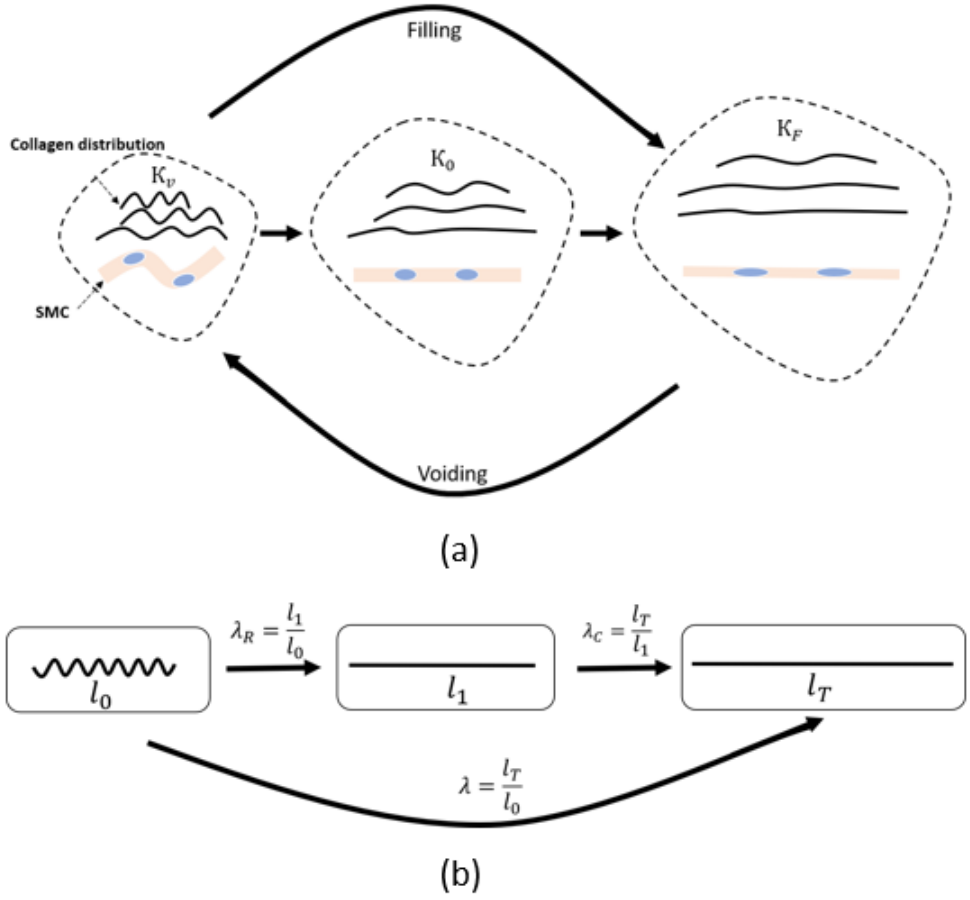

Figure 28: Schematic simplification of (a) structural transformation during filling and voiding. From left to right shows the voided state (κ_V), the unloaded state (κ_0), the filled state of normal capacity (κ_F). (b) three states of constituents (collagen, SMC) during loading. l_0, l_1, l_T denote the tissue length at the state of unloaded, barely recruited, and stretched. λ_R is the constituent recruitment stretch defined as the ratio of l_1 to l_0. λ_C is the constituent stretch defined as the ratio of l_T to l_1. λ is the total tissue stretch defined as the ratio of l_T to l_0.

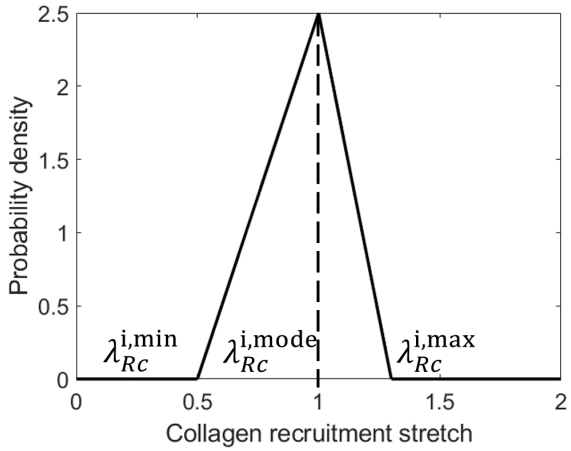

Figure 29: Schematic of triangular distribution of collagen recruitment stretch

The fiber recruitment distribution is represented with a triangular probability density function $\rho_{Rc}^{i}(\lambda_{Rc}^{i})$ [18, 8, 13, 78]; $\lambda_{Rc}^{i,q}$ relates to the the minimum ($q = min$), modal ($q = mode$) and maximum ($q = max$) recruitment stretches of the distribution, Figure 29. More specifically:

$$\rho_R^i\left(\lambda_{Rc}^i\right) = \begin{cases} 0, & \lambda_{Rc}^i \leq \lambda_{Rc}^{i,min} \\ g_1(\lambda_{Rc}^i), & \lambda_{Rc}^{i,min} < \lambda_{Rc}^i \leq \lambda_{Rc}^{i,mode} \\ g_2(\lambda_{Rc}^i), & \lambda_{Rc}^{i,mode} < \lambda_{Rc}^i \leq \lambda_{Rc}^{i,max} \\ 0, & \lambda_{Rc}^{i,max} < \lambda_{Rc}^i, \end{cases} \tag{3.21}$$

where

$$\begin{aligned} g_1(\lambda_{Rc}^i) &= \frac{2\left(\lambda_R^i - \lambda_{Rc}^{i,min}\right)}{\left(\lambda_R^{i,max} - \lambda_{Rc}^{i,min}\right)\left(\lambda_{Rc}^{i,mode} - \lambda_{Rc}^{i,min}\right)} \\ g_2(\lambda_{Rc}^i) &= \frac{2\left(\lambda_{Rc}^{i,max} - \lambda_{4r}^i\right)}{\left(\lambda_{Rc}^{i,max} - \lambda_{Rc}^{i,min}\right)\left(\lambda_{Rc}^{i,max} - \lambda_{Rc}^{i,mode}\right)}. \end{aligned} \tag{3.22}$$

Insertion of equations 3.19 and 3.21 into 3.17 followed by integration yields analytic expressions for the strain energy from which analytic expressions for the stress can be derived (see [78]).

We determined the three main parameters of the distribution ($\lambda_{Rc}^{i,min}$, $\lambda_{Rc}^{i,mode}$, $\lambda_{Rc}^{i,max}$) by

fitting the cumulative triangular probability function using the tissue stretch and collagen fiber recruitment fraction data obtained using method described in 3.2.1.5, as shown in Figure 27. The estimation of collagen fiber recruitment stretch helped us to understand the loading mechanism of bladder and formulate hypothesis of collagen fiber layer dependent role in the model.

3.2.2.5 SMC Active Stress

The active stress generated by the bladder during voiding is correlated to nerve activity [53] and occurs over a large range of bladder contractility [82], i.e. the active stress is generated within a range of SMC stretch, λ_m^{min} to λ_m^{max}, and is zero outside this range. We define the active (Cauchy) stress tensor, $\underline{\sigma}_a$,

$$\underline{\sigma}_a = \sigma_m^{act}\, \underline{a}_m \otimes \underline{a}_m \tag{3.23}$$

where, σ_m^{act} is defined to be a function of SMC stretch (λ_m), nervous stimuli $S(t)$ and normalised SMC mass-density m_m, i.e. $\sigma_m^{act} = \sigma_m^{act}(S(t), m_m(\tau), \lambda_m(t))$.

$$\sigma_m^{act} = \begin{cases} S(t) m_m k_m^{act} (\lambda_m)^4 (\lambda_m - \lambda_m^{min})(\lambda_m^{max} - \lambda_m) & \lambda_m^{min} \leq \lambda_m \leq \lambda_m^{max} \\ 0 & \text{otherwise} \end{cases} \tag{3.24}$$

The neurogenic control system of the bladder is complex with feedback loops such as voiding and guarding reflexes instigated by afferent and efferent nerve signals continuously transmitted between the bladder, urethra, and sphincters [84]. Despite the complexity of the bladder neurogenic control system, the neurogenic control of micturition can be idealized. For example, Fletcher et al. [29] idealize the contraction and relaxation of bladder musculature as being controlled by a nerve signal quantified as a normalized stepwise linear function. In this work, we extend the work of Fletcher et al. to include boht the normalized function of stimuli as a smoothed stepwise function as well as a feedback mechanism to decrease the stimulus

and relax the muscle when the flow rate falls below a critical value Q_{crit} ($Q_{crit} = 0.02ml/s$) at $t = t_{crit}$, i.e.

$$S(t) = \begin{cases} 1 - \frac{1}{1+(t/k_1)^4} & 0 \leq t \leq t_{crit} \\ \left(1 - \frac{1}{1+(t_{crit}/k_1)^4}\right)\left(\frac{1}{1+((t-t_{crit})/k_2)^4}\right) & t_{crit} < t \leq t_{end} \\ 0 & t > t_{end} \end{cases} \tag{3.25}$$

where $k_1 = 1$ and $k_2 = 2$ control the rate of increase and decrease of signal strength, respectively; t_{end} denotes when $Q(t) = 0$.

Table 6: Parameter values relevant to the model of contractility and micturition with the description of methods.

Parameters	Value	Method
λ_M^{min}	0.25	Based on [71], $\lambda_M^{max} > 8\lambda_M^{min}$
λ_M^{max}	2.5	
k_M^{act}	6212 Pa	Estimated by the maximum voiding pressure in cystometry
P_c	380 Pa	Determined by the estimated pressure at κ_V
α	$3.5e^{-5}ml/spa$	Estimated based on the total voiding period

3.2.3 Micturition Model

3.2.3.1 Active Bladder

In the active bladder state, the SMCs are able to generate sufficient wall tension to overcome the urethral outlet resistance and induce voiding. For the *in silico* model, this process is simulated through a coupling between SMC stretch and the active stress generated by the SMCs. In particular, as the bladder fills and enlarges, the nervous stimulus function $S(t)$ is triggered when the SMC stretch reaches a critical value, i.e. when ($\lambda_m = \lambda_m^{at}$). Consequently, SMC active stress increases and voiding is initiated when the internal bladder

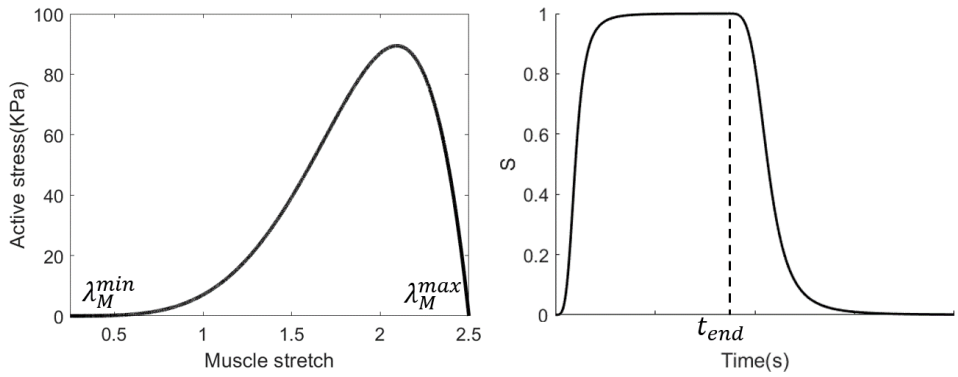

Figure 30: Example plots of (a) muscle stretch dependent active stress function σ_M^{act} (λ_M) and (b) function of normalized stimuli $S(t)$

pressure (*passive + active*) exceeds the cutoff pressure (P_c) at which the urethra opens and closes. Voiding is complete when the internal pressure falls below the cutoff pressure.

The temporal dynamics of the pressure and outflow-rate of the active bladder can be computed during voiding. Following earlier works, we assume a linear relationship between voiding flow rate $Q(t)$ and bladder pressure $P(\lambda, t)$ [38, 10]:

$$Q(t) = \begin{cases} \frac{1}{\alpha}(P(\lambda,t) - P_c) & P(\lambda,t) > P_c \\ 0 & P(\lambda,t) \leq P_c \end{cases} \tag{3.26}$$

where $\frac{1}{\alpha}$ is the slope of the urethral resistance relationship. As voiding progresses, the updated volume is computed to calculate updated pressure $(P(\lambda, t))$. On completion of voiding, relevant metrics are calculated (volume voided, residual volume, voiding duration, contractile range).

3.2.4 Spherical Membrane Model of Bladder

In this work, we apply the general constitutive model above to the case of quasi-static inflation of an incompressible, two-layered nonlinear elastic, spherical membrane. Each wall component is idealized as having an isotropic contribution. In the absence of external body forces, the displacement field must satisfy $\nabla \cdot \underline{\sigma} = 0$ where, as previously noted, $\underline{\sigma}$ is the Cauchy stress tensor.

During the deformation, the spherical membrane with unloaded radius R_0 is inflated to radius $R(s)$ due to an applied transmural pressure P. The corresponding kinematics in spherical coordinates $(\underline{e}_r, \underline{e}_\phi, \underline{e}_\theta)$ are:

$$\underline{F} = \text{Diag}[1/\lambda^2, \lambda, \lambda], \qquad \underline{B} = \text{Diag}[1/\lambda^4, \lambda^2, \lambda^2], \tag{3.27}$$

where, λ denotes the tissue stretch (R/R_0), with reference to the unloaded state κ_0. Due to the symmetry of the loading conditions and the symmetry of the material response, $\sigma_{\phi\phi} = \sigma_{\theta\theta}$, which we simply denote as σ. Employing the governing equation for mechanical equilibrium of the membrane and the boundary conditions, it follows that,

$$P = \frac{2H_0}{R_0\lambda^3}\left(r^H_{LP}\sigma_{c,LP} + r^H_{DSM}(\sigma_e + \sigma_{c,DSM} + \sigma^{act}_m) + r^H_{ADV}\sigma_{c,ADV}\right) \tag{3.28}$$

where r^H_L denotes the ratio of the thickness of layer L to total wall thickness H_0 where $L = LP, DSM, ADV$. σ_e denotes the Cauchy stress of elastin, σ_{c_L} denotes the Cauchy stress of collagen in layer L and σ^{act}_m denotes the active Cauchy stress of smooth muscle; H_0 and R_0 denote the thickness and radius at the unloaded state, respectively. It should be recalled, that for this study, each contribution is idealized as isotropic.

3.3 Results

3.3.1 Passive mechanical response of the bladder wall

The raw data and fitted curves from biaxial testing for each sample are shown in Figure 31 averaged for the longitudinal and circumferential directions. According to Table 7, the average stiffness modulus of collagen fiber k_C is 1e6 which is much higher than the non-collagenase components k_{NC}. The individual plots of the probability density function of collagen recruitment distribution are shown in Figure 32. For samples Y02, Y03, Y04, the DSM fiber recruitment starts earlier than LP fibers. For samples Y01, even the DSM and LP collagen fibers recruitment almost starts at the same time, the DSM recruitment happens much quicker than LP due to the skew of the distribution. Thus, in general, LP acts as a protective sheath.

Table 7: Summary of all fitted parameters for the passive mechanical response. Values of stiffness terms are in units of Pa.

Parameters		Y01	Y02	Y03	Y04	Average	STD
k_{NC}		820	1510	232	1468	1007	606
k_C^{DSM}		6.2e5	1.6e6	1.1e6	1.1e6	1.1e6	0.4e6
k_C^{LP}		2.5e6	6.4e6	4.4e6	4.4e6	4.4e6	1.4e6
LP	λ_R^{min}	2.1	2.1	2.2	2.2	2.2	0.05
	λ_R^{peak}	2.5	2.4	2.2	2.3	2.4	0.11
	λ_R^{max}	2.6	2.5	2.5	2.7	2.5	0.08
DSM	λ_R^{min}	2.0	2.0	1.9	2.0	2.0	0.04
	λ_R^{peak}	2.1	2.1	2.0	2.1	2.1	0.04
	λ_R^{max}	2.6	2.2	2.4	2.8	2.5	0.20

3.3.2 The Role of Bladder Constituents for Mechanical Function

Figure 33 shows the intramural stress on each component of the bladder during filling and voiding at the normal capacity. During the early filling stage, the non-collagenase components (light) dominate the passive response (purple) and passive stress is very low. When the bladder reaches its normal capacity, the muscle active stress (blue dashed) kicks in and dominates the total stress (blue). The collagen fiber only gets recruited if the bladder passes its normal capacity. DSM collagen fibers were recruited earlier than the LP collagen fibers. Once the collagen fibers kicked in, the curve of total passive stress becomes steep. This indicates that collagen fibers in the bladder play a role in preventing over-extension.

The stress curve of voiding at different bladder fullness (70% capacity, 100% capacity, 110% capacity) is shown in Figure 40. The voiding at a larger initial stretch can generate larger stress. This is because higher initial stretch has both higher passive stress and active stress. At 110% capacity, there is high passive stress caused by the recruitment of collagen fibers before the onset of voiding. The high passive stress helps to generate flow in the urethra at $t = 0$, see Figure 39b.

3.3.3 Simulation of Bladder Urodynamics

The urodynamic study is the gold standard for the diagnosis of dysfunction bladder. It plots the pressure and flow rate with time and allows one to make a diagnosis of voiding and storage abnormalities responsible for LUTS. In this study, we simulate the bladder urodynamics during the voiding phase to understand the bladder voiding function (see Fig-

Table 8: Dimensions of young bladders (n=4)

Young	Y01	Y02	Y03	Y04	Average	STD
unloaded width W_0 (mm)	4.31	5.05	4.76	4.84	4.74	0.27
unloaded height Y_0 (mm)	11.10	10.32	9.64	9.36	10.10	0.67
unloaded thickness H_0 (mm)	0.72	0.71	0.85	0.82	0.78	0.06

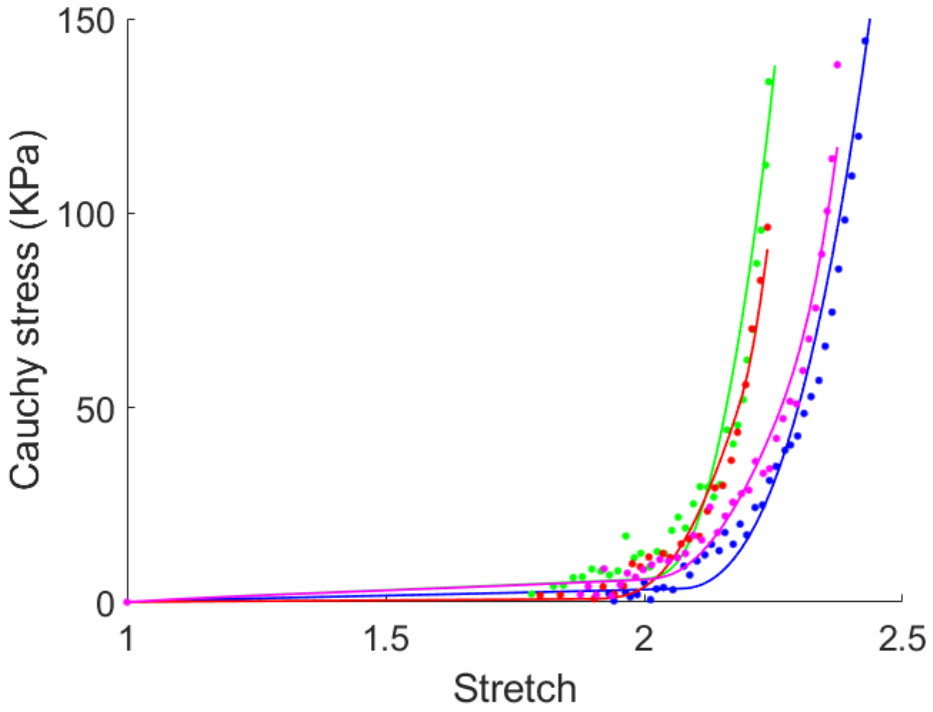

Figure 31: Quantitative measurement of bladder mechanical properties and fiber distribution: (a) data fitting of mechanical loading curves ($n = 4$, blue: R^2=0.97, green: R^2=0.92, red: R^2=0.97, purple: R^2=0.97)

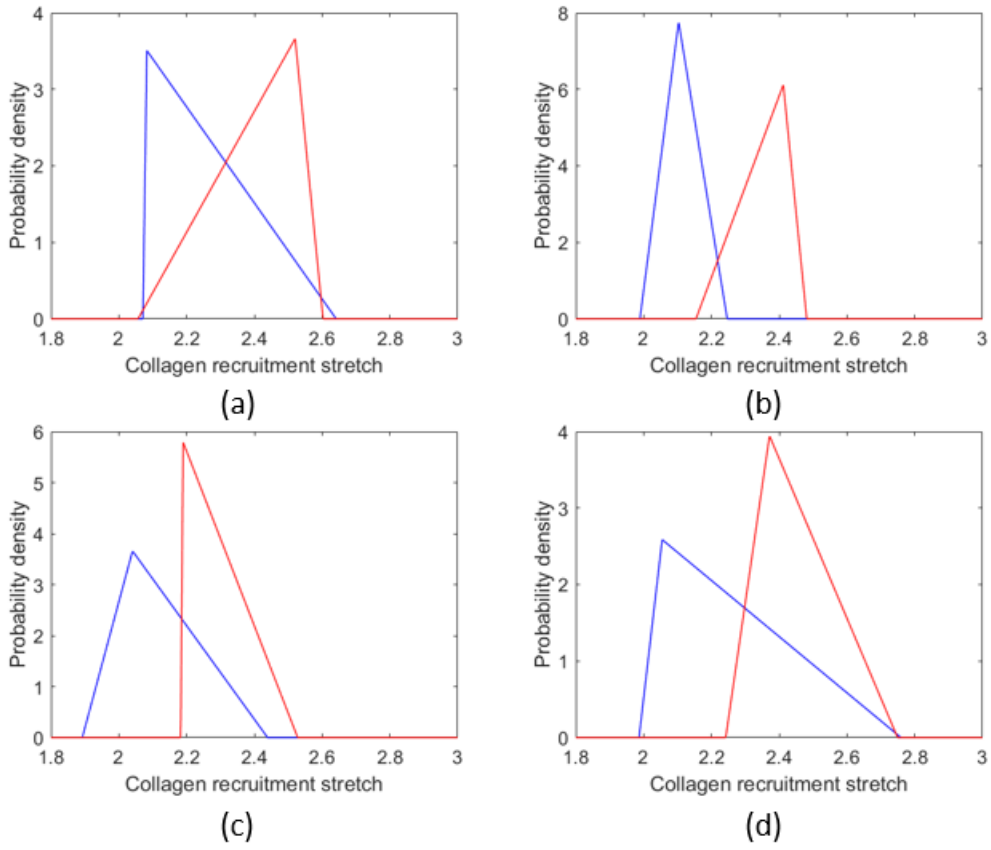

Figure 32: Plots of the probability density function of collagen recruitment stretch distribution (directly measured from MPM images) (a) sample Y01 (b) sample Y02 (c) sample Y03 (d) sample Y04. Blue represents DSM and red represents LP.

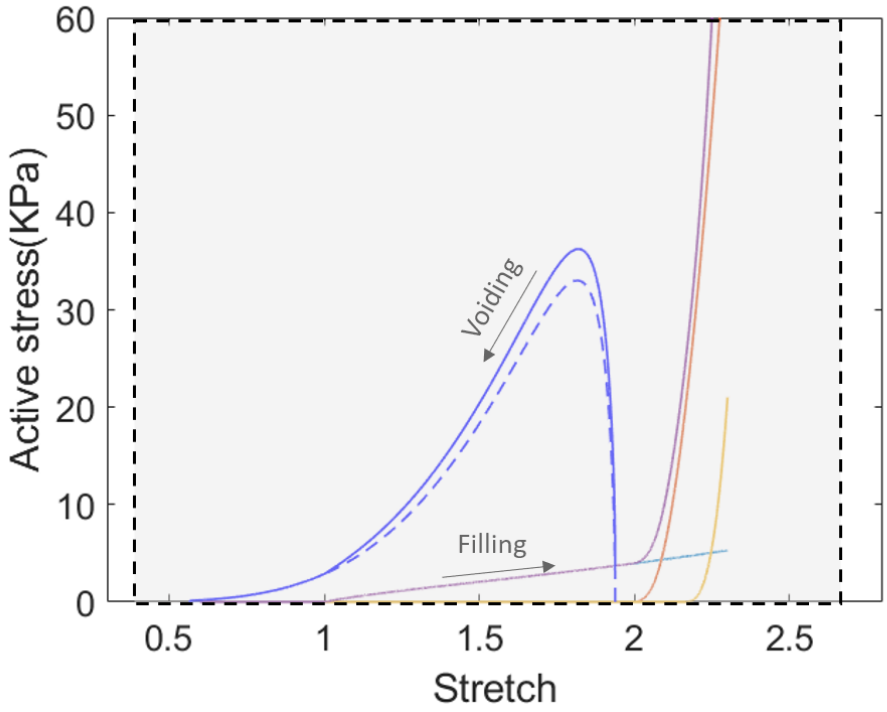

Figure 33: The intramural stress versus stretch (relative to κ_0) during bladder filling and voiding at the normal capacity: total stress during filling (purple), total stress during voiding (blue), muscle active stress during voiding (blue dash), the stress of DSM collagen (red), the stress of LP collagen (yellow), and stress of elastin components (light blue). The region highlighted by the dashed box shows the working range of SMCs. Stretch is relative to κ_0.

Table 9: In vivo measured cystometry parameters.

Quantities	symbol	Young
voided volume (ml)	ΔV_{void}	0.84 $\pm$ 0.03
post void volume = residual volume (ml)	V_{PV}	0.02 $\pm$ 0.008
void duration (s)	Δt_{void}	12 $\pm$ 0.4
max filling pressure (Pa)	$P_{max}^{passive}$	300 $\pm$ 80
max void pressure (Pa)	$P_{max}^{voiding}$	3900 $\pm$ 220

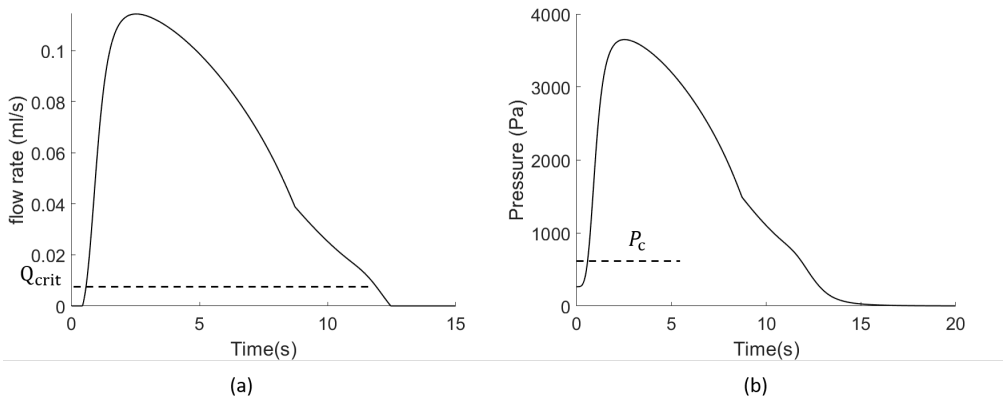

Figure 34: The simulated urodynamic curves during the voiding phase: (a) flow rate vs. time (b) pressure vs. time. Baseline of k_1 is chosen to be 1 and k_2 is chosen to be 2.

ure 34). Before the active response is initiated, the bladder pressure is dominated by the passive response and that's why we see an initial pressure at t=0 (see Figure 34b). After the contraction starts, the bladder pressure increases but the voiding doesn't start until the pressure reaches P_c (the minimum pressure required to generate flow in the urethra). The flow/pressure curves can be generally divided into two phases: an increasing phase and a decreasing phase. During the increasing phase, the active response is dominated by nervous stimulation. Thus, the pressure/flow rate increases in a linear fashion. During the decreasing phase, the nervous stimulation is maintained at the maximum level, the curve is now dominated by the stretch-dependent stress σ_M. When the flow rate drops below the critical threshold Q_{crit} (Figure 34a), the muscle starts to relax caused by a gradual decrease of nerve stimulation. The complete relaxation is done after the flow stops.

3.3.4 Radius Changes with Time

From Figure 35, we can see that radius of the bladder remains unchanged at the beginning of contraction. This is because initiating the flow in the urethra requires a minimum bladder pressure (P_c). After the voiding starts, the radius decreases nearly linearly with time.

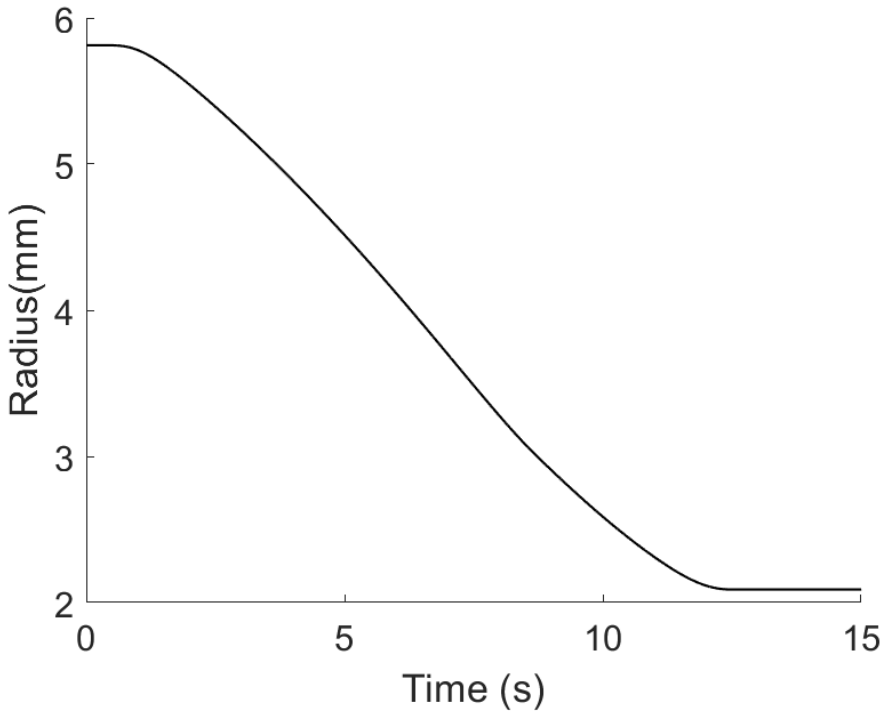

Figure 35: Radius vs. time during the voiding phase. Baseline of k_1 is chosen to be 1 and k_2 is chosen to be 2.

3.3.5 The Effect on Voiding of Nervous Control

Increasing k_1 will delay the full activation of SMCs and thus delay the onset of voiding, Figure 36a. As a result, the maximum voiding pressure are reached at a lower stretch with smaller magnitude, Figure 37b. Figure 36 shows that as k_1 increase, the time stays at the maximum stimulation, the maximum pressure, and maximum flow rate decrease which causes the increase of total voiding time increases. In facts, there is a linear relationship between the k_1 and total voiding time (Figure 37a).

3.3.6 The Effect on Voiding of Bladder Fullness

Figure 39 shows that both the bladder maximum pressure and flow rate increase with the initial volume. From 70% to 100% capacity, the maximum pressure and flow rate increases because when the voiding starts at the left side of the peak, the higher initial volume is corresponding to higher maximum active pressure (Figure16). From 100% to 110% capacity, the maximum pressure and flow increases mainly because of the high passive stress caused by the recruitment of collagen fibers (Figure 40). According to Figure 39, the total voiding duration increase even though voiding with higher initial volume can generate higher maximum pressure.

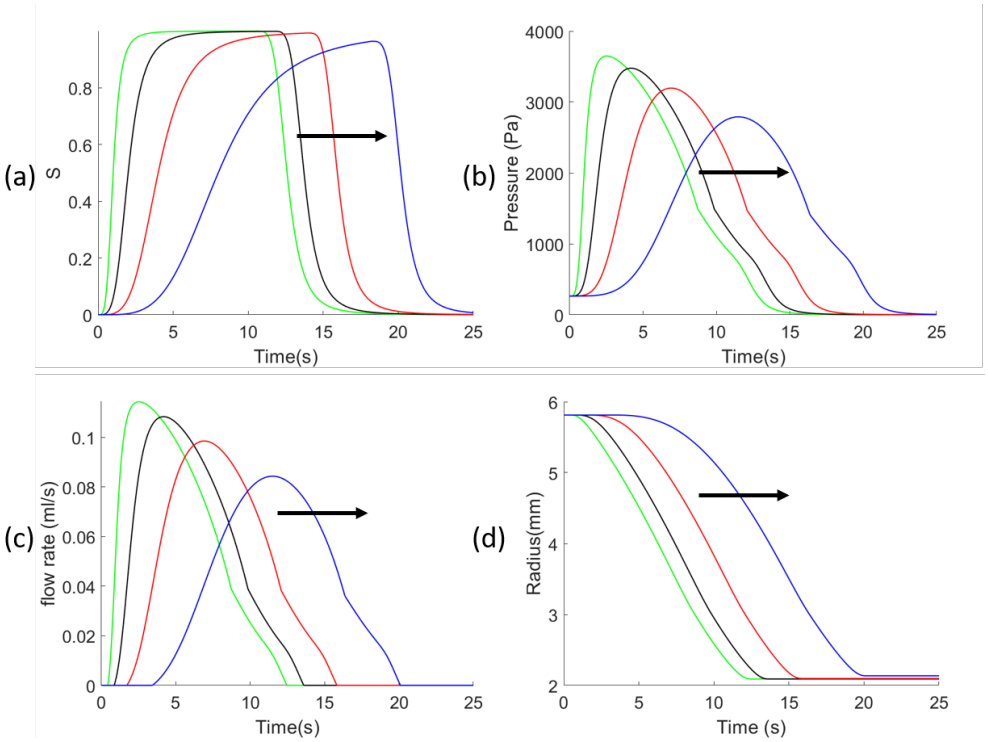

Figure 36: The effect of nervous stimulation constant k_1 on voiding function. Plots include (a) normalized nervous stimulation vs. time (b) pressure vs. time (c) flow rate vs. time (d) radius vs. time. The values of k_1 are 1, 2, 4, and 8 with the arrow showing increasing k_1

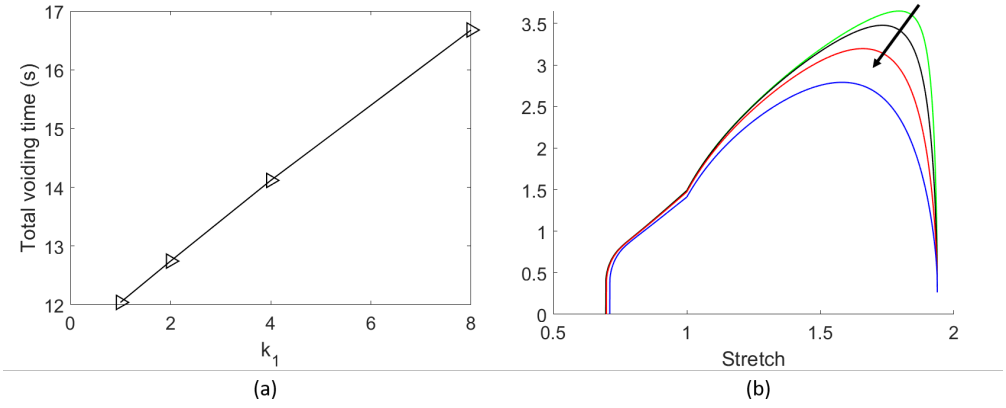

Figure 37: (a) The relation between k_1 and total voiding time (b) The stretch and pressure relation for $k_1 = 1, 2, 4, 8$ (the arrow shows increasing k_1).

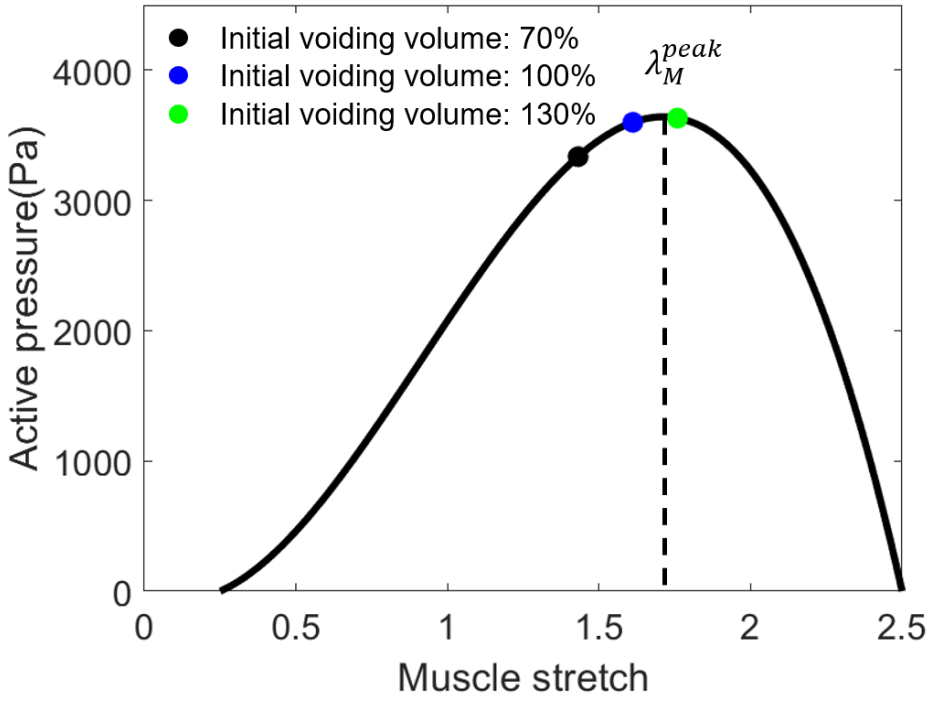

Figure 38: The relation between muscle stretch and active pressure when nervous stimuli reaches maximum (S = 1). The dots label three different initial voiding volume (black: 70% capacity, blue: 100% capacity, and green: 130% capacity)

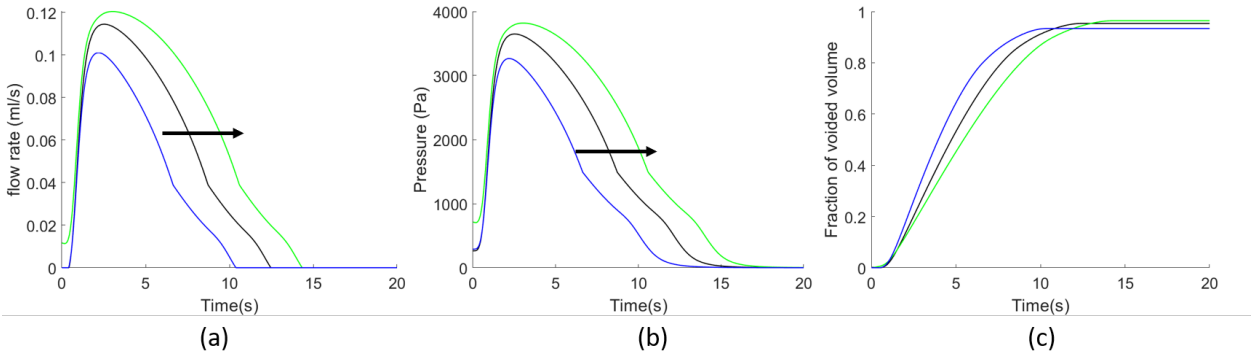

Figure 39: The effect of initial volume on voiding function. Plots include (a) pressure vs. time (b) flow rate vs. time and (c) fraction of voided volume for three different initial volumes: 70%, 100%, and 130% of the bladder capacity vs. time with the arrow showing increasing initial volume. Baseline of k_1 is chosen to be 1 and k_2 is chosen to be 2.

3.4 Discussion

3.4.1 Novelties

Traditional mathematical models for bladder can be categorized into two types: the constitutive model and the micturition model. The constitutive model focused on material properties of the bladder tissue (elasticity and contractility) but disregard the connection between the material properties and the micturition function. The micturition model focused on the interaction between the bladder contractility, neutral control, and urethra resistance but often ignored the bladder elasticity. Our model integrated a novel microstructural motivated constitutive model with a micturition framework. For the first time, we were able to understand the bladder function from the material properties of its components.

3.4.2 Experiments Informed Novel Microstructural Model

To date, the constitutive modeling of the bladder has been largely phenomenological [23] [12] [85]. The microstructural modeling of collagen fiber only existed in a few studies [89]

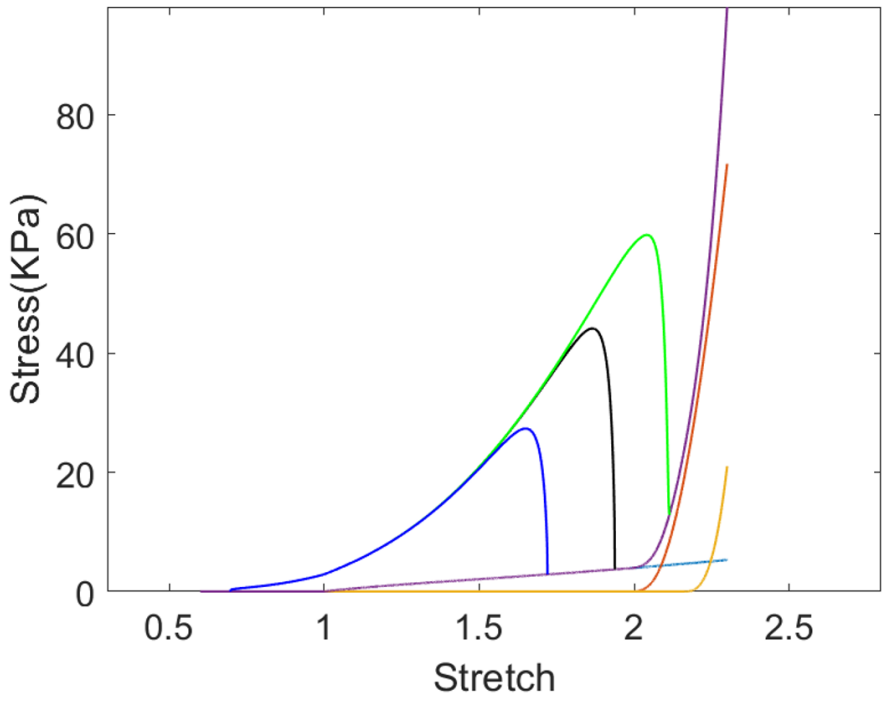

Figure 40: The stress during bladder filling and voiding at the capacity 70%, 100%, and 130%: total stress during filling (purple), total stress during voiding (green: 130% capacity, black: 100% capacity, blue: 70% capacity), the stress of DSM collagen (red), stress of LP collagen (yellow), and stress of non-collagenase components (light blue). Baseline of k_1 is chosen to be 1 and k_2 is chosen to be 2.

[59]. However, these studies were theoretical studies with little experimental validation or quantification. We presented a microstructural mechanical model that is informed by the collagen fiber distribution directly measured from 3D reconstructed MPM images. As we noticed the collagen fiber distribution for the two main layers is substantially different [20], the collagen fiber distribution for individual layers was measured separately. Our model, for the first time, allows individual constituents and layers of the bladder tissue to be coupled back to the gross mechanical response.

3.4.3 Optimal Bladder Function

As shown in Figure 33, we found that the collagen fibers were only recruited after the bladder reached its normal capacity and within the muscle work range. If the collagen fibers were recruited earlier, the bladder lost its compliance. If the collagen fibers were recruited later and out of the working range of the muscle (indicated by the dashed box in Figure 33), the bladder stored more of urine but lost voiding capacity. Interestingly, these two scenarios correspond to the two main types of bladder dysfunction: non-compliant bladder and over-compliant bladder.

In conclusion, when collagen fibers are recruited right after the bladder reaches capacity, the bladder achieves optimal function. On one hand, it allows the bladder to store urine at low pressure. On the other hand, it prevents over-extension of the bladder and ensures the bladder is always within the muscle working range. In the cases of voiding at higher volume (Figure 40), the higher stress caused by the recruitment of collagen fibers can also contribute to the initial voiding.

3.5 Future work

3.5.1 Complete Neurogenic Control Model

As mentioned previously, the neurogenic control system has various feedback loops and is extremely complicated. In the present study, the neurogenic control of the bladder is

simplified and not based on physiological data. A feedback mechanism is assumed so that the muscle is not relaxed until voiding is completed and this allows the bladder to efficiently empty itself at any initial volume. Even though the simplified model adequately described realistic response and allowed investigation of the other non-neural components of the system, a more complete neurogenic control model is desirable in the future.

3.5.2 Growth and Remodeling Model

The bladder tissue constantly remodels itself during aging [74] [17] [20] and in response to the mechanical environment [50] [17] [36]. Remodeling of the bladder microstructure can dramatically alter its function. For instance, in the aged bladder tissue, premature fiber recruitment found in the DSM layer causes significant loss of bladder compliance [20]. To predict the mechanical function, it's important to understand its homeostatic tendency to adapt in response to changes in the mechanical environment. In the future, our model can be further developed to examine the role of growth and remodeling response in dysfunctional bladders.

The early bladder constitutive models including [23] [12] [85] are so-called phenomenological models which provided the stress-strain relation but cannot capture the underlying mechanism contributing to tissue behavior and the model parameters are not based on physiological phenomena. In recent years, structural models [89, 59] were developed based on collagen fiber recruitment and orientation. These types of models can relate the tissue level mechanical response to individual collagen fiber properties. Microstructurally motivated constitutive models for bladder tissue have been developed [45, 20].

Traditional micturition models[39, 25, 83, 67, 28] modeled the urethral resistance relation that relates detrusor pressure/contractile force to flow rate during voiding with the focus on nervous control of the SMC. These models predict muscle contraction force simply by assuming a relationship between contraction velocity and muscle contraction[28] and don't explain the underlying mechanism of the muscle.

Over the years, studies have been conducted to understand the mechanics of bladder tissue through mechanical testing with the focus gradually shifting from quantifying the

bladder material properties [35, 58, 79, 86] to understanding the association between load transfer mechanism and the bladder's microstructure [33, 45, 20, 15, 81]. Early constitutive models of bladder wall are phenomenological [23] [12] and don't explain the correspondence between individual model components and the bladder function.

3.6 Conclusion

We present a novel hybrid model that couples a constrained mixture model with a micturition framework. The model included the bladder elasticity,contractility, nervous control, and urethra resistance relation (URR) and was informed by both in-vivo (planar biaxial testing) and ex-vivo (cystometry) experiments. This model, for the first time, has the potential to infer the structural changes that are primarily responsible the change of mechanical function from the urodynamics data.

3.7 Acknowledgement

The author gratefully acknowledges Dr. Yoshimura for providing the rat bladder tissue for planar biaxial testing as well as the data from cystometry.

3.8 Appendix: Analytic Solution of Stress for Sphere Inflation and Equi-biaxial Stretch

3.8.1 Introduction

An exponential dependence of stress on stretch was proposed by [30] and is commonly used for soft biological tissues. In Chapter 2, we found that the exponential model fits data with an $R^2 > 0.94$ for all samples. Therefore, we would like to use this simple model to understand the difference of stretch-stress relationship between sphere inflation and equi-biaxial stretch.

The Cauchy stress tensor of the exponential model is

$$\underline{\sigma} = -p\underline{I} + \mu\, e^{\gamma(I_1-3)}\underline{B} \tag{3.29}$$

where p is the Lagrange multiplier associated with incompressiblity, I_1 is the first invariant of the left Cauchy-Green deformation tensor, $\underline{B}$,

$$I_1 = tr(\underline{B}), \tag{3.30}$$

μ is the shear modulus and material constant γ controls the exponential dependence on I_1.

3.8.2 Analytic Solution for Spherical Inflation of a Membrane

In this section, we recall the solution for inflation of a spherical membrane of current radius R and thickness H under transmural pressure P. The unloaded radius and thickness are denoted as R_0 and H_0, respectively. The Cauchy stress as a function of stretch $\lambda = R/R_0$ for a spherical membrane composed of the isotropic, exponential material described above (see, e.g. [11]) is

$$P(\lambda) = \frac{2H_0}{\lambda R_0}\,[1 - \frac{1}{\lambda^6}]\mu e^{\gamma(I_1-3)} \tag{3.31}$$

It follows from equilibrium that the relationship between pressure and stress in a spherical membrane is

$$\sigma_{rr}(\lambda) = P(\lambda)\frac{{R_0}^2}{2H_0\lambda^3}. \tag{3.32}$$

and therefore, the Cauchy stress as a function of stretch for spherical inflation can be expressed as

$$\sigma_{rr}(\lambda) = (\lambda^2 - \frac{1}{\lambda^4})\mu e^{(\gamma(I_1-3))}. \tag{3.33}$$

3.8.3 Analytic Solution of Stress for Equi-biaxial Stretch

In this section, we recall the solution for equi-biaxial planar stretch of a square specimen of unloaded length L_0 and thickness $\bar{H}_0$ to loaded length and thickness L and $\bar{H}$, respectively. The Cauchy stress as a function of stretch $\bar{\lambda} = L/L_0$ during planar equi-biaxial stretch of the isotropic exponential material,

$$\sigma_{11} = \sigma_{22} = \bar{\lambda}^2\mu e^{(\gamma(\bar{I}_1-3))} - p \qquad \sigma_{33} = \frac{\mu e^{(\gamma(\bar{I}_1-3))}}{\bar{\lambda}^4} - p \tag{3.34}$$

where $\bar{I}_1 =$ If we apply the stress free boundary condition to the top surface with normal $\bar{e}_3$, we can solve for the Lagrange multiplier as

$$p = \frac{\mu e^{\gamma(\bar{I}_1-3)}}{\bar{\lambda}^4}. \tag{3.35}$$

The solution for planar biaxial stress can therefore be expressed as

$$\sigma_{11} = \sigma_{22} = (\bar{\lambda}^2 - \frac{1}{\bar{\lambda}^4})\mu e^{\gamma(\bar{I}_1-3)} \tag{3.36}$$

3.8.4 Conclusion

The functional form for the solution for Cauchy stress as a function of stretch is identical for spherical inflation and planar equi-biaxial stretch of a membrane, despite the different definitions of stretch.

4.0 A Mechanobiological Model of the Urinary Bladder: Integrative Modelling of Outlet Obstruction

4.1 Introduction

The function of the bladder is to serve as a low pressure reservoir for storing urine and then efficiently expel this urine at a convenient time. Bladder outlet obstruction (BOO) is a urodynamic diagnosis that signifies the existence of increased urethral resistance, sufficient to alter the voiding process. Over time, BOO can lead to changes in the bladder's storage capacity as well. A clinical diagnosis of BOO is based on the presence of specific changes to the bladder pressure flow relationship that are defined in the International Continence Society (ICS) Standardisation report and can be measured using urodynamic studies [1]. The mechanical causes of BOO include an enlarged prostate, such as induced by benign prostatic hyperplasia (BPH) [64, 65, 69] and urethral narrowing from scarring or strictures [40, 80, 5]. BPH induced BOO is increasingly prevalent for men over the age of 50, with 50 - 75% of men over age 50 and 80% of men over age 70 experiencing lower urinary tract symptoms (LUTS) as a result of BPH[26], voiding hesitancy, prolonged micturition, incomplete bladder emptying, increased urination frequency, urgency, and incontinence, which dramatically lower the quality of life, both physically and psychologically [61]. Two-thirds or more of the men with BOO have storage problems where there is increased urinary frequency associated with urgency to void, and the majority of these patients have bladder overactivity that is measurable in urodynamic testing [37]. The economic burden of BPH induced BOO is significant; 4 billion dollars annually in 2006, a sum that will only increase as the US population continues to age [77].

The structure of the bladder wall is often considered with respect to three layers: the mucosa, the muscularis propria (herein referred to as the detrusor smooth muscle (DSM) layer) and the adventitia. The mucosa is the innermost layer and is composed of an urothelium, a basement membrane and a lamina propria (LP) which contains a densely packed, interwoven network of collagen fibers. The DSM is a composite of smooth muscle cell (SMC) bundles

intermixed with collagen and elastin fibers and the outer surface of the bladder is formed of loose connective tissue commonly termed the adventitia. During filling, the unfolding of the tissue layers allow the bladder to expand under low pressure[20]. To void, the contraction of the muscle cells is triggered to generate active stress and initiate flow by overcoming the urethral resistance.

In silico models of the bladder that have been developed to date can, broadly speaking, be classified into two main types: constitutive models [**?**, 23, 47, 12, 90, 59, 45, 20, 15, 81] and whole bladder micturition models [39, 25, 83, 67, 28, 72]. The constitutive models focus on the strain-stress relation for the passive and, in some cases, active mechanical response, whilst the micturition models focus on simulating the pressure-flow relation of the bladder during voiding.

The bladder, like other soft tissues can alter its constituents and geometry through a growth and remodeling process. Recently, we developed an integrated constitutive model that combines a constrained-mixture model of this G&R process for the bladder wall with a micturition model[22]. Using this model, urodynamic curves can be interpreted with respect to the underlying microstructure (and vice-versa), providing fundamental insight into the structure-function relation of the bladder during filling and voiding. This coupled micturition/GR model has the potential to provide insights into bladder pathophysiology and its effect on bladder function. In the present work, we extend this model to the BOO bladder.

In bladders with BOO, the urethral resistance increases, requiring the SMC in the wall to generate larger pressures to void, inducing a growth and remodeling (G&R) response that leads to changes in bladder size and tissue composition [32]. While this G&R response can restore voiding, there can be associated deficits in mechanical function such as weak stream, incomplete emptying, and increased voiding frequency. The changes to bladder functionality are intimately related to changes in the mechanics and microstructure of the tissue. Although experimental and computational models of the G&R process, can potentially provide insight into the evolving pathophysiology of the BOO bladder, thus far, no computational models have been developed to simulate the G&R evolution of any bladder disease.

In the present work, we extend cheng2021a model to incorporate G&R scheme and

apply the model to simulate the adaptive response of the bladder to BOO. An integrative interdisciplinary modelling approach is adopted in which an experimental rat model of outlet obstruction is used to inform the *in silico* model. The model is parameterized using data from a healthy rat bladder, BOO is simulated by an increase in outlet resistance and competing hypotheses for the adaptive response of the bladder to increased urethral flow resistance are investigated.

The structure of the paper is as follows: Section 4.2 details the experimental model, protocols for tissue characterization and computational methodology; Section 4.3 illustrates model simulations and compares predictions with experimental observations. Lastly, Section 4.4 concludes with a summary and critique of the model and provides an outlook for future research.

4.2 Methods

We utilise an integrative *in vivo in-vitro in-silico* modelling approach (see Figure 23). An *in silico* model is developed that simulates the mechanics of the micturition cycle in healthy bladder and it's G&R in response to outlet obstruction. Where possible, model parameters are informed from *in vivo* pressure-flow experiments and *in vitro* planar biaxial testing coupled with multi-photon microscopy of the collagen fibers.

4.2.1 Experimental Studies of BOO Model

4.2.1.1 Creation of BOO Model

Male Sprague Dawley rats were used for producing the experimental BOO model [76]. Briefly, under isoflurane anesthesia, the bladder and the proximal urethra were exposed via a lower abdominal midline incision.

A 4-0 silk ligature was placed around the urethra and tied at the urethrovesical junction level proximal to the urethral fenestration with a metal rod (outside catheter diameter of 1.27 mm) placed alongside the urethra, and then the rod was removed. The abdominal wound was closed. This ligation was maintained in place throughout the duration of the experiments. Sham rats underwent similar procedures without urethral ligation.

4.2.1.2 In vivo Measurements: Pressure-flow Study

Twenty four Sprague Dawley rats (twelve BOO and twelve SHAM) were used in the cystometry (pressure-flow) studies, performed 4 weeks after inducing BOO,[76]. Under isoflurane anaesthesia, a PE-50 polyethylene catheter (Clay-Adams, Parsippany, NJ) was inserted through the bladder dome and a purse-string suture was placed tightly around the catheter. The implanted catheter was exteriorized through the abdominal wall, and the wound was closed with 4-0 silk sutures. After the surgery, the rats were placed in restraining cages (W 80 mm × L 300 mm × H 150 mm, Yamanaka Chemical Ind., Ltd, Osaka, Japan) and allowed to recover from isoflurane anaesthesia for 1–2 h before starting cystometry. After recovery, a three-way stopcock was used to connect the intravesical catheter to a pressure transducer (Transbridge 4M, World Precision Instruments, Sarasota, FL, USA) for recording intravesical bladder pressure and to a syringe pump (*company*) for infusing saline at a fixed flowrate. Because variability in bladder capacity among BOO rats is typical of this model, saline was initially infused at 0.1 ml/min; subsequently, the infusion rate was adjusted to 0.04–0.3 ml/min to obtain an intercontraction interval around 10-15 min [60]. Intravesical pressure changes were measured using data acquisition software (AD Instruments, Castle Hill, NSW, Australia) at a sampling rate of 100 Hz using a PowerLab. Saline infusion was continued until stable voiding cycles were established.

The recorded data was used to construct the presssure/flow curves (Figure 24), from which the following parameters were evaluated: (i) maximum voiding pressure $P_{max}^{voiding}$ (the peak pressure minus the basal pressure during each voiding cycle); (ii) maximum passive filling pressure $P_{max}^{passive}$ (the pressure immediately after the reflex contraction minus the basal pressure; the basal pressure is the the passive pressure in the empty bladder and measured

Table 10: In vivo measured parameters for SHAM and BOO experimental models.

Quantities	symbol	SHAM	BOO
void volume (ml)	V_{void}	0.84 $\pm$ 0.03	0.82 $\pm$ 0.12
residual volume (ml)	$V_{residual}$	0.02 $\pm$ 0.008	1.2 $\pm$ 0.23
void duration (s)	t_{void}	12 $\pm$ 0.4	45 $\pm$ 5
max filling pressure (Pa)	$P_{max}^{passive}$	300 $\pm$ 80	280 $\pm$ 70
max void pressure (Pa)	$P_{max}^{voiding}$	3900 $\pm$ 220	8900 $\pm$ 640

from the lowest pressure during cystometry). We define the maximum active voiding pressure (P_{max}^{active}) as the difference between maximum voiding pressure and maximum passive filling pressure, i.e. $P_{max}^{active} = P_{max}^{voiding} - P_{max}^{passive}$. Measured quantities are summarised in Table 10.

Voided urine was collected using a plastic cup placed underneath the restraining cage and measured to determine the voided volume (V_{void}), and post-void residual volume V_v was collected and measured by draining the post-void bladder using the bladder catheter with gravity [76]. Bladder capacity (V_F) was calculated as the sum of voided and residual volumes. After the bladder was harvested, the ex-vivo unloaded width (W_0), height (D_0) and thickness of the bladder were measured (see Tables. 11 and 12).

Table 11: Dimensions of Sham bladders (n=4)

Sham	S01	S02	S03	S04	Average	STD
unloaded width W_0 (mm)	4.31	5.05	4.76	4.84	4.74	0.27
unloaded height D_0 (mm)	11.10	10.32	9.64	9.36	10.10	0.67
unloaded thickness t_0 (mm)	0.72	0.71	0.85	0.82	0.78	0.06

Table 12: Dimensions of BOO bladders (n=4)

BOO	B01	B02	B03	B04	Average	STD
unloaded width W_O (mm)	7.92	8.40	9.38	10.08	8.95	0.84
unloaded height D_0 (mm)	19.14	17.39	13.75	15.35	16.41	2.04
unloaded thickness (mm)	1.61	1.53	1.98	1.10	1.56	0.36

4.2.2 Constitutive Modeling for the Bladder Wall Mechanics

The bladder wall experiences large displacements that are modeled as quasi-static and constrained to be isochoric (as the bladder is idealized as incompressible). In the absence of external body forces, the displacement field therefore must satisfy the following equilibrium equation $\nabla \cdot \underline{\sigma} = 0$ where $\underline{\sigma}$ is the Cauchy stress tensor. We assume an additive decomposition of the stresses due to the passive and active components

$$\underline{\sigma} = \underline{\sigma_p} + \underline{\sigma_a}. \tag{4.1}$$

4.2.2.1 Kinematics

The Lagrangian formulation used in this work denotes the deformation gradient as $\underline{F}$, and the right Cauchy-Green tensor as $\underline{C} = \underline{F}^T \underline{F}$. The tensor invariants are $I_1 = tr(\underline{C})$, $I_2 = (tr(\underline{C})^2 - tr(\underline{C}^2))/2$ and $I_3 = \det(\bar{C}) = 1$. The direction of the collagen fibers is denoted by the unit vector $\boldsymbol{a}_c^i$ where i ranges over number of orientations at a point within the tissue. The stretch λ_{4c}^i in the fibre direction is

$$\left(\lambda_{4c}^i\right)^2 = I_{4c}^i = \boldsymbol{a}_c^i \cdot \underline{C} \boldsymbol{a}_c^i \tag{4.2}$$

i.e., associated with I_{4c}^i, a pseudo-invariant of $\underline{C}$ and $\boldsymbol{a}^i$. Similarly, denoting the SMC direction by the unit vector $\boldsymbol{a}_m$, the stretch λ_{4m} in the SMC direction is

$$\left(\lambda_{4m}\right)^2 = I_{4m} = \boldsymbol{a}_m \cdot \underline{C} \boldsymbol{a}_m \tag{4.3}$$

4.2.2.2 Strain-energy Functions

The strain energy function for the passive response of each layer L (where $L = LP$ denotes lamina propria, $L = DSM$ denotes the destrusor muscle layer and $L = ADV$ denotes the advential layer) receives contributions from elastin, passive smooth muscle cells and collagen fibers (anisotropic components). Hence

$$\Psi_L = \Psi_{L,e}(I_1) + \sum_i \Psi^i_{L,c}(I^i_{4c}). \tag{4.4}$$

4.2.2.3 Elastinous Constitutents

The isotropic elastic components are modeled as a neo-Hookean material [88]:

$$\Psi_{L,e} = K_{L,e}\left(I_1 - 3\right), \tag{4.5}$$

with $K_{L,e}$ being stiffness-like material constants.

4.2.2.4 Collagenous Constituents

The constitutive model for the collagen accounts for the experimental observation that collagen fibers have a a distribution of waviness in the unloaded configuration and thus have a distribution of recruitment [**?**]. The strain energy function involves integrating the strain energy for a fiber ($\tilde{\Psi}^i_{L,c}$) over the distribution of recruitment stretches (ρ^i_{RL}),

$$\Psi_{L,c}(I^i_4) = m_{L,c} \cdot \sum_i \int_1^{\sqrt{I^i_4}} \tilde{\Psi}^i_{L,c}\left(\lambda^i_c\right) \rho^i_{RLc}\left(\lambda^i_{RLc}\right) d\lambda^i_{RLc}. \tag{4.6}$$

where $m_{L,c}$ is the (dimensionless) normalized mass density of collagen fibers that can adapt to simulate collagen growth/atrophy[87]. We model each individual fiber to have a linear relationship between its 1st Piola-Kirchoff stress and its stretch (λ^i_c)([8, 78])

$$\tilde{\Psi}^i_{L,c}\left(\lambda^i_c\right) = \begin{cases} \dfrac{k^i_{L,c}}{2} \cdot \left(\lambda^i_c - 1\right)^2 & \lambda^i_c \geq 1 \\ 0, & \text{otherwise}\ , \end{cases} \tag{4.7}$$

where $K_{L,c}$ is a stiffness-like material constant and the fibre stretch λ_c^i is given by

$$\lambda_c^i = \frac{\lambda_{4c}^i}{\lambda_{RLc}^i} \tag{4.8}$$

$\lambda_{RLc}^i = \sqrt{I_{Rc}^i}$ denotes the recruitment stretch of the collagen fiber in layer L, and $\lambda_{4c}^i = \sqrt{I_{4c}^i}$.

The fiber recruitment distribution is represented with a triangular probability density function ρ_{Rc}^i [18, 8, 13, 78]; $\lambda_{Rc}^{i,q}$ relates to the the minimum ($q = min$), modal ($q = mode$) and maximum ($q = max$) recruitment stretches of the distribution (see Figure 29). More specifically:

$$\rho_{RL}^i\left(\lambda_{RLc}^i\right) = \begin{cases} 0, & \lambda_{RLc}^i \leq \lambda_{RLc}^{i,min} \\ g_1(\lambda_{RLc}^i), & \lambda_{RLc}^{i,min} < \lambda_{RLc}^i \leq \lambda_{RLc}^{i,mode} \\ g_2(\lambda_{RLc}^i), & \lambda_{RLc}^{i,mode} < \lambda_{RLc}^i \leq \lambda_{RLc}^{i,max} \\ 0, & \lambda_{RLc}^{i,max} < \lambda_{RLc}^i, \end{cases} \tag{4.9}$$

where

$$\begin{aligned} g_1(\lambda_{RLc}^i) &= \frac{2\left(\lambda_{RLc}^i - \lambda_{RLc}^{i,min}\right)}{\left(\lambda_{RLc}^{i,max} - \lambda_{RLc}^{i,min}\right)\left(\lambda_{Rc}^{i,mode} - \lambda_{RLc}^{i,min}\right)} \\ g_2(\lambda_{RLc}^i) &= \frac{2\left(\lambda_{RLc}^{i,max} - \lambda_{4RLc}^i\right)}{\left(\lambda_{RLc}^{i,max} - \lambda_{RLc}^{i,min}\right)\left(\lambda_{RLc}^{i,max} - \lambda_{RLc}^{i,mode}\right)}. \end{aligned} \tag{4.10}$$

Insertion of equations 4.12 and 4.9 into 4.6 and integration yields analytic expressions for the strain energy from which analytic expressions for the collagen stress can be derived (see [78]). The three main parameters of the distribution ($\lambda_{Rc}^{i,min}$, $\lambda_{Rc}^{i,mode}$, $\lambda_{Rc}^{i,max}$) are inferred from collagen fibre attachment stretch distributions at the onset of voiding.

4.2.2.5 SMC Active Stress

The active stress generated by the bladder during voiding is correlated to nerve activity [53] and occurs over a large range of bladder contractility [82], i.e. the active stress is generated within a range of SMC stretch, λ_m^{min} to λ_m^{max}, and is zero outside this range. We

define the active (Cauchy) stress, σ_m^{act}, to be a function of SMC stretch (λ_m), nervous stimuli $S(t)$ and normalised SMC mass-density m_m, i.e. $\sigma_m^{act} = \sigma_m^{act}(S(t), m_m(\tau), \lambda_m(t))$.

$$\sigma_m^{act} = \begin{cases} S(t) m_m k_m^{act} (\lambda_m)^4 (\lambda_m - \lambda_m^{min})(\lambda_m^{max} - \lambda_m) & \lambda_m^{min} \leq \lambda_m \leq \lambda_m^{max} \\ 0 & \text{otherwise} \end{cases} \tag{4.11}$$

where the SMC stretch λ_m is related to the tissue stretch by

$$\lambda_m = \frac{\lambda_{4m}}{\lambda_{Rm}} \tag{4.12}$$

and λ_{Rm} is the SMC recruitment stretch. We set $\lambda_m^{min} = 0.25$ and $\lambda_m^{max} = 2.5$. Examples of SMC stretch and active pressure curves are shown in Figure 49.

The stimuli $S(t)$ ramps up at the onset of voiding and incorporates a feedback mechanism to decrease the stimulus and when the flow rate falls below a critical value Q_{crit} ($Q_{crit} = 0.02ml/s$) at $t = t_{crit}$, i.e.

$$S(t) = \begin{cases} 1 - \frac{1}{1+(t/k_1)^4} & 0 \leq t \leq t_{crit} \\ \left(1 - \frac{1}{1+(t_{crit}/k_1)^4}\right)\left(\frac{1}{1+((t-t_{crit})/k_2)^4}\right) & t_{crit} < t \leq t_{end} \\ 0 & t > t_{end} \end{cases} \tag{4.13}$$

where $k_1 = 1$ and $k_2 = 2$ control the rate of increase and decrease of signal strength, respectively; t_{end} denotes when $Q(t) = 0$.

4.2.3 Modeling Two States of Micturition

Due to the induction of BOO, the pressure required to void the bladder increases. Initially, the SMCs cannot generate sufficient tension to achieve this pressure and urine only exits the bladder through leakage. As remodeling progresses, the SMC mass increases and the bladder recovers the capacity for voiding. As elaborated on below, the micturition model of the BOO bladder therefore has two different states (see Figure 41): *active bladder* and *leaky bladder*. The animal model initially exhibited the early phase of leaky bladder shown by overflow incontinence due to BOO-induced high urethral resistance. Then, the active bladder phase with micturition events gradually developed along with SMC hypertrophy.

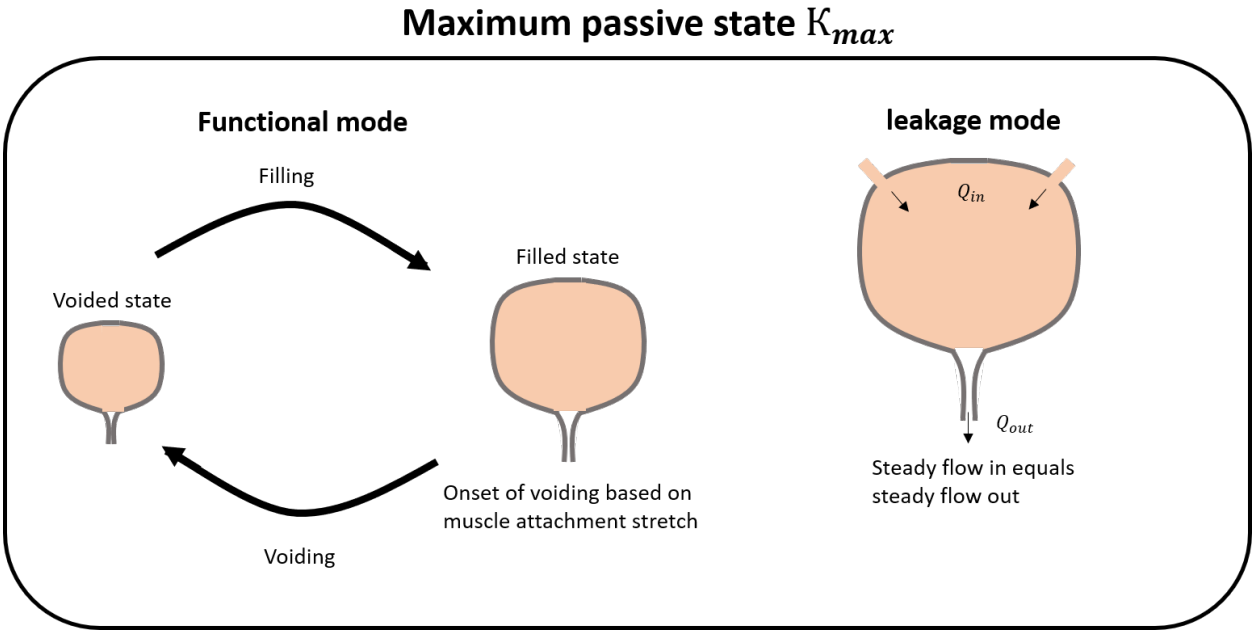

Figure 41: Schematic implication of the bladder maximum passive state under two different modes: functional mode (left) and leakage mode (right)

4.2.3.1 Active Bladder

In the active bladder state, the SMCs are able to generate sufficient wall tension to overcome the urethral outlet resistance and induce voiding. For the *in silico* model, this process is simulated through a coupling between SMC stretch and the active stress generated by the SMCs. In particular, as the bladder fills and enlarges, the nervous stimulus function $S(t)$ is triggered when the SMC stretch reaches a critical value, i.e. when $(\lambda_m = \lambda_m^{at})$. Consequently, SMC active stress increases and voiding is initiated when the internal bladder pressure (*passive + active*) exceeds the cutoff pressure (P_c) at which the urethra opens and closes. Voiding is complete when the internal pressure falls below the cutoff pressure.

The temporal dynamics of the pressure and outflow-rate of the active bladder can be computed during voiding. Following earlier works, we assume a linear relationship between voiding flow rate $Q(t)$ and bladder pressure $P(\lambda, t)$ [38, 10]:

$$Q(t) = \begin{cases} \frac{1}{\alpha}(P(\lambda,t) - P_c) & P(\lambda,t) > P_c \\ 0 & P(\lambda,t) \leq P_c \end{cases} \tag{4.14}$$

where α is the slope of the Pressure-Flow relationship and is a measure of urethral resistance. As voiding progresses, the updated volume is computed to calculate updated pressure $(P(\lambda, t))$. On completion of voiding, relevant metrics are calculated (volume voided, residual volume, voiding duration, contractile range). If the bladder cannot generate sufficient active pressure to overcome the BOO cutoff pressure P_c^{BOO} then it will continue to fill. As it enlarges, the passive pressure increases; when passive pressure exceeds the cutoff pressure, the bladder will begin to leak. A new steady state occurs when the passive pressure increases until the leaky flow rate matches the filling rate of the bladder, i.e. $Q_{out} = Q_{in}$. The passive pressure (P^{leaky}) this occurs at can be determined from eqn.4.14:

$$P^{leaky} = \alpha Q_{in} + P_c^{BOO} \tag{4.15}$$

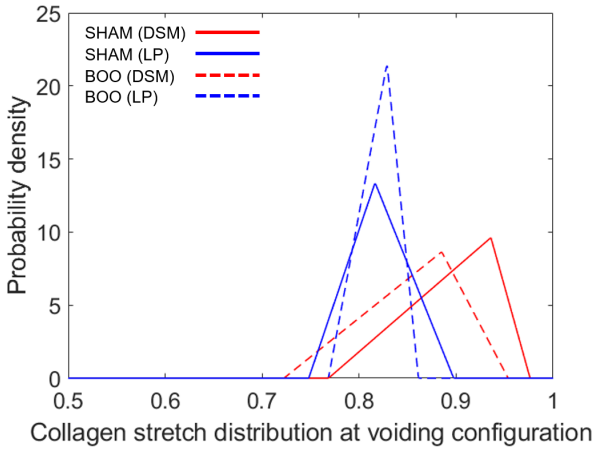

Figure 42: The average collagen stretch distribution at voiding configuration κ_V of BOO and SHAM

4.2.4 Homeostasis, Growth and Remodelling

4.2.4.1 Homeostasis

Collagen recruitment distributions of SHAM and BOO tissue samples were quantified using biaxial mechanical testing and multiphoton microscopy. The distribution of collagen stretches at the onset of voiding is calculated from recruitment stretch distributions and the *in vivo* stretch at the onset of voiding, i.e. $\lambda|_{\kappa_{max}}^{sham}$, $\lambda|_{\kappa_{max}}^{boo}$. We observed that whilst the BOO bladder's onset of voiding radius increased by around 33%, collagen stretch distributions in this configuration were similar in each layer and maximum stretches were maintained below 1 (see Figure 42). Hence we observed that collagen is configured to be a protective sheath for the SHAM bladder and remodels during outlet obstruction to maintain this mechanical role. Based on our observations, for the *in silico* model, we assume that collagen is configured with a preferential stretch distribution at the onset of voiding and this distribution is fixed during remodelling; values for the distribution (see Table 13 are based based on Figure 42)

We assume SMC configures to achieve a preferred stretch at the onset of voiding, i.e. λ_m^{at}. We further assume that the muscle stretch at the onset of voiding is configured to the left

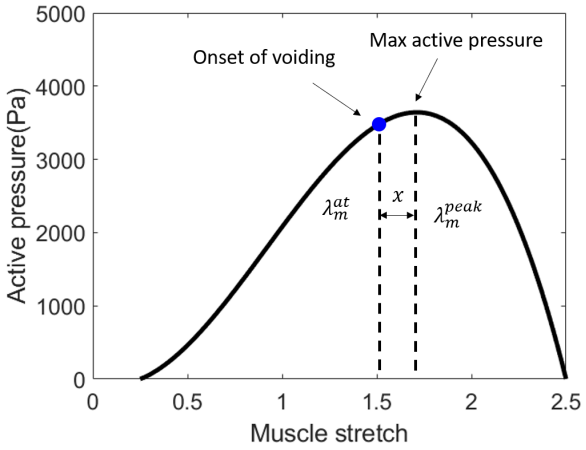

Figure 43: Schematic of active pressure vs. muscle stretch curve and configuration of muscle stretch at the onset of voiding

of the maxima of the active pressure-muscle stretch curve which occurs at an SMC stretch of λ_m^{peak}, i.e.

$$\lambda_m^{at} = \lambda_m^{peak} - x \tag{4.16}$$

where we take $x = 0.1$. The rationale for this choice is as follows: configuring to the left of the peak still enables the bladder to generate active stress to void at a larger size (if voiding is withheld), Figure 43; we don't configure too far to the left of the peak so that we can simulate a sufficient contractile voiding range.

4.2.4.2 Remodelling

We assume that constituents are configured about the maximum passive state κ_{max} during the voiding cycle, i.e. about the onset of voiding for the *active bladder* and about the steady flow state for the *leaky bladder*. We assume collagen continually remodels to maintain it's mechanical role as a protective sheath at the maximum passive state (κ_{max}). Collagen recruitment stretch distributions remodel so that the collagen stretch distribution

remodels towards the (homeostatic) attachment stretch distribution[8, 13, 78]:

$$\frac{\partial \lambda_{RLc}^{min}}{\partial \tau} = \alpha_c \frac{\lambda_{Lc}^{max}(\tau)|_{\kappa_{max}} - \lambda_{Lc}^{at,max}}{\lambda_{Lc}^{at,max}} \tag{4.17}$$

$$\frac{\partial \lambda_{RLc}^{mod}}{\partial \tau} = \alpha_c \frac{\lambda_{Lc}^{mod}(\tau)|_{\kappa_{max}} - \lambda_{Lc}^{at,mod}}{\lambda_{Lc}^{at,mod}} \tag{4.18}$$

$$\frac{\partial \lambda_{RLc}^{max}}{\partial \tau} = \alpha_c \frac{\lambda_{Lc}^{min}(\tau)|_{\kappa_{max}} - \lambda_{Lc}^{at,min}}{\lambda_{Lc}^{at,min}} \tag{4.19}$$

where the max, mode and minimum collagen fibre stretches evaluated at κ_{max} are, respectively:

$$\lambda_{Lc}^{max}|_{\kappa_{max}} = \frac{\lambda|_{\kappa_{max}}}{\lambda_{RLc}^{min}}, \qquad \lambda_{Lc}^{mod}|_{\kappa_{max}} = \frac{\lambda|_{\kappa_{max}}}{\lambda_{Rc}^{mod}}, \qquad \text{and} \qquad \lambda_{Lc}^{min}|_{\kappa_{max}} = \frac{\lambda|_{\kappa_{max}}}{\lambda_{RLc}^{max}}. \tag{4.20}$$

We hypothesise that SMCs remodel to maintain their stretch towards a homeostatic value about the onset of voiding, i.e. typical maximum passive state, κ_{max}:

$$\frac{\partial \lambda_{Rm}}{\partial \tau} = \alpha_m \frac{\lambda_m(\tau)|_{\kappa_{max}} - \lambda_m^{at}}{\lambda_m^{at}}|_{\kappa_{max}} \tag{4.21}$$

Where λ_{Rm} is the SMC recruitment stretch, λ_m^{at} is the SMC attachment stretch, α_m is a remodeling rate parameter and $\lambda_m|_{\kappa_{max}}$ is the SMC stretch at the maximum passive state, i.e. at the onset of voiding or leaky bladder.

4.2.4.3 Growth

The bladder responds to outlet obstruction with SMC hypertropy so that it can generate more force to overcome the outlet resistance and successfully void. In this study, we simulate SMC hypertrophy by evolving the SMC mass density and consider three illustrative mechanisms to drive growth. SMC hypertrophies to maintain: (i) volume voided; (ii) average voiding flow rate; (iii) contractile range. Based on the experimental observations, the total voided volume of bladder is restored at 4 weeks post-obstruction. Thus we assumed that the muscle grows to maintain the total volume voided of bladder.

$$\frac{\partial m_{smc}}{\partial \tau} = \beta_{smc} m_{smc} \left(\frac{V^0_{void} - V_{void}(\tau)}{V^0_{void}} \right) \tag{4.22}$$

where V^0_{void} is the volume voided at $\tau = 0$ (normal bladder) and $V_{void}(\tau)$ is the volume voided at time τ; β_{smc} is the growth rate parameter of muscle cells. The urethra can sense flow[14] and we assume that the the muscle grows was driven by the average flow rate of voiding sensed by urethra. Specifically,

$$\frac{\partial m_{smc}}{\partial \tau} = \beta_{smc} m_{smc} \left(\frac{Q^0_{avg} - Q_{avg}(\tau)}{Q^0_{avg}} \right) \tag{4.23}$$

Where $Q_{avg}(0)$ is the average voiding flow rate at $t = 0$ (normal bladder) and $Q_{avg}(\tau)$ is the average voiding flow rate at time τ. We assumed that the muscle grows to maintain the contraction range λ_{m-cyc} during voiding, which is defined as the difference between the muscle stretch at the filled state λ^F_m and the muscle stretch at the voided state λ^V_m, i.e.

$$\frac{\partial m_{smc}}{\partial \tau} = \beta_{smc} m_{smc} \left(\frac{\lambda^0_{m-cyc} - \lambda_{m-cyc}(\tau)}{\lambda^0_{m-cyc}} \right) \tag{4.24}$$

where $\lambda_{m-cyc} = \lambda^F_m - \lambda^V_m$ and, λ^0_{m-cyc} and $\lambda_{m-cyc}(\tau)$, are the muscle contractile ranges during voiding at $\tau = 0$ and τ, respectively.

Hypertropy of SMC will lead to a thickening of the bladder wall. The evolving wall thickness can be inferred from initial constituent volume fractions and constituent mass-densities; this allows for comparison with experimental observations. For the geometrical

model of the bladder considered (spherical membrane), the wall thickness in the voiding configuration, $h_g(t)$, is

$$h_g(t) = H_0 \hat{v}(t) \frac{1}{\lambda(t)^2 \mid_{\kappa_{max}}} \tag{4.25}$$

where $\lambda_{onset}(t)$ denotes the stretch at onset of voiding and the normalised tissue volume $\hat{v}(t)$ is

$$\hat{v}(t) = f_e^0 m_e(t) + f_c^0 m_c(t) + f_m^0 m_m(t), \tag{4.26}$$

and f_e^0, f_c^0, f_m^0 are initial volume fractions of elastin, collagen and SMCs. We assumed that at $t = 0$, the volume fractions of elastin, collagen, and SMCs are 10%, 30% and 60%, respectively.

4.2.5 Computational Implementation

4.2.5.1 Spherical Membrane Model of Bladder

In this work, we apply the general constitutive model above to the case of quasi-static inflation of an incompressible, two-layered nonlinear elastic, spherical membrane. Each wall component is idealized as having an isotropic contribution. In the absence of external body forces, the displacement field must satisfy $\nabla \cdot \underline{\sigma} = 0$ where, as previously noted, $\underline{\sigma}$ is the Cauchy stress tensor.

During the deformation, the spherical membrane with unloaded radius R_0 is inflated to radius R due to an applied transmural pressure P. The corresponding kinematics in spherical coordinates $(\underline{e}_r, \underline{e}_\phi, \underline{e}_\theta)$ are:

$$\underline{F} = \text{Diag}[1/\lambda^2, \lambda, \lambda], \qquad \underline{B} = \text{Diag}[1/\lambda^4, \lambda^2, \lambda^2], \tag{4.27}$$

where, λ denotes the tissue stretch (R/R_0), with reference to the unloaded state κ_0. Due to the symmetry of the loading conditions and the symmetry of the material response, $\sigma_{\phi\phi} = \sigma_{\theta\theta}$, which we simply denote as σ. Employing the governing equation for mechanical equilibrium of the membrane and boundary conditions involving the transmural pressure, it follows that

$$P = \frac{2H_0}{R_0 \lambda^3} \left(r_{LP}^H \sigma_{c,LP} + r_{DSM}^H (\sigma_e + \sigma_{c,DSM} + \sigma_m^{act}) + r_{ADV}^H \sigma_{c,ADV} \right) \tag{4.28}$$

where r_L^H denotes the ratio of the thickness of layer L to total wall thickness H_0 where $L = LP, DSM, ADV$. σ_e denotes the Cauchy stress of elastin, σ_{c_L} denotes the Cauchy stress of collagen in layer L and σ_m^{act} denotes the active Cauchy stress of smooth muscle; H_0 and R_0 denotes the thickness and radius at the unloaded state, and λ denotes the tissue stretch with reference to the unloaded state κ_0. It should be recalled, that for this study, each contribution is idealized as isotropic.

4.2.5.2 Set-up Initial Configuration: Geometry; Material Parameters; G&R Parameter

Geometric, mechanical, urodynamic features of the *in silico* model are informed from experimental measurements (see Tables 10, 11 and 12). At the onset of voiding, the bladder has a radius of 5.8 mm and a wall thickness of 0.21mm. The passive pressure within the bladder at the onset of voiding is 300Pa and the pressure increases to 3800Pa as the SMC generates active force. Voiding takes 12s during which 0.8ml is voided leaving a residual volume of 0.02ml. The modelling steps to set-up the *in silico* model of the the healthy bladder are as follows:

- The radii of the unloaded, voided and filled states, R_0, R_V and R_F were computed by assuming the bladder to be a hollow sphere. The unloaded spherical radius is $R_0 = (\frac{3V_0}{4\pi})^{1/3}$ where V_0 is the volume of the unloaded bladder which is assumed to be an ellipsoid. Similarly, the bladder radii at voided state κ_v and filled state κ_F (Figure 25) were calculated by approximating the bladder as a spherical membrane, i.e. $R_F = (\frac{3V_F}{4\pi})^{1/3}$ and $R_v = (\frac{3V_v}{4\pi})^{1/3}$ where V_F and V_v are the filled and voided volumes, respectively.
- The tissue stretches at filled and voided configurations are $\lambda_F = R_F/R_0$ and $\lambda_V = R_V/R_0$, respectively.
- The three recruitment parameters of the collagen triangular recruitment distribution are determined from the collagen attachment stretch distribution parameters (see Figure 44 and Table 13) and the tissue stretch at the filled state (λ_F).
- The initial value of the muscle recruitment stretch is determined by dividing the tissue stretch at filled state λ_F by the muscle attachment stretch λ_m^{at}, i.e. $\lambda_M^R = \lambda_F/\lambda_m^{at}$.

Table 13: Default model parameters.

Parameter	Meaning	Value
k_e	elastin material parameter	$1.15e^3$ Pa
$k_{LP,c}$	collagen material parameters	$6.4e^6$ Pa
$k_{DSM,c}$	layer L (L=LP,DSM,ADV)	$1.6e^6$ Pa
$k_{ADV,c}$		$6.4e^6$ Pa
λ^{att}_{LPc}	min/mode/max	0.75, 0.775, 0.9
λ^{att}_{DSMc}	collagen attachment stretches	0.775, 0.95, 0.975
λ^{att}_{ADVc}	layer L (L=LP,DSM,ADV)	0.6, 0.7, 0.8
k^{act}_m	SMC active modulus	6212 Pa
λ^{min}_m	SMC active stress parameter	0.25
λ^{max}_m	SMC active stress parameter	2.5
λ^{att}_m	SMC attachment stretch	1.6
P^{SHAM}_c	cutoff pressure SHAM	380 Pa
P^{BOO}_c	cutoff pressure BOO	6300 Pa
α_{SHAM}	urethral resistance SHAM	28570Pa/(ml/s)
α_{BOO}	urethral resistance BOO	52630Pa/(ml/s)
Q_{in}	bladder filling rate	$0.8ml$/day
α_c	collagen remodeling rate	7.5
α_m	muscle remodeling rate	7.5
β_m	muscle growth rate	4

- We observed that collagen was not bearing load at the onset of voiding and hence acts as a protective-sheath against overdistension. Therefore k_E was computed based on the force balance at the initial maximum passive state (R_F) and assumption that only elastin is load bearing. Specifically $K_E = P_{max}^{passive} \frac{R_0 \lambda_F^7}{2H_0 r_{DSM}^H (\lambda_F^6 - 1)}$.
- Collagen material parameters ($k_{LP,c}, k_{DSM,c}, k_{ADV,c}$) are determined by fitting the passive model to the mechanical loading data.
- In the pressure-flow experiment, we measured the maximum passive filling pressure $P_{max}^{passive}$ and maximum voiding pressure $P_{max}^{voiding}$. The difference between these two is the maximum active pressure P_{max}^{act}. From the active force balance equation, we can determined k_m^{act} analytically from $P_{max}^{act} = k_m^{act} \frac{2H_0 r_{DSM}^H}{R_0 (\lambda_m^r \lambda_m^{at})^3} (\lambda_m^{at})^4 (\lambda_m^{at} - \lambda_m^{min})(\lambda_m^{max} - \lambda_m^{at})$.
- The urethral resistance parameters, P_C and P_C^{BOO}, are determined as follows. At the tissue voided stretch λ_V, the flow-rate $Q(t) = 0$. Hence from eqn.4.14, we obtain $P_c = P^{act}(\lambda_m(\lambda_V, \lambda_M^R)) - P_C = 0$ where P^{act} is the active pressure (and similarly for P_C^{BOO}). The slope of urethral resistance relationship, α, is then determined by matching the voiding duration of the SHAM bladder; we assume α is a constant and does not adapt during BOO remodelling.
- The collagen remodeling rate α_c and muscle growth rate β_m are numerically determined so that the final void radius matches the experimental void radius and smooth muscle hypertrophy stabilises after around 2 weeks.

The model is implemented into Matlab and uses two timescales: a longer time-scale τ (days/weeks) for G&R; a short-time scale t (seconds) for computation of urodynamics during voiding; parameter values are detailed in Table.13.

The bladder model is subject to a constant inflow rate. To facilitate visual illustration of the model behaviour, we set the inflow to be 0.8ml/day so that the healthy bladder fills and voids once per day. At each time step, as the bladder fills, the updated volume (and radius) of the bladder is computed. The bladder continues to fill until either: voiding is triggered or of it is unable to void, it leaks. If voiding is triggered, urodynamic metrics are computed, the bladder is emptied and the cycle of filling begins again.

- For $\tau < 0$, the bladder can functionally void and is in a homeostatic state.

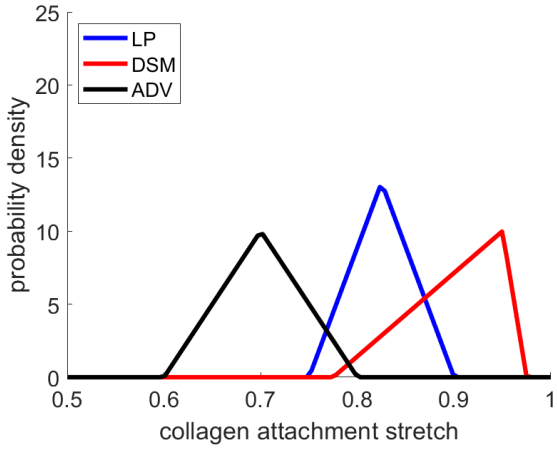

Figure 44: Collagen attachment stretch distributions in the lamina propria, detrusor and adventitial layers.

- To simulate the creation of outlet obstruction, parameters of the pressure-flow relationship (see eqn. 4.14) are instantaneously changed at $\tau = 0$: the cutoff pressure is increased from P_c^{SHAM} to P_c^{BOO} and the resistance parameter is increased from α_{SHAM} to α_{BOO}.
- Throughout the simulation, maximum stretches of all constituents are computed during voiding cycle (or in the leaky state). These are used to drive remodelling of collagen and SMC recruitment stretches to maintain a homeostatic state about the voiding configuration (see eqns. 4.17, 4.19, 4.18 and 4.21). Voiding metrics are used to control SMC growth using eqns. 4.22 or 4.23 or 4.24
- Growth and remodelling continues until a new homeostasis is achieved and voiding functionality of bladder restored.

4.2.5.3 Simulations

In Section 4.3, we illustrate the *in silico* model of the bladder and its adaptive response to BOO. We then investigate how the SMC growth rate parameter influences model behaviour and examine several mechanisms to drive SMC growth. Lastly, we compare model predictions with experiment at 4 weeks post-BOO.

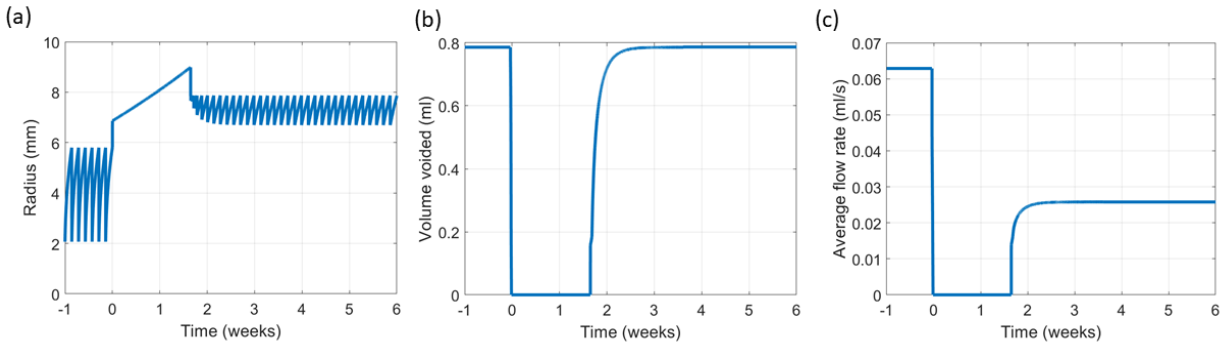

Figure 45: Bladder adaption from pre-obstruction ($t < 0$) to post-obstruction ($t > 0$). (a) Evolution of radius with illustrative filling and voiding cycles. Temporal evolution of (b) volume voided and (c) average flow rate.

4.3 Results

Figure 45 overviews the voiding behaviour of the *in silico* bladder, prior to, and in response to outlet obstruction. Note that in this illustrative simulation, the bladder is subject a constant inflow rate of 0.8ml/day and consequently, during the pre-obstruction period ($t < 0$), the healthy bladder voids once per day: the radius varies from around 2mm to 6mm during voiding cycles (see Figure 45(a)); voiding of 0.8ml/s takes 12 seconds; the peak flow rate is 0.12 ml/s and the average flow rate is 0.06 ml/s. Following obstruction, the bladder is unable to actively void and consequently continues to fill and enlarge. The increase in size is accompanied by a significant increase in the passive pressure as collagen is recruited to load bearing. When the passive pressure becomes sufficiently large, it overcomes the outlet resistance and the bladder begins to leak (*leaky bladder*). The passive pressure continues to increase until the outflow rate matches the filling rate.

During the *leaky bladder* phase, the SMC does not generate sufficient force to contract the bladder and thus the (active) volume voided is zero (see Figure 45b). Between $0 < t < 1.5$ weeks, the leaky bladder increases in size to around 8.5mm as the collagen (which acts as a protective sheath for the healthy bladder) remodels. Once the bladder is able to void again,

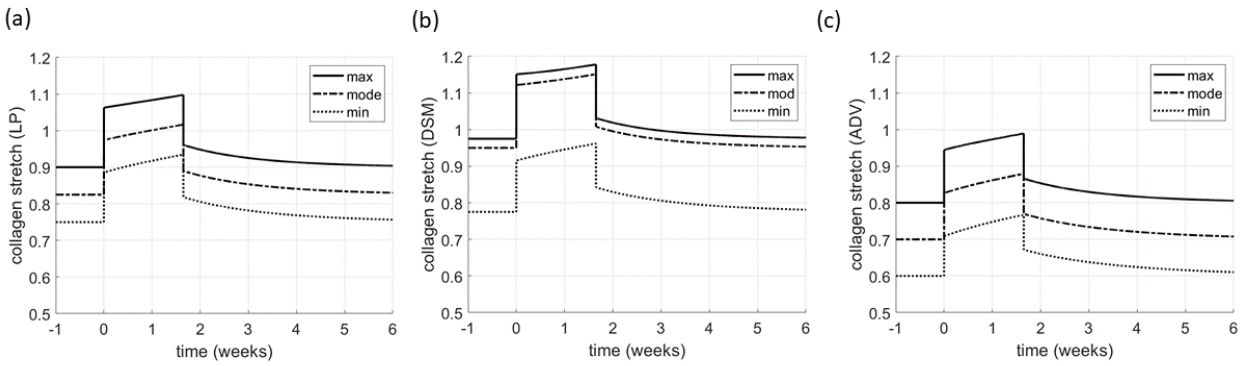

Figure 46: Evolution of collagen stretch distribution (maximum, mode and minimum) for individual layers: (a) lamina propria (b) detrusor and (c) adventitia.

the maximum stretches of collagen during the voiding cycle reduce below 1 and collagen reverts to being a protective sheath (see Figure 46). Note that as the bladder enlarges, the collagen recruitment stretch distributions remodel (see Figure 47) to maintain the collagen stretch distribution towards the attachment stretch distribution at the onset of voiding.

Hypertropy of SMC occurs rapidly during the *leaky bladder* phase (Figure 48). In the model, functional voiding is restored when SMC can generate sufficient force to generate a contraction of the bladder so that the voided SMC stretch is less than the homeostatic SMC voiding stretch ($\lambda_m^{att} = 1.6$). After around 1.5 weeks, the bladder starts to (actively) void again with a small volume and high frequency. As SMC hypertropy increases, the contractile range of SMC during voiding increases and thus the volume voided increases whilst the voiding frequency decreases. After 3 weeks, the total volume voided is fully restored but the average flow rate is only about 50% of the normal bladder (see Figure 45b,c). Interestingly, due to an increase in size, the post-obstructed bladder can void the same amount of urine as the pre-obstructed bladder with a smaller range of contraction (see Figs. 45a and 49).

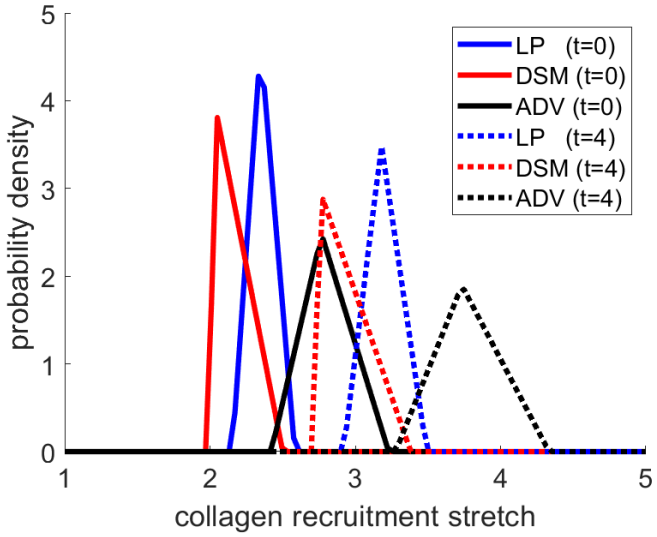

Figure 47: Recruitment stretch distributions in the layers of the bladder for the SHAM bladder ($(t = 0)$ and following G&R in response to BOO.

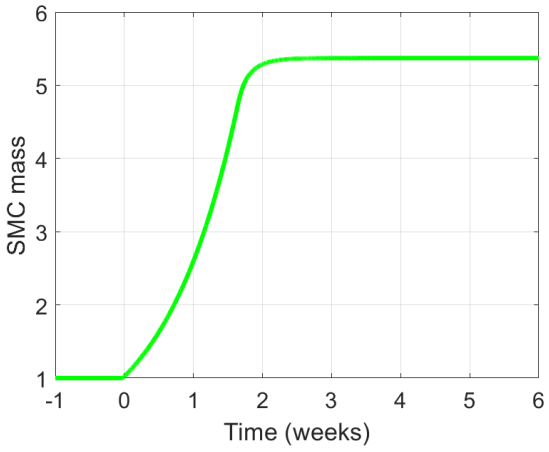

Figure 48: The change of SMC mass during BOO growth and remodeling

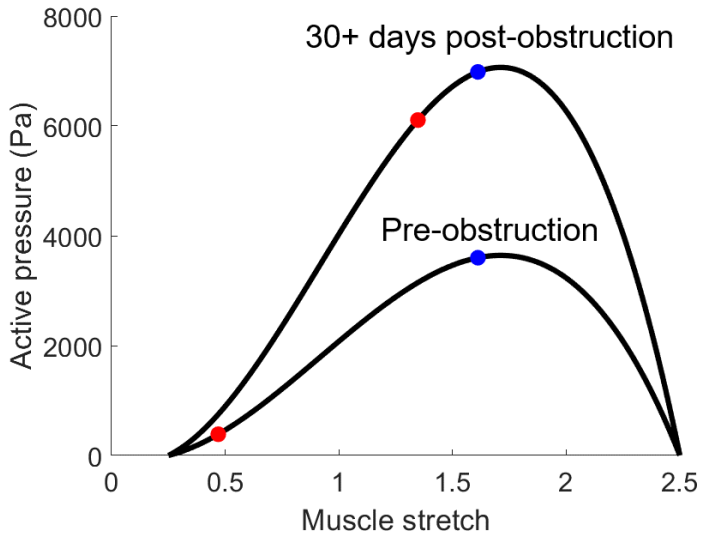

Figure 49: The relation between muscle stretch and active pressure for pre and 30+ days post obstruction. The blue dots showed the onset of voiding and red dots showed the end of voiding

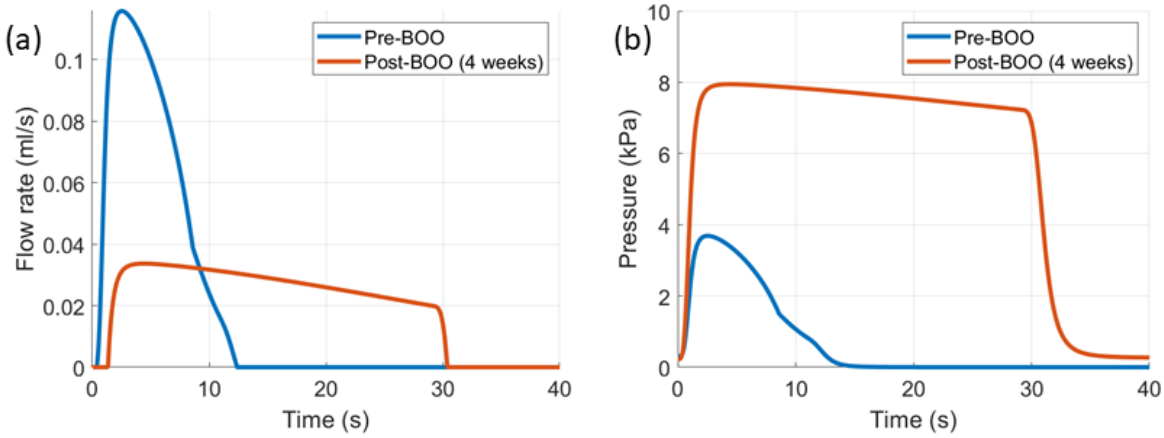

Figure 50: The urodynamic curves of selected time points including (a) time vs. flow rate curve and (b) time vs. pressure curve

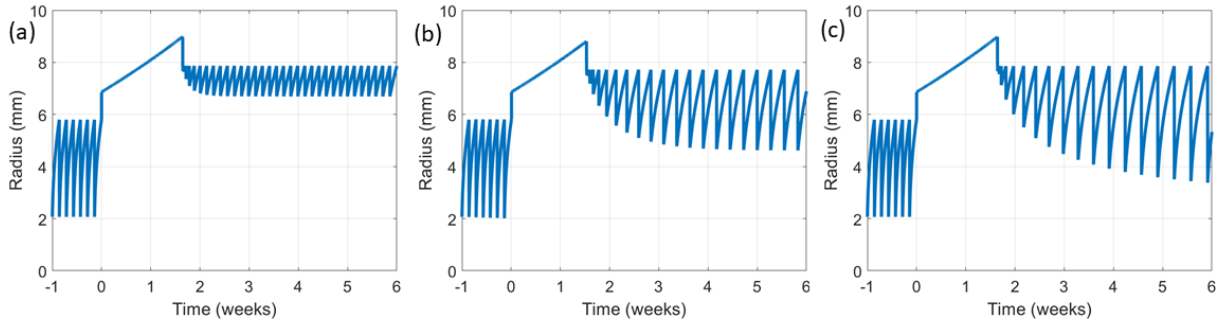

Figure 51: The simulated time as a function of radius with different hypothesis of SMC growth (a) SMC growth driven by voided volume driven (b) SMC growth driven by average flow rate (c) SMC growth driven by SMC contraction range

4.3.1 Bladder Urodynamics Pre and Post Obstruction

From Figure 50a, it can be seen that the maximum flow rate of the bladder decreases by approximately 75% and the voiding duration more than doubles. The maximum voiding pressure doubles during voiding for the BOO bladder (see Figure 50b) due to the SMC hypertrophy.

4.3.2 Comparison of Different Growth Hypotheses

Three illustrate mechanisms to drive SMC hypertrophy were investigated, restoration of: volume voided; 2. average voiding flow-rate; 3. contractile range. For all cases, the bladder maximum radius was increase by 33 % (see Figure 51) following obstruction. It can be seen that if the bladder adapts to restore average flow rate or contractile range then the volume voided increases (Figure 52(b)). However, significant increases in SMC mass are required to maintain the contractile range (Figure 52(a)) and it takes a longer time to achieve homeostasis.

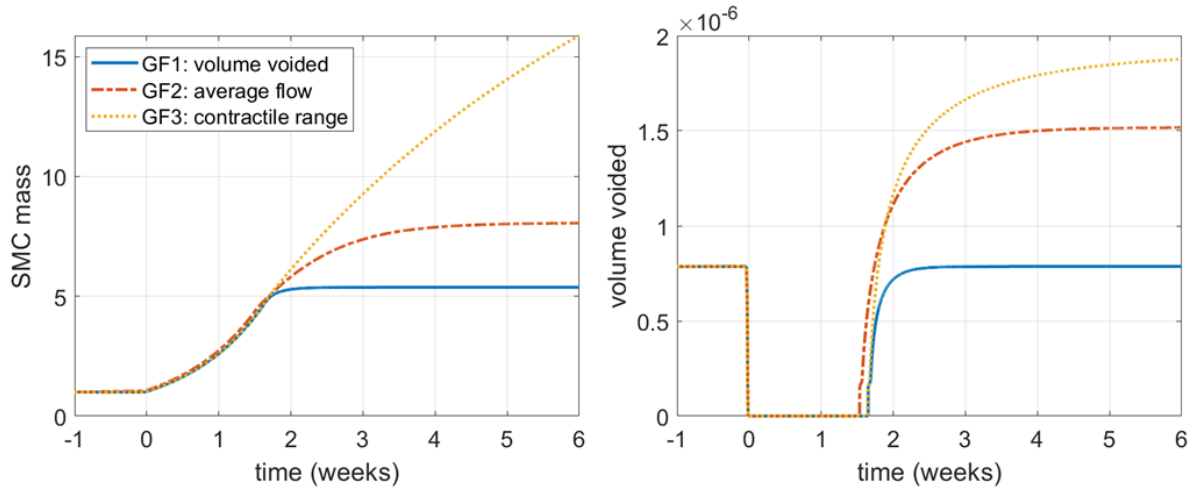

Figure 52: The time dependent change of (a) SMC mass and (b) volume voided using different SMC growth evolution functions: GF1 (blue) - SMC hypertrophy acts to restore volume voided; GF2 - (red) SMC hypertrophy acts to restore average flow rate; GF3 - (yellow) SMC hypertrophy acts to restore contractile range

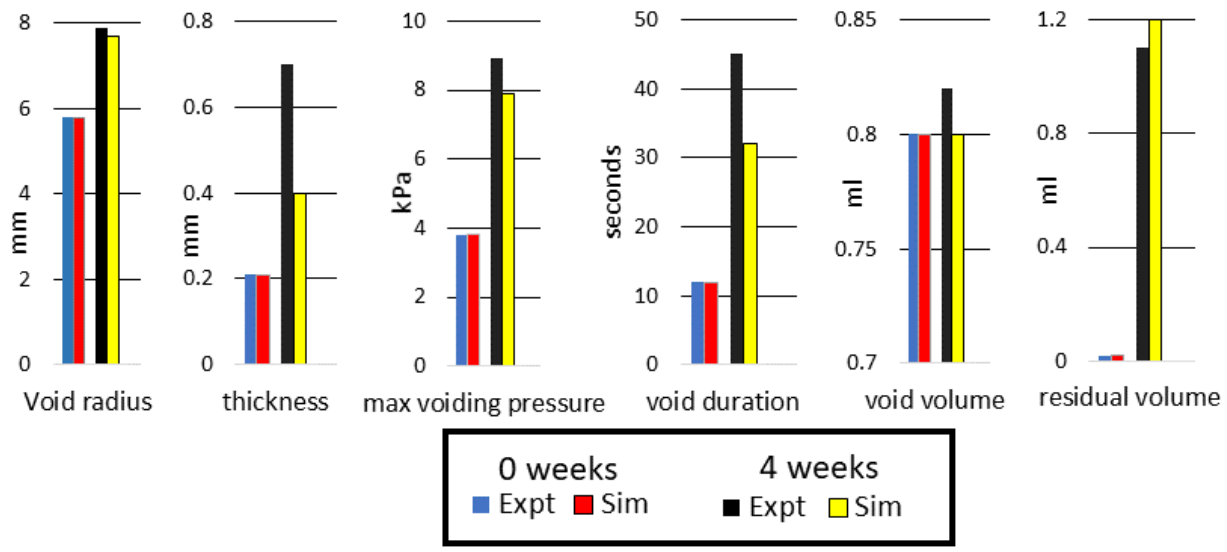

Figure 53: Comparison between *in silico* and experimental model bladder parameters at 4 weeks post-BOO.

4.3.3 Comparison Between Simulation and Experiment

We conclude the results section by comparing predictions of the *in silico* bladder model with experimental observations. Figure 54 illustrates the rightward shift of the stress-stretch curves for (a) the experimental model and (b) the *in silico* model. Note for comparison with the experimental model, the BOO mechanical response has been plotted relative to the SHAM reference configuration. Figure 53 depicts relevant bladder metrics pre-BOO and 4 weeks post-BOO. It can be seen that there is consistency between model predictions and experiment observations, i.e. the *in silico* bladder: enlarges in size and the wall thickens; voiding volume is conserved whilst the residual volume increases; voiding duration increases; a reduction in the passive filling pressure occurs whilst the maximum void pressure approximately doubles. In fact, quantitative consistency is achieved for most quantities; however, the *in silico model* underestimates the increase in wall thickness and void duration.

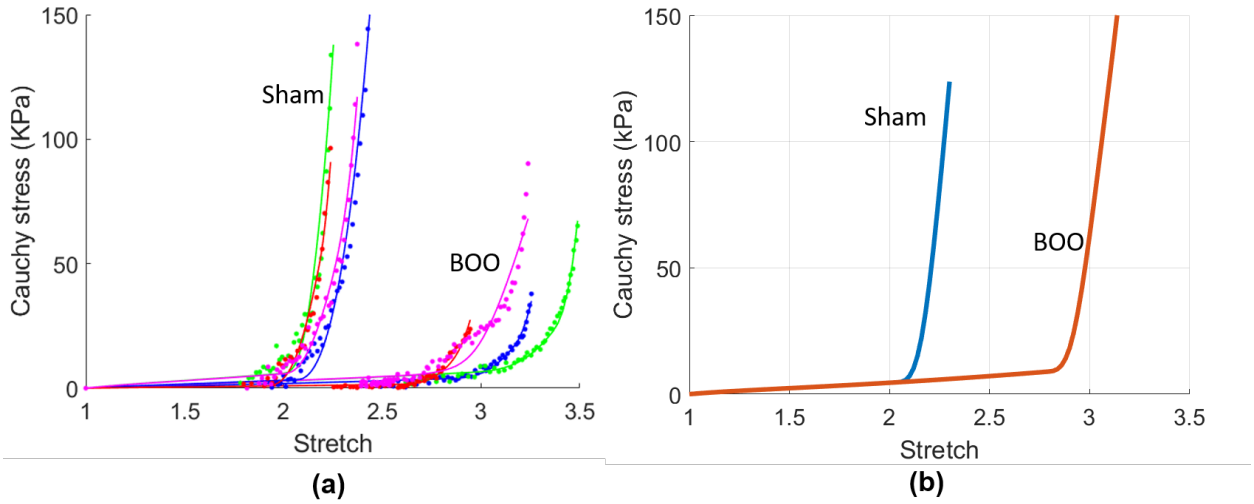

Figure 54: The comparison between (a) experimentally measured mechanical loading curves of SHAM (n=4) and 4 week BOO (n=4) and (b) simulated passive mechanical loading curves of SHAM and 4 week BOO. Note for the comparison, the experimentally measured stretch of BOO bladder is defined relative to the unloaded state κ_0 of SHAM bladder by multiplying the stretch by the ratio of unloaded radii ($R_{0,BOO}/R_{0,Sham}$).

4.4 Discussion

We have presented the first G&R model of the urinary bladder and used it to simulate the response of the bladder to outlet obstruction. The model provides a mechanistic understanding of how the bladder wall adapts in response to BOO to restore voiding functionality. An integrative *in-vivo in-vitro in-silico* modelling approach underpins the work and enables calibration of the healthy bladder model and informs remodelling assumptions. Consistent with experimental observations in a rat model of BOO, the model predicts that following initiation of BOO, the bladder enters a leaky state after which hypertrophy of SMC restores the ability to void. Moreover, the model correctly predicts that whilst volume voiding is restored by this G&R response, residual volume increases, the average voiding flow rate decreases and the voiding duration increases. Although the model has good consistency with experiment, it has several limitation, that are discussed below.

Experimental data confirms the bladder undergoes three stages of remodelling in response to BOO: an initial *hypertrophy* phase, followed by a *compensation* phase, and finally, a *decompensation* phase [32]. The hypertrophy stage consists of SMC growth accompanied by angiogenesis to meet the increased metabolic demands of the tissue. During the compensation stage, the bladder maintains effective voiding function but is subject to cyclic ischaemia-reperfusion injury; this leads leads to matrix accumulation (fibrosis) and also neuronal loss [54] that is accompanied diminished SMC contractility. Finally, in the decompensation stage, SMC atrophy occurs leading to loss of bladder functionality. In the present work, we only model the hypertrophy and early compensation stages of BOO- without ischaemic damage. Our integrative *in-vivo in-vitro in-silico* modelling approach provides foundations for developing a more complete representation of all stages of BOO. We envisage such a model may assist in designing/evaluating pharmacological or surgical interventional strategies for clinical management of the disease.

While numerous studies have investigated the relationship between mechanical stimuli and SMC remodeling in arteries as well as the associated set points for homeostasis, very little is known about this type of coupling in the bladder wall. Here, we used the G&R model to investigate hypotheses linking SMC growth to bladder biometrics (volume voided, average

voiding flow rate, contractile range). The first hypothesis we investigated is that the growth of SMC is driven by volume voided. This is based on our experimental observations that volume voided was restored following hypertrophy. Interestingly, others have also observed the bladder to increase in size with higher residual volume whilst maintaining volume voided [62]. However, whilst it is known that mechanical stress can activate signals that mediate bladder wall hypertrophy, the mechanobiological mechanisms that would enable the bladder to sense how much volume it has voided (to drive SMC growth) remain an open question. We also evaluated the hypotheses that SMC growth evolves to restore either average voiding flow rate or SMC contractile range. However, both these hypotheses led to larger increases in volume voided than observed in experiment. We therefore enlisted the first hypothesis for much of the present work. Nevertheless, we conjecture that flow or SMC stretch sensors may be relevant for adaption in non-pathological conditions, e.g. bladder enlargement during development.

Consistent with experiments, the in silico bladder was unable to void following the increase in outlet resistance, resulting in overflow incontinence after which voiding was recovered. Simulations with the G&R model enabled a mechanistic understanding of how this recovery was achieved. Imposition of BOO stimulates rapid SMC hypertrophy. In time, SMC growth is sufficient to generate adequate intravesical pressures to overcome the increased outlet resistance. However, initially, the remodeled bladder voids smaller volumes at higher frequency, compared with the normal bladder. Subsequently, the bladder transitions to the compensated phase as smooth muscle growth stabilises in response to recovery of voiding function; by design, this model restored volume voided. Consistent with experiments, the model predicted increased void duration following imposition of BOO. However, the predicted increase in void duration was greater than in experiments: 12s to 32s in *in silico* model whilst in the rat model it increased from 12s to 45s. This difference may be attributed to the modelling idealization that neither the stimulus function $S(t)$ nor the functional form of the active stress-stretch relationship are changed in response to BOO. Experimental guidance is needed to gain greater insight into the evolving functionality of SMC so the model can be sophisticated to more accurately simulate the bladder's evolving structural-functional relationship in response to BOO.

We modelled the bladder as a 1D non-linear elastic incompressible, homogeneous spherical membrane. However, the real bladder is not spherical and has spatially heterogenous material properties[55, 81]. Future developments of the model will build on existing computational growth models that account for anatomical geometries[78]; anisotropic volumetric growth [41]; and incorporation of regulatory fibrotic pathways [8]. Consideration of the molecular aspects of the remodelling, (for example, those associated with ischaemia) during the compensation, decompensation stages of BOO will provide insights on the reversibility of pathological changes associated with BOO.

The clinical diagnosis of BOO in the context of a non-neurogenic history, involves taking a detailed urological history and assessing the lower urinary tract symptoms including storage, voiding and post-voiding symptoms. A variety of symptom score questionnaires are available [37] including the International Prostate Symptom Score, the International Consultation on Incontinence questionnaire, and the Danish Prostate Symptom Score. There is strong evidence that a validated symptom score questionnaire should be used. More generally, the mainstay of assessment of lower urinary tract symptoms (LUTS) is the use of a bladder diary to assess frequency of voiding and the volumes of urine produced, ideally recorded over a consecutive three-day period. Following a clinical examination and analysis of the urine, the use of a blood test to exclude cancer (prostate specific antigen), a post-voiding residual to check that the bladder is emptying to completion and where appropriate a flow test to assess the flow of urine from the bladder through the urethra. In this work, we used our silico model to understand the cause of changes to clinical parameters such as residual volume and voided volume during the G&R response to BOO. In the future, simulations of this kind could be extended to other types of data available in clinical evaluations in order to more directly impact clinical practice.

The animal model of BOO induced by partial urethral ligation has most commonly been used to investigate the pathophysiology of male LUTS associated with BOO resulted from BPH. However, the majority of previous basic research studies on BOO have utilized female

animals. Therefore, this project used male rats to produce the BOO condition underlying male LUTS [92]. A recent study also reported that this male BOO model exhibits the early hypertrophy-compensation phase followed by the later decompensation phase of bladder dysfunction, similar to those observed in human BPH/BOO[73].

Animal models may also provide the critical data needed to overcome limitations in current diagnosis and treatment practices. For example, a pressure flow analysis is the conventional approach for diagnosing and defining the severity of BOO in patients who have a complex situations such as failure to respond to initial therapy, existence of significant post-voiding bladder residual, or prior to surgery. Whilst this test has been considered the "gold standard" evaluation for BOO and is used as a predictor of outcome to any surgical intervention to relieve the outlet obstruction, recent work in a randomised study looking at the role of urodynamics prior to surgery raised concerns over this previously widely held opinion[9]. We conjecture that a more mechanistic understanding of the relationship between the urodynamic data and progressive changes to the bladder wall during the three stages of BOO pathology is essential for addressing these limitations. Such an understanding requires a modelling approach of the kind developed here that integrates a model of filling/voiding with a longer time scale G&R model. Moreover, we envisage future work that leverages the *in vivo in vitro in silico* approach introduced here will enable the design of new diagnostic tools for assessing bladder dysfunction and provide guidance on developing new treatments.

4.5 Conclusion

We present a novel model for the bladder's adaptive G&R response to outlet obstruction. Predictions of the model were consistent with *in vivo* experiments of bladder outlet obstruction. This work is an important step towards the development of patient specific *in silico* models of the bladder that can predict changes to bladder functionality and hence guide the selection and timing of patient treatment. We envisage these models can be leveraged in the future so clinicians can make more effective use of diagnostic data and researchers can design new pharmacological and surgical interventions.

Bibliography

[1] *I.C. Society, ICS Standards 2020-2021.* 2021.

[2] P. Abrams, L. Cardozo, M. Fall, D. Griffiths, P. Rosier, U. Ulmsten, P. van Kerrebroeck, A. Victor, and A. Wein. The standardisation of terminology of lower urinary tract function: Report from the standardisation sub-committee of the international continence society. *Neurourology and Urodynamics*, 21(2):167–178, 2002.

[3] K.J. Aitken and D.J. Bägli. The bladder extracellular matrix. Part II: regenerative applications. *Nat. Rev. Urol.*, 6(11):612–621, 2009.

[4] R.S. Alexander. Mechanical properties of urinary bladder. *Am. J. Physiol.*, 220(5):1413–1421, 1971.

[5] A. Alwaal, S. D. Blaschko, J. W. McAninch, and B. N. Breyer. Epidemiology of urethral strictures. *Translational andrology and urology*, 3(2):209, 2019.

[6] K.E. Andersson and K.D. McCloskey. Lamina propria: The functional center of the bladder? *Neurourol. Urodyn.*, 33(1):9–16, 2014.

[7] K.E. Andersson and A.J. Wein. Pharmacologic management of lower urinary tract storage and emptying failure. In Alan J Wein, Louis R. Kavoussi, Alan W. Partin, and Craig A. Peters, editors, *Campbell -Walsh Urol. 11th Ed.*, chapter Pharmacolo, pages 1836–1874. Elsevier, Philadelphia, PA, 10th editi edition, 2011.

[8] P. Aparício, M.S. Thompson, and P.N. Watton. A novel chemo-mechano-biological model of arterial tissue growth and remodelling. *Journal of Biomechanics*, 49:2321–2330, 2016.

[9] K. Bailey, P. Abrams, P. S. Blair, C. Chapple, C. Glazener, J. Horwood, J. A. Lane, J. McGrath, S. Noble, R. Pickard, G. Taylor, G. J. Young, M. J. Drake, and A. L. Lewis. Urodynamics for prostate surgery trial; randomised evaluation of assessment methods (upstream) for diagnosis and management of bladder outlet obstruction in men: study protocol for a randomised controlled trial. *Trials*, 16:567, 2015.

[10] C.P. Bates, E.P. Arnold, and D.J. Griffiths. The Nature of the Abnormality in Bladder Neck Obstruction. *British Journal of Urology*, 47:651–656, 1975.

[11] M.F. Beatty. Topics in finite elasticity: Hyperelasticity of rubber, elastomers, and biological tissues-with examples. *Appl. Mech. Rev.*, 40:1699–1734, 1987.

[12] A.J.Van Beek. *A finite element model of the urinary bladder.* 1997.

[13] P. Bhogal, G. Pederzani, A. Grytsan, Y. Loh, P. A. Brouwer, T. Andersson, N. Gundiah, A. M. Robertson, P. N. Watton, and M. Söderman. The unexplained success of stentplasty vasospasm treatment : Insights using mechanistic mathematical modeling. *Clinical Neuroradiology*, 29:763–774, 2019.

[14] L.A. Birder, W. Stefan, J. Gillespie, and J.J. Wyndaele. Urethral sensation: basic mechanisms and clinical expressions. *International Journal of Urology*, 21:13–16, 2014.

[15] M.A Borsdorf, A. Tomalka, N. Stutzig, M. Morales-Orcajo, E.and Böl, and T. Siebert. Locational and directional dependencies of smooth muscle properties in pig urinary bladder. *Frontiers in physiology*, 10:63, 2019.

[16] S L Chang, P S Howard, H P Koo, and E J Macarak. Role of type III collagen in bladder filling. *Neurourol. Urodyn.*, 17(2):135–45, 1998.

[17] S.L. Chang, J.S. Chung, M.K. Yeung, P.S. Howard, and E.J. Macarak. Roles of the lamina propria and the detrusor in tension transfer during bladder filling. *Scandinavian journal of urology and nephrology. Supplementum*, 201:38–45, 1999.

[18] H Chen. *Intracranial aneurysm disease: novel modelling of inception and the microstructural adaption of collagen fabric.* PhD thesis, Department of Engineering Science, University of Oxford, 2014.

[19] J. Chen, B.A. Drzewiecki, W.D. Merryman, and J.C. Pope. Murine bladder wall biomechanics following partial bladder obstruction. *J. Biomech.*, 46(15):2752–2755, 2013.

[20] F. Cheng, L. A. Birder, F. A. Kullmann, J. Hornsby, P. N. Watton, S Watkins, and M. Robertson A. M Thompson. Layer-dependent role of collagen recruitment during loading of the rat bladder wall. *Biomechanics and modeling in mechanobiology*, 17:403–417, 2018.

[21] F. Cheng, A. M. Robertson, L. Birder, F. Kullmann, J. Hornsby, P. Watton, and S Watkins. An experimental approach for understanding the layer dependent role of collagen recruitment during loading in the rat bladder wall. *Proceedings of the 5th*

International Conference on Computational Mathematical Biomedical Engineering, pages 396–399, 2017.

[22] F. Cheng, P.N. Watton, and et al. An integrative biomechanics-micturition model of the urinary bladder. *to be submitted*, 2021.

[23] M. Coldinq-Jørqensen and K. Steven. A model of the mechanics of smooth muscle reservoirs applied to the intestinal bladder. *Neurourology and Urodynamics*, 12:59–79, 1993.

[24] K.S. Coyne, A.J. Wein, A. Tubaro, C.C. Sexton, C.L. Thompson, Z.S. Kopp, and L.P. Aiyer. The burden of lower urinary tract symptoms: Evaluating the effect of LUTS on health-related quality of life, anxiety and depression. *BJU International*, 103:4–11, 2009.

[25] M.S. Damaser and S.L. Lehman. Two mathematical models explain the variation in cystometrograms of obstructed urinary bladders. *Journal of biomechanics*, 29(12):1615–1619, 1996.

[26] K.B. Egan. The epidemiology of benign prostatic hyperplasia associated with lower urinary tract symptoms: prevalence and incident rates. *Urologic Clinics*, 43(3):289–297, 2016.

[27] D H Ewalt, P S Howard, B Blyth, H M Snyder, J W Duckett, R M Levin, and E J Macarak. Is lamina propria matrix responsible for normal bladder compliance? *J. Urol.*, 148(2 Pt 2):544–9, 1992.

[28] W. Fletcher. A Computer Simulation of Micturition. pages 1–36, 2005.

[29] William Fletcher, F. T. Smith, and C. Fry. A computer simulation of micturition, 2005.

[30] Y.C. Fung. Elasticity of soft tissues in simple elongation. *The American journal of physiology*, 213:1532–1544, 1967.

[31] Y.C. Fung. *Bio-viscoelastic solids*. 1981.

[32] F. Fusco, M. Creta, C. De Nunzio, V. Iacovelli, F. Mangiapia, V.L. Marzi, and E.F. Agrò. Progressive bladder remodeling due to bladder outlet obstruction: a systematic

review of morphological and molecular evidences in humans. *BMC urology*, 18(1):1–11, 2018.

[33] T.W. Gilbert, S. Wognum, E.M. Joyce, D.O. Freytes, M.S. Sacks, and S.F. Badylak. Collagen fiber alignment and biaxial mechanical behavior of porcine urinary bladder derived extracellular matrix. *Biomaterials*, 29(36):4775–4782, 2008.

[34] C.J. Girman, S.J. Jacobsen, T. Tsukamoto, F. Richard, W.M. Garraway, P.P. Sagnier, H.A. Guess, T. Rhodes, P. Boyle, and M.M. Lieber. Health-related quality of life associated with lower urinary tract symptoms in four countries. *Urology*, 51:428–436, 1998.

[35] D.C. Gloeckner, M.S. Sacks, M.O. Fraser, G.T. Somogyi, W.C. de Groat, and M.B. Chancellor. Passive biaxial mechanical properties of the rat bladder wall after spinal cord injury. *The Journal of urology*, 167(5):2247–2252, 2002.

[36] J.A. Gosling. Modification of bladder structure in response to outflow obstruction and ageing. *Eur. Urol.*, 32 Suppl 1:9–14, 1997.

[37] S. Gravas, J.N. Cornu, M. M. Gacci, C. Gratzke, T.R.W. Herrmann, C. Mamoulakis, M.J. Rieken, M.and Speakman, and K.A.O. Tikkinen. Management of non-neurogenic male luts. 2022.

[38] D.J. Griffiths. The Mechanics of the Urethra and of Micturition. *British Journal of Urology*, 45:497–507, 1973.

[39] D.J. Griffiths and H.J. Rollema. Urine flow curves of healthy males: a mathematical model of bladder and urethal function during micturition. *Medical & Biological Engineering & Computing*, 17:291–300, 1979.

[40] A. Groutz, J.G. Blaivas, and D.C. Chaikin. Bladder outlet obstruction in women: definition and characteristics. *Neurourology and Urodynamics: Official Journal of the International Continence Society*, 19(3):213–220, 2000.

[41] A Grytsan, T. S. E. Eriksson, P. N. Watton, and T. C. Gasser. Growth description for vessel wall adaptation: A thick-walled mixture model of abdominal aortic aneurysm evolution. *Materials*, 10:994, 2017.

[42] T Hald and T Horn. The human urinary bladder in ageing. *Br. J. Urol.*, 82 Suppl 1(2):59–64, 1998.

[43] M. R. Hill, X. Duan, G. A. Gibson, S. Watkins, and Robertson A. M. A theoretical and non-destructive experimental approach for direct inclusion of measured collagen orientation and recruitment into mechanical models of the artery wall. *Journal of biomechanics*, 45:762–71, 2012.

[44] M.R. Hill. *A Novel Approach for Combining Biomechanical and Microstructural Analyses to Assess the Mechanical Damage Properties of the Artery Wall.* PhD thesis, University of Pittsburgh, 2011.

[45] J. Hornsby, D.M. Daly, D. Grundy, F. Cheng, A.M. Robertson, P.N. Watton, and M.S. Thompson. Quantitative multiphoton microscopy of murine urinary bladder morphology during in situ uniaxial loading. *Acta Biomaterialia*, 64:59–66, 2017.

[46] Jack Hornsby. *Bladder Microstructural and Biomechanical Modelling: in Vivo, in Vitro and in Silico (Ph.D. Thesis).* PhD thesis, University of Oxford, 2016.

[47] U Hübener and R Van Mastrigt. Computer simulation of micturition. *Urodinamica*, 4:81–90, 1994.

[48] A. Kaname, P.S. M, Robert J.B., and Subbarao V.Y. Urodynamic Characterization of Nonobstructive Voiding Dysfunction in Symptomatic Elderly Men. *J. Urol.*, 162:142–146, 1999.

[49] R.T. Kershen, K.M. Azadzoi, and M.B. Siroky. Blood Flow, Pressure and Compliance in the Male Human Bladder. *J. Urol.*, 168(1):121–125, 2002.

[50] J.C. Kim, J.Y. Yoon, S. Seo, T.K. Hwang, and Y.H. Park. Effects of partial bladder outlet obstruction and its relief on types I and III collagen and detrusor contractility in the rat. *Neurourology and Urodynamics*, 19:29–42, 2000.

[51] K M Kim, B A Kogan, C A Massad, and Y C Huang. Collagen and elastin in the obstructed fetal bladder. *J. Urol.*, 146(2 (Pt 2)):528–531, 1991.

[52] A.D. Kohan, M. Danziger, E.D. Vaughan Jr, and D Felsen. Effect of aging on bladder function and the response to outlet obstruction in female rats. *Urol. Res.*, pages 33–37, 2000.

[53] J Le Feber, E Van Asselt, and R Van Mastrigt. Neurophysiological modeling of voiding in rats: bladder pressure and postganglionic bladder nerve activity. *The American journal of physiology*, 272:R413–R421, 1997.

[54] R. Levin, P. Chichester, S. Levin, and R. Buttyan. Role of angiogenesis in bladder response to partial outlet obstruction. *Scandinavian Journal of Urology and Nephrology*, 38(215):37–47, 2004.

[55] E. Morales-Orcajo, T. Siebert, and M. Böl. Location-dependent correlation between tissue structure and the mechanical behaviour of the urinary bladder. *Acta biomaterialia*, 75:263–278, 2018.

[56] P.Y. Mure, M. Galdo, and N. Compagnone. Bladder function after incomplete spinal cord injury in mice: quantifiable outcomes associated with bladder function and efficiency of dehydroepiandrosterone as a therapeutic adjunct. *J Neurosurg*, 100(1 Suppl Spine):56–61, 2004.

[57] J. Nagatomi, D.C. Gloeckner, M.B. Chancellor, W.C. Degroat, and M.S. Sacks. Changes in the biaxial viscoelastic response of the urinary bladder following spinal cord injury. *Annals of biomedical engineering*, 32(10):1409–1419, 2004.

[58] J. Nagatomi, K.K. Toosi, J.S. Grashow, M.B. Chancellor, and M.S Sacks. Quantification of bladder smooth muscle orientation in normal and spinal cord injured rats. *Annals of biomedical engineering*, 33(8):1078–1089, 2005.

[59] A. N. Natali, A. L. Audenino, W. Artibani, C. G. Fontanella, E. L. Carniel, and E. M. Zanetti. Bladder tissue biomechanical behavior: Experimental tests and constitutive formulation. *Journal of Biomechanics*, 48:3088–3096, 2015.

[60] J. Nishiguchi, D.D. Kwon, Y. Kaiho, M.B. Chancellor, H. Kumon, P.B. Snyder, and N. Yoshimura. Suppression of detrusor overactivity in rats with bladder outlet obstruction by a type 4 phosphodiesterase inhibitor. *BJU international*, 99(3):680–686, 2007.

[61] V.W. Nitti. Pressure flow urodynamic studies: the gold standard for diagnosing bladder outlet obstruction. *Reviews in urology*, 7(Suppl 6):S14, 2005.

[62] V.W. Nitti, L.M. Tu, and J. Gitlin. Diagnosing bladder outlet obstruction in women. *The Journal of urology*, 161(5):1535–1540, 1999.

[63] A. Parekh, A.D. Cigan, S. Wognum, R.L. Heise, M.B. Chancellor, and M.S. Sacks. Ex vivo deformations of the urinary bladder wall during whole bladder filling: Contributions of extracellular matrix and smooth muscle. *J. Biomech.*, 43(9):1708–1716, 2010.

[64] N.D. Patel and J.K. Parsons. Age and bladder outlet obstruction are independently associated with detrusor overactivity in patients with benign prostatic hyperplasia. *European urology*, 54(2):419–426, 2008.

[65] N.D. Patel and J.K. Parsons. Epidemiology and etiology of benign prostatic hyperplasia and bladder outlet obstruction. *Indian journal of urology*, 30.2:170, 2014.

[66] A.S. Paya, D.R. Fernandez, D. Gil, J.M. Garcia Chamizo, and F.M. Perez. Mathematical modelling of the lower urinary tract. *Computer Methods and Programs in Biomedicine*, 109:323–338, 2013.

[67] A. Pigne, F.A. Valentini, and P.P. Nelson. Comparison at short follow-up of the changes in the voiding phase induced by sub-urethral tapes using a mathematical micturition model. *Current Urology*, 3(4):179–184, 2009.

[68] M. Pokrywczynska, I. Gubanska, G. Drewa, and T. Drewa. Application of bladder acellular matrix in urinary bladder regeneration: The state of the art and future directions. *Biomed Res. Int.*, 2015, 2015.

[69] S.V.K. Reddy and B.S. Ahammad. Non-invasive evaluation of bladder outlet obstruction in benign prostatic hyperplasia: a clinical correlation study. *Arab journal of urology*, 17(4):259–264, 2019.

[70] M.S. Sacks. Biaxial mechanical evaluation of planar biological materials. *J. Elast.*, 61:199–246, 2000.

[71] Masahiko Saito, Alan J. Wein, and Robert M. Levin. Effect of partial outlet obstruction on contractility: Comparison between severe and mild obstruction. *Neurourology and Urodynamics*, 12:573–583, 1993.

[72] R. Seydewitz, R. Menzel, T. Siebert, and M. Böl. Three-dimensional mechano-electrochemical model for smooth muscle contraction of the urinary bladde. *J Mech Behav Biomed Mater*, 75:128–14, 2017.

[73] N. Shinkai, K. Ichihara, K. Kobayashi, H. Tabata, K. Hashimoto, F. Fukuta, T. Tanaka, and N. Masumori. Long-term tadalafil administration can prevent functional and structural changes of the urinary bladder in male rats with partial bladder outlet obstruction. *Neurourol Urodyn*, 39:1330–1337, 2020.

[74] M.B. Siroky. The aging bladder. *Reviews in urology*, 6 Suppl 1:S3–S7, 2004.

[75] J. G. Susset and C. H. Regnier. Viscoelastic properties of bladder strips: standardization of a technique. *Investigative urology*, 18(8):445–450, 1981.

[76] E. Takaoka, M. Kurobe, H. Okada, S. Takai, T. Suzuki, N. Shimizu, J. Kwon, H. Nishiyama, N. Yoshimura, and C.J. Chermansky. Effect of trpv4 activation in a rat model of detrusor underactivity induced by bilateral pelvic nerve crush injury. *Neurourology and urodynamics*, 37(8):2527–2534, 2018.

[77] D.A Taub and J.T Wei. The economics of benign prostatic hyperplasia and lower urinary tract symptoms in the united states. *Current Prostate Reports*, 4(2):81–90, 2006.

[78] F.S. Teixeira, E. Neufeld, N. Kuster, and P.N. Watton. Modeling intracranial aneurysm stability and growth: an integrative mechanobiological framework for clinical cases. *Biomechanics and modeling in mechanobiology*, 19(6):2413–2431, 2020.

[79] K.K. Toosi, J. Nagatomi, M.B. Chancellor, and M.S. Sacks. The effects of long-term spinal cord injury on mechanical properties of the rat urinary bladder. *Annals of biomedical engineering*, 36(9):1470–1480, 2008.

[80] S. Tritschler, A. Roosen, C. Füllhase, C.G. Stief, and H. Rübben. Urethral stricture: etiology, investigation and treatments. *Deutsches Ärzteblatt International*, 110(13):220, 2013.

[81] R. Trostorf, E. Morales-Orcajo, T. Siebert, and M. Böl. Location-and layer-dependent biomechanical and microstructural characterisation of the porcine urinary bladder wall. *journal of the mechanical behavior of biomedical materials*, 115:104275, 2021.

[82] B. Uvelius. Length-tension relations of in vitro urinary bladder smooth muscle strips. *Journal of Pharmacological and Toxicological Methods*, 45:87–90, 2001.

[83] F. A Valentini, G.R. Besson, P.P. Nelson, and P.E. Zimmern. A mathematical micturition model to restore simple flow recordings in healthy and symptomatic individuals and enhance uroflow interpretation. *Neurourology and Urodynamics: Official Journal of the International Continence Society*, 19(2):153–176, 2000.

[84] F. van Duin, P.f.w.m. Rosier, N.j.m. Rijkhoff, P.e.v. van Kerrebroeck, F.m.j. Debruyne, and H. Wijkstra. A Computer model of the neural control of the lower urinary tract. *Neurourology and Urodynamics*, 17:175–196, 1998.

[85] I. Vlastelica, D. Veljković, V. Ranković, B. Stojanović, M. Rosić, and M. Kojić. Modeling of urinary bladder deformation within passive and active regimes. *Journal of Serbian Society for Computational Mechanics*, 1:129–134, 2007.

[86] C.C. Wang, J. Nagatomi, K.K. Toosi, N. Yoshimura, J.H. Hsieh, M.B. Chancellor, and M.S. Sacks. Diabetes-induced alternations in biomechanical properties of urinary bladder wall in rats. *Urology*, 73(4):911–915, 2009.

[87] P.N. Watton, N.A. Hill, and M. Heil. A mathematical model for the growth of the abdominal aortic aneurysm. *Biomechanics and modeling in mechanobiology*, 3(2):98–113, 2004.

[88] P.N. Watton, Y. Ventikos, and G.A. Holzapfel. Modelling the mechanical response of elastin for arterial tissue. *Journal of Biomechanics*, 42:1320–1325, 2009.

[89] S. Wognum. *A multi-phase structural consitituvie model for insights into soft tissue remodeling mechanisms*. PhD thesis, 2010.

[90] S. Wognum, D.E. Schmidt, and M.S. Sacks. On the mechanical role of de novo synthesized elastin in the urinary bladder wall. *Journal of biomechanical engineering*, 131:101018, 2009.

[91] M.L. Zeidel. Obstructive Uropathy. In L Goldman and A.I. Schafer, editors, *Goldman's Cecil Medicine*, page Chapt 123. Elsevier, 25th ed. edition, 2016.

[92] P. Zvara, J. Kliment Jr, A. L. DeRoss, B. H. Irwin, S. E. Malley, M. K. Plante, and M. A. Vizzard. Differential expression of bladder neurotrophic factor mrna in male and female rats after bladder outflow obstruction. *Journal of Urology*, 168:2682–8, 2002.